Alma Mater Studiorum · University of Bologna

School of Science
Department of Physics and Astronomy
Master Degree in Physics

Growth of structures in non-standard Dark Energy models

Supervisor:
Prof. Silvia Pascoli

Co-supervisors:
Prof. Olga Mena
Dr. Rasmi Hajjar

Submitted by:
Pietro Ghedini

Academic Year 2023/2024

Abstract

Despite the fact that the ΛCDM model has been highly successful over the last few decades in providing an accurate fit to a broad range of cosmological and astrophysical observations, different intriguing tensions and anomalies emerged at various statistical levels. Among these, the H_0 tension is now exceeding five standard deviations, pointing to new physics beyond the ΛCDM model. Alternative appealing models, still allowed by observations, include the interacting dark energy (IDE) scenario, where dark matter and dark energy interact non-gravitationally. It is well-known that within these interacting cosmologies the growth of structure is modified and departures from the standard cosmological model of structure formation are parameterised via the growth rate f.

This study explores the growth of structure in non-standard dark energy cosmologies, trying to extend the standard parametrisation for f to take into account the dependence on the coupling ξ between dark matter and dark energy. We aim as well to place constraints on the phenomenological parameters of these alternative models, by considering different datasets related to different cosmological measurements, to achieve a complementary analysis. We put emphasis, in particular, on redshift space distortion measurements (RSD), whose role has not been recently highlighted.

Sommario

Nonostante il modello cosmologico standard, noto come modello ΛCDM, abbia avuto molto successo negli ultimi decenni nel fornire un fit a molte osservazioni cosmologiche e astrofisiche, diverse tensioni e anomalie sono emerse a diversi livelli statistici. Tra queste, la tensione su H_0, ovvero il valore del parametro di Hubble oggi, supera ora le cinque deviazioni standard, suggerendo la necessità di nuova fisica che vada oltre il modello cosmologico standard ΛCDM. Tra i vari modelli alternativi, permessi dalle osservazioni, troviamo i modelli di energia oscura interagente (Interacting Dark Energy, IDE). In questi modelli, energia oscura e materia oscura interagiscono non gravitazionalmente. É noto che in questi modelli di cosmologie interagenti, la crescita delle strutture è modificata e deviazioni dal modello standard che descrive questo fenomeno sono parametrizzate tramite il rate di crescita f.

Questo studio esplora la crescita delle strutture in modelli cosmologici dove si considera una forma non standard di energia oscura, provando a estendere la nota parametrizzazione per f per includere la dipendenza sul parametro di accoppiamento ξ tra materia ed energia oscura. Ci poniamo inoltre l'obiettivo di fissare dei limiti sui possibili valori che i parametri cosmologici possono assumere in queste modelli cosmologici alternativi, considerando diversi set di dati derivanti da misurazioni differenti, per ottenre un'analisi complementare. Nel seguente lavoro, si è posta particolare enfasi sulle misure delle distorsioni nello spazio dei redshifts (Redshift Space Distortions, RSD), il cui ruolo non è stato evidenziato in lavori recenti.

Contents

Introduction

The standard cosmological model, known as ΛCDM, describes the Universe as isotropic and homogeneous on large scales. The majority of the matter in the model is made up of Cold Dark Matter (CDM), which is parameterised as a perfect fluid of collision-less particles that interact solely through gravity. The model also accounts for the existence of Dark Energy, represented by a cosmological constant Λ in the Einstein equations, responsible for the observed accelerated expansion of the Universe at later stages (see [1]). The ΛCDM model has been highly successful over the last few decades in providing an accurate fit to a broad range of cosmological and astrophysical observations. Nevertheless, as error-bars on cosmological parameters began to narrow, different intriguing tensions and anomalies emerged at various statistical levels. Currently, the most significant tension is between the Hubble constant (H_0) value, as measured by the SH0ES collaboration [2], that is using a distance ladder with Cepheids variables to calibrate Type Ia Supernovae ($H_0 = 73.04 \pm 1.04$ km/s/Mpc), and the value inferred by the Planck satellite [1] from Cosmic Microwave Background (CMB) observations ($H_0 = 67.36 \pm 0.54$ km/s/Mpc) assuming a ΛCDM model for the expansion history of the Universe. The so-called H_0 tension [3, 4] has recently overcome the threshold of five standard deviations [2, 5], essentially ruling out the possibility of a statistical fluke. Consequently, the H_0 tension suggests a discrepancy between our comprehension of the early (i.e. CMB measurements) and late (i.e. Cepheids measurements) Universe and may also point to new physics, because inferring H_0, i.e. the rate at which the Universe is expanding today, from observations of the Cosmic Microwave Background necessarily relies on the cosmological model and its underlying assumptions. In more complex cosmologies beyond ΛCDM, values of H_0 consistent with local distance ladder measurements can be obtained, and numerous potential solutions have been proposed in the literature, see, e.g., Refs. [6, 7] for some reviews.

Another important emerging tension of the ΛCDM model is the σ_8 tension, parameterised by $S_8 = \sigma_8(\Omega_\mathrm{m}/0.3)^{1/2}$ (from Planck CMB observations we obtain $S_8 = 0.825 \pm 0.011$ [1], while the weak lensing survey KiDS-1000 gives $S_8 = 0.766^{+0.020}_{-0.014}$ [8]).

One model that has gained popularity for potentially resolving the H_0 tension is the interacting dark energy (IDE) scenario, where a non-gravitational interaction between dark matter and dark energy is postulated [9, 10, 11, 12, 13, 14, 15, 16, 17, 18, 19, 20, 21, 22, 23, 24, 25, 26, 27, 28]. It is well-known that within this interacting cosmologies the growth of structure is modified, and therefore it is crucial to apply observational constraints on the former to set bounds on this putative cosmological scenario.

Departures from the standard cosmological model of structure formation are parameterised via the growth rate f [29, 30]. Within the canonical General Relativity scheme, and in a flat ΛCDM background, $f = [\Omega_{\mathrm{dm}}]^{\gamma}$ with $\gamma = 0.55$ [29] and Ω_{dm} is the relative energy density (i.e. we use Ω_{dm} but we refer to $\Omega_{\mathrm{dm}}/\Omega_{\mathrm{tot}}$). Consequently, a departure from this standard value would suggest an inconsistency between the concordance cosmological model and observations. Therefore, it is timely to explore what would be the deviations from the standard prediction for f within well-motivated, non standard models.

In this study, we aim to explore the growth of structure within non-standard dark energy cosmologies and set bounds on the phenomenological parameters describing the possible alternative models.

The structure of the thesis is as follows.

In Chapter 1, we will present the standard cosmological model, describing as well all the measurements that consolidate this model. In addition, we will present the framework of the standard cosmological perturbation theory.

In Chapter 2, we describe how to introduce a new non-gravitational interaction between dark matter and dark energy, leading to the interacting dark energy (IDE) models. We find a parametrisation for the growth function f and also for $\sigma_{8,0}$, namely the value of σ_8 today, for different values of the coupling. We also check the consistency of our parametrisation for f obtaining two different contour plots in the (Ω_{dm}, ξ) plane: the first one with data obtained from the public available codes `CLASS` [31, 32] and the other obtained considering our parametrisation for f.

In Chapter 3, we present the cosmological and astrophysical observations data-sets and likelihoods that will be used to constrain our model, showing the obtained results using `Cobaya` [33, 34].

Finally, in Chapter 4, we summarise and discuss the final results.

Chapter 1

Cosmology overview

1.1 The Standard Cosmological Model

The Standard Cosmological Model, also known as Hot Big Band Model, is the basis of the evolution theory of our Universe. It is based on the so called cosmological principle, stating that, on scales larger than 100 Mpc, the Universe is homogeneous and isotropic. The success of this cosmological model rests on three main observations: the expansion of the Universe, light element abundances (which are in agreement with Big Bang Nucleosynthesis predictions) and the Cosmic Microwave Background radiation (CMB) [35].

1.1.1 Hubble Law and Redshift

We have evidence that the Universe is expanding, as found by Hubble in 1929 [36]. He noticed that distant galaxies are receding from us and that the velocity increases with the distance. Then, in order to understand the history of the Universe, we need to study how the scale factor changes with time. To quantify the change in the scale factor it is useful to introduce a new parameter, called Hubble parameter $H(t)$, defined as

$$H(t) = \frac{1}{a}\frac{da}{dt} = \frac{\dot{a}}{a} \; , \tag{1.1}$$

where $a = a(t)$ is the scale factor and today $a(t_0) = 1$, meaning that at earlier times it was smaller. The value of this parameter today, $H(t_0) = H_0$ is a very important value in cosmology as, for example, it determines the age of the Universe today ($\sim H_0^{-1}$). Unfortunately, there are inconsistencies in the values obtained considering local (distance ladder with Cepheids variables to calibrate Type Ia Supernovae) measurements and early-Universe (CMB) measurements. This is known as H_0 tension [3]. From the Planck CMB measurements [1], we have $H_0 = (67.36 \pm 0.54)$ km/s/Mpc, while from the SH0ES collaboration [2] one finds $H_0 = (73.04 \pm 1.04)$ km/s/Mpc.

It is conventional to parameterise the Hubble parameter today, H_0, as $H_0 = 100h$

km/s/Mpc, where h is a dimensionless parameter whose value depends on the kind of measurement one is considering.

The expansion of the Universe changes also the light emitted by the sources in such a way that we measure an increased wavelength λ_o (measured at a time t_0, today) with respect to the emitted one λ_e (emitted at a time t_e). We introduce the parameter z, known as redshift, to measure this change in the wavelength, defined as

$$z = \frac{\lambda_o - \lambda_e}{\lambda_e} \; . \tag{1.2}$$

There exists a relation between the redshift and the scale factor, given by

$$1 + z = \frac{\lambda_o}{\lambda_e} = \frac{a(t_0)}{a(t_e)} = \frac{1}{a(t_e)} \; , \tag{1.3}$$

where we used the fact that today $a_0 = 1$.

If we consider two observers at rest in the comoving frame, they are moving away from each other with a velocity that depends on the evolution of the scale factor. At low redshift, so that $z \simeq v$ we find the Hubble law describing the expansion of the Universe

$$v = H_0 d \; , \tag{1.4}$$

so one expects that, at least at low redshift, the velocity of recession should increase linearly with the distance. Eq. (1.4) is only an approximation since, at larger redshifts, it only represents the first contribution: in order to get the correct relation, one must consider additional terms.

1.1.2 Friedmann-Lemaitre-Robertson-Walker metric

In order to study cosmology, we need to work with Einstein's theory of General Relativity. An important concept is the one of metric, which turns coordinate distances into physical distances, allowing us to make quantitative predictions in an expanding Universe. Moreover, the great advantage of the metric is that it incorporates gravity.

In four space-time dimensions, the interval between two points is defined, using Einstein summation rule[1], as

$$ds^2 = g_{\mu\nu} dx^\mu dx^\nu \; , \tag{1.5}$$

where the indices μ and ν run from 0 to 3 and the 0-th component refers to time.

The tensor $g_{\mu\nu}$, known as the metric tensor, is a symmetric tensor (so in principle has 10 non zero components) and it describes the space-time geometry.

In Special Relativity, the metric tensor is $\eta_{\mu\nu}$, which represents Minkowski space-time.

---

[1] Repeated indices are implicitly summed over.

Minkowski metric describes a static and flat Universe, therefore is not the proper metric to use in the case of a homogeneous and isotropic Universe which is expanding and in which matter and energy are present.
The form of the metric for our Universe can be partly fixed using the Cosmological Principle. In particular, homogeneity translates into invariance under translations ($g_{\mu\nu}$ must be independent of the spatial coordinates in cartesian coordinates), while isotropy means invariance under rotations (the off-diagonal elements must vanish). Then, what one finds is that the most general form of the metric is given by the Friedmann-Lemaître-Robertson-Walker (FLRW) metric [37]:

$$ds^2 = -dt^2 + a^2(t)\left[\frac{dr^2}{1-kr^2} + r^2(d\theta^2 + \sin^2(\theta)d\phi^2)\right] \,, \tag{1.6}$$

where r, θ and ϕ are the comoving coordinates and t is the proper time of an observer who sees the time expand uniformly around them.
The symmetries fix the metric up to arbitrary values for the scale factor $a(t)$, which describes the time evolution of the Universe, and for the curvature parameter k, which can assume three different values, corresponding to three different geometries:

- $k = -1$: in this case, we talk about an open Universe, where the $t =$ constant surface Σ_t is a 3D hyperboloid;
- $k = 0$: in this case, we recover flat space-time and Σ_t is flat;
- $k = +1$: in this case, we talk about a closed Universe and Σ_t is a 3D sphere.

Throughout this study we will always assume that we work in a flat Universe with $k = 0$.

1.1.3 Friedmann equations

The evolution of the Universe is described by the theory of General Relativity, i.e. by the Einstein equations, describing the evolution of physical systems under the action of gravity

$$G_{\mu\nu} = R_{\mu\nu} - \frac{1}{2}g_{\mu\nu}R = 8\pi G T_{\mu\nu} \,, \tag{1.7}$$

in which $G_{\mu\nu}$ is the Einstein tensor, G is the Newton constant, $T_{\mu\nu}$ is the stress-energy tensor, R is the Ricci scalar, $R = R_{\mu\nu}g^{\mu\nu}$, and $R_{\mu\nu}$ is the Ricci tensor, defined as

$$R_{\mu\nu} = \Gamma^\alpha_{\mu\nu,\alpha} - \Gamma^\alpha_{\mu\alpha,\nu} + \Gamma^\alpha_{\beta\alpha}\Gamma^\alpha_{\mu\nu} - \Gamma^\alpha_{\beta\nu}\Gamma^\beta_{\mu\alpha} \,, \tag{1.8}$$

where commas denote derivatives with respect to x and $\Gamma^\alpha_{\mu\nu}$ are the Christoffel symbols, defined as

$$\Gamma^{\alpha}_{\mu\nu} = \frac{1}{2} g^{\alpha\beta} (g_{\mu\beta,\nu} + g_{\nu\beta,\mu} - g_{\mu\nu,\beta}) \ . \tag{1.9}$$

Einstein later added a term to his equations as he believed that our Universe was a static one, but a static Universe containing only non relativistic matter would collapse:

$$R_{\mu\nu} - \frac{1}{2} g_{\mu\nu} R + g_{\mu\nu}\Lambda = 8\pi G_N T_{\mu\nu} \ . \tag{1.10}$$

Λ is the cosmological constant, which represents a vacuum energy and works as a repulsive force opposed to the collapse of the Universe. When Hubble discovered the expansion of the Universe in 1929, Einstein stated that the cosmological constant was the biggest mistake of his career. Today, Λ is needed in order to describe our Universe, in particular to explain the fact that our Universe is now in a phase of accelerated expansion.

In cosmology, one can assume the stress-energy momentum tensor $T_{\mu\nu}$ to be that of a perfect fluid, so

$$T_{\mu\nu} = (\rho + p) u_\mu u_\nu + p g_{\mu\nu} \ , \tag{1.11}$$

where ρ is the energy density (the sum of the energy densities of the single components), p is the (total) pressure and u_μ is the four velocity. In a homogeneous and isotropic Universe, $T_{\mu\nu}$ is diagonal, $T_{\mu\nu} = \mathrm{diag}(-\rho, p, p, p)$.

Considering Einstein equations (1.10), using the FLRW metric (1.6) and this particular form of the stress-energy tensor, we have that the 10 Einstein equations reduce to just 2 equations, known as Friedmann equations:

$$H^2 = \left(\frac{\dot{a}}{a}\right)^2 = \frac{8\pi G}{3}\rho - \frac{k}{a^2} \ ; \tag{1.12a}$$

$$\dot{H} + H^2 = \frac{\ddot{a}}{a} = -\frac{4\pi G}{3}(\rho + 3p) \ , \tag{1.12b}$$

where ρ and p are the total energy density and pressure of the Universe, including the cosmological constant contribution

$$\rho_\Lambda = -p_\Lambda = \frac{\Lambda}{8\pi G} \ . \tag{1.13}$$

The first Friedmann equation (1.12a) is usually rewritten in terms of the density parameter Ω as

$$1 - \Omega = -\frac{k}{a^2 H^2} \ , \tag{1.14}$$

where

$$\Omega = \frac{\rho}{\rho_{\mathrm{c}}} \tag{1.15}$$

and

$$\rho_{\mathrm{c}} = \frac{3H^2}{8\pi G} \ . \tag{1.16}$$

ρ_{c}, called critical density, represents the density we would have if we consider a flat Universe ($k = 0$). This means that the density parameter Ω is related to the geometry of the Universe. As a matter of fact:

- for an open Universe: $\Omega < 1 \leftrightarrow \rho < \rho_{\mathrm{c}} \leftrightarrow k = -1$;
- for a flat Universe: $\Omega = 1 \leftrightarrow \rho = \rho_{\mathrm{c}} \leftrightarrow k = 0$;
- for a closed Universe: $\Omega > 1 \leftrightarrow \rho > \rho_{\mathrm{c}} \leftrightarrow k = +1$.

The right hand side of Eq. (1.14) is known as the curvature parameter

$$\Omega_{\mathrm{k}} = -\frac{k}{a^2H^2} \tag{1.17}$$

and the energy density associated, also known as curvature density, is defined as

$$\rho_{\mathrm{k}} = -\frac{3k}{8\pi a^2 G} \ . \tag{1.18}$$

In order to fully be able to solve the Friedmann equations (1.12a) and (1.12b), we need a third equation. We use the equation of state for a perfect fluid, which relates its density and its pressure, $p = w\rho$, where w is a dimensionless parameter which takes a different value for each component of the Universe.

One can obtain a continuity equation for the density or via the conservation of the stress-energy momentum tensor, or combining the two Friedmann equations. The final result is that

$$\dot{\rho} = -3\frac{\dot{a}}{a}(\rho + p) = -3\frac{\dot{a}}{a}\rho(1 + w) \ , \tag{1.19}$$

whose general solution is given by

$$\rho \propto a^{-3(1+w)} \ . \tag{1.20}$$

Let us now study the general behaviour of the different components of the Universe, therefore, for different values of w:

- *Relativistic matter*: in this case, $w_{\mathrm{r}} = 1/3$ and this is generically referred to as radiation. The energy density evolves with the scale factor as $\rho_{\mathrm{r}} \propto a^{-4}$, with the scale factor evolving in time as $a(t) \propto t^{1/2}$ (for a spatially flat Universe $k = 0$, for which it is easy to solve the Friedmann equations). This tells us that the energy density of radiation decreases as the Universe expands.

- *Non-relativistic matter*: the fluid has zero pressure since $w_{\mathrm{m}} = 0$. This leads to $\rho_{\mathrm{m}} \propto a^{-3}$, with $a(t) \propto t^{2/3}$ (in the case of $k = 0$), which is what one would expect since the density goes like the inverse of the volume ($\sim a^3$). This means that it decreases less with the expansion of the Universe with respect to the radiation case: this is no surprise since the photons are redshifted as the Universe expands.

- *Vacuum energy*: for the case of a cosmological constant (or dark energy), $w_\Lambda = -1$, which means that $p_\Lambda = -\rho_\Lambda$, meaning that the density is a constant. In a spatially flat Universe, the scale factor exponentially grows as $a(t) \propto e^{H_\Lambda t}$.

- *Curvature*: if $k \neq 0$, we can treat the curvature component as an additional fluid with equation of state $w_{\mathrm{k}} = -1/3$. This leads to $\rho_{\mathrm{k}} \propto a^{-2}$ and $a(t) \propto t$.

As we see, the time dependence of the scale factor is determined by the energy density of the Universe.

Since our Universe is a mixture of different components, the fact that the energy densities evolve differently for each of them can lead to having different phases in the Universe history. The Big Bang Model predicts an initial phase of radiation domination, followed by a matter dominated epoch. Today, the Universe expansion is accelerated, which cannot be re-conducted to either components above, but we need something that behaves as a cosmological constant Λ (Dark Energy).

Using one of the Friedmann equations, i.e. (1.12a), we can derive the dependence of the Hubble parameter on the densities of the different components. This is given by

$$H^2 = H_0^2[\Omega_k^0 a^{-2} + \Omega_{\mathrm{m}}^0 a^{-3} + \Omega_{\mathrm{r}}^0 a^{-4} + \Omega_\Lambda^0] \ . \tag{1.21}$$

If we take $a = 1$, the densities satisfy the following relation

$$\Omega_{\mathrm{m}}^0 + \Omega_{\mathrm{r}}^0 + \Omega_\Lambda^0 + \Omega_k^0 = 1 \ . \tag{1.22}$$

1.1.4 Dark Matter and Dark Energy

When we use Ω_{m} we are actually referring at the contribution of two different components: baryonic matter, Ω_{b}, and dark matter (DM), Ω_{dm}. The most intriguing fact about this distinction is that we do not know the true nature of dark matter even though it constitutes the majority of the mass of the Universe. From [1], we know that ordinary matter makes up for the 5% of the Universe total energy, while dark matter represent the 26% of the total.

Dark matter has been introduced as a consequence of several evidences, as for example the necessity to have more matter in order to be able to explain the rotational velocities of spiral galaxies. In the 1970's, Vera Rubin found that the rotational velocity approaches an approximate constant value even outside of the range of luminous matter, while it was expected to decrease as $r^{-1/2}$, being r the distance from the galactic center [38]. A more recent evidence is the Bullet Cluster [39], which is a striking piece of evidence for non-collisional particle dark matter. When we talk about dark matter, we actually refer to cold dark matter (CDM). Therefore, in all the work, when we say dark matter (dm), we actually refer to cold dark matter (cdm).

The remaining part of the energy budget of the Universe, 69% [1], is represented by dark energy, whose nature is still a secret. It is a component with a strong negative pressure, dominating gravitational physics on large scales and is the responsible of the accelerating phase of expansion of our Universe right now.

In the standard cosmological model, dark energy is a cosmological constant component, characterised by an equation of state with $w_\Lambda = -1$.

The minimal scenario is the so called ΛCDM model, where we consider that the Universe is spatially flat ($\Omega_\mathrm{k} = 0.0007 \pm 0.0019$ [1]) and composed by baryonic matter ($\Omega_\mathrm{b} h^2 = 0.02242 \pm 0.00014$ [1]), cold dark matter ($\Omega_\mathrm{dm} = 0.11933 \pm 0.00091$ [1]) and dark energy ($\Omega_\Lambda = 0.6889 \pm 0.0056$ [1]).

From this, we see that Eq. (1.22) can be simply rewritten today, considering the main contributions, as

$$\Omega^0_\mathrm{dm} + \Omega^0_\Lambda = 1 \ . \tag{1.23}$$

1.1.5 Cosmological distances

Measuring distances in an expanding Universe is not an easy task. Moreover, one must discriminate between the comoving distance, which remains fixed as the Universe expands, and the physical distance, which instead grows as the Universe expands.

The total comoving distance, which is the distance that light can have traveled since $t = 0$, is given by

$$\eta = \int_0^t \frac{dt}{a(t)} \ , \tag{1.24}$$

and it is used to describe the distance between two points in the comoving frame, the reference frame where the coordinates of an observer at rest do not change during the evolution of the Universe. Regions separated by distances greater than η are not causally connected. The corresponding physical distance, that is the farthest distance we can observe today, is given by

$$d_H(t_0) = a(t_0)\eta \ , \tag{1.25}$$

which is also called horizon distance.
One can introduce the concept of proper distance d_P: this is the distance measured along a null geodesic. From the line element (1.6),

$$ds = \frac{a(t)dr}{\sqrt{1-kr^2}} \ . \tag{1.26}$$

Integrating this result, we obtain that the proper distance is

$$d_P(t) = a(t)f(r) \ , \tag{1.27}$$

where $f(r)$ is given by

$$f(r) = \begin{cases} \sin^{-1}(r) \ , & \text{if } k = 1 \ ; \\ r \ , & \text{if } k = 0 \ ; \\ \sinh^{-1}(r) \ , & \text{if } k = -1 \ . \end{cases} \tag{1.28}$$

There exists a relation between the proper distances at different times (for example today t_0 and a generic instant of time t), which is

$$d_P(t_0) = a_0 f(r) = \frac{a_0}{a(t)} d_P(t) \ . \tag{1.29}$$

In the case of a flat Universe ($k = 0$), and in absence of peculiar motion in the comoving frame ($\dot{r} = 0$), taking the derivative of Eq. (1.27) gives the Hubble law (1.4), if we evaluate it at $t = t_0$.
Another way to measure distances is by using the so-called distance-luminosity relation. If we denote with F the flux of energy measured by an observer at fixed distance from the source, the luminosity distance is defined such that

$$F = \frac{L}{A} = \frac{L}{4\pi d_L^2} \ . \tag{1.30}$$

In a flat FLRW space-time, since the photons get redshifted during the expansion and the luminosity depends on the redshift too, we find that the relation between the luminous and the physical distance is given by:

$$d_L = d_P(1+z) \ . \tag{1.31}$$

We can rewrite the luminosity distance in terms of the apparent and absolute magnitudes, respectively m and M. The first one is a measure of the flux of a source as seen by an observer on Earth, while the second is a measure of the flux emitted by the source. The difference of these two magnitudes, $m - M$, is called distance module.

$$d_L = 10^{(m-M-25)/5} \ . \tag{1.32}$$

In order to obtain this result, we must use astrophysical sources whose absolute magnitude is theoretically known. These objects are called standard candles and the most famous example is represented by the Cepheids variable stars. One could also use Supernovae, which are known as standardizable candles.

Another useful distance measurement is the angular diameter distance d_A.

Let us suppose that we know the proper length ℓ of an object, aligned perpendicular to our line of sight. Measuring the angular size of the object $\delta\theta$, it is possible to compute the angular distance from the relation

$$d_A = \frac{\ell}{\delta\theta} \ . \tag{1.33}$$

In the case of a static and Euclidean Universe, it coincides with the proper distance, $d_A = d_P$, while in a spatially flat Universe, the relation between the angular diameter distance and the luminosity distance is $d_L = (1+z)^2 d_A$.

1.1.6 Cosmological measurements

We review the observations that support the cosmological model described above. In particular, how the ΛCDM model parameters can be constrained by the measurements of Supernovae luminosity distances, Cosmic Microwave Background (CMB), Big Bang Nucleosynthesis (BBN), Baryon Acoustic Oscillations (BAO) and Large Scale Structure (LSS).

Supernovae

We have seen that the Hubble parameter measures the expansion rate of the Universe at a given time t. Since the Universe was thought to be decelerating in its expansion, the deceleration parameter was introduced and it is defined as

$$q = -\frac{\ddot{a}\, a}{\dot{a}^2} = \frac{\Omega_{\rm m}}{2} + \Omega_{\rm r} - \Omega_\Lambda \ , \tag{1.34}$$

where the second equality holds if the Universe only contains matter, radiation and a cosmological constant. To have an accelerated expansion for the Universe, we need $q_0 = q(t_0)$ to be negative, which cannot be explained by a cosmological model only containing matter and radiation.

We can write the luminosity distance for $z \ll 1$ Taylor expanding the scale factor around t_0, today:

$$d_L(z) \sim \frac{z}{H_0}\left[1 + \frac{1+q_0}{2} z\right] \ , \tag{1.35}$$

and we see that, at first order, we recover the Hubble law, but then we have deviations, related to the deceleration parameter. So both H_0 and q_0, related to the expansion of the Universe, can be obtained measuring the luminosity distance using standard candles.

In recent years, Supernovae are considered as standardizable candles because of the relation between their peak and light-curve width. They are divided into two classes, based on their spectra: Supernovae of type I (SNI) do not contain hydrogen absorption lines in their spectra and Supernovae of type II (SNII), that contain strong hydrogen absorption lines. SNI are divided themselves into three sub-classes: Ia, Ib and Ic. While Ib and Ic are similar to SNII, SNIa are completely different and can be used as standard candles due to their high luminosity. Moreover, we can expect the luminosity of these SNIa to be (roughly) always the same since they all explode starting from the same initial mass, known as Chandrasekhar limit ($M_C = 1.4 M_\odot$, with $M_\odot$ the mass of the Sun) [40]. From the light curve of a SN, we can obtain the two magnitudes, m and M, so we can obtain the luminosity distance d_L.

In addition, SNIa can constrain some of the cosmological parameters, like the density parameters Ω_i. As a matter of fact, we can rewrite the luminosity distance is terms of the densities of the different components present in our Universe as

$$d_L(a) = \frac{1+z}{H_0} \int_{1/(1+z)}^{1} \frac{da'}{a'^2 \sqrt{\Omega_\Lambda + \Omega_\mathrm{m} a'^{-3} + \Omega_\mathrm{r} a'^{-4}}} \,. \tag{1.36}$$

The search for SN in distant galaxies made by The Supernova Cosmology Project and the High-z Supernova Search Team, using light curves and redshifts of SNIa to measure cosmological parameters and the acceleration of the Universe, led to the discovery of cosmic acceleration.

Currently, the most recent results related to Supernovae are obtained thanks to the Dark Energy Survey (DES) [41] which aims as well to improve both the statistical precision of supernova cosmology and the control of systematic errors in using Supernovae to measure distances. DES is also designed to probe the origin of the accelerating Universe, helping to understand the nature of dark energy.

Out of this set of data, we can also set bounds on the density parameters, as can be seen in Fig. 1.2.

Another important data set is the Pantheon [44] one, composed by 1048 data points.

Cosmic Microwave Background

The Cosmic Microwave Background (CMB), discovered accidentally by Penzias and Wilson in 1965 [45], is a rich source of data for the Universe's cosmological parameters.

In the primordial Universe, photons and baryons were tightly coupled in the so-called photon-baryon fluid. At the epoch of recombination (T $\sim$ 3000K, $z_{dec} \sim 1090$), photons decoupled, free-streaming through the Universe. The epoch of last scattering, meaning the time at which a CMB photon underwent its last scattering from an electron, it is

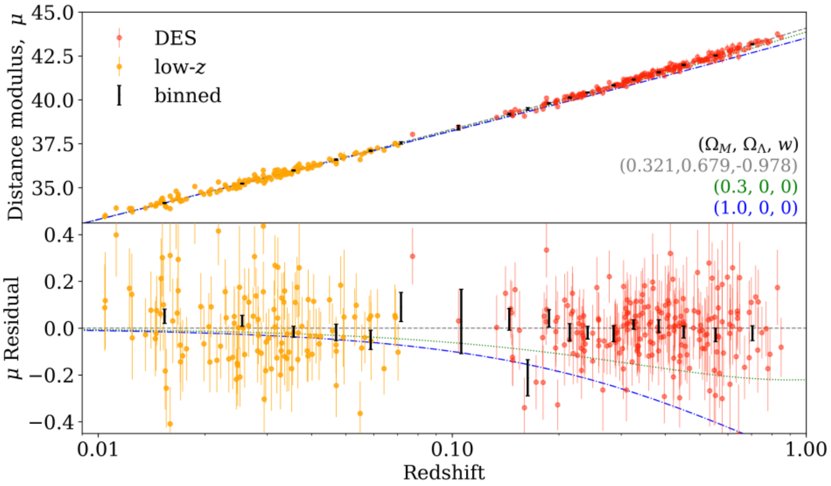

Figure 1.1: Hubble diagram for the DES-SN3YR sample. Top: distance modulus (μ) from BBC fit (black bars, which are used for cosmology fits) and for each SN (red, orange circles). The dashed gray line describe the best fit model, while the green and blue dotted lines show models with no dark energy and matter densities $\Omega_{\rm m} = 0.3$ and 1.0 respectively. Bottom: residuals to the best fit model; 1σ error bars show 68% confidence. Figure taken from [42].

the origin of the CMB. The Universe at this point was surprisingly isotropic, about 1 part in 10^5. The small anisotropies in temperature and polarization, that were present at the decoupling time, are essential to understand the physics at this redshift, but also to understand the early Universe (there could be processes leaving an imprint on the CMB photons, as for Baryon Acoustic Oscillations, BAO). Moreover, since the photons travelled to reach us, they also carry some (integrated) information about the post-decoupling Universe, since there could be processes affecting the photon's propagation.
The photons of the CMB present a black body spectrum since they were in thermal equilibrium with the electrons, with an average temperature of $T_{\rm CMB} = 2.725K$. This was first measured by the COsmic Background Explorer (COBE) satellite [46].
Let us consider the CMB temperature field as a function of the angle on the sky, $T(\hat{n})$, and let us denote the fractional difference (i.e. the dimensionless temperature fluctuation around the mean value) as

$$\Theta(\hat{n}) = \frac{T(\hat{n}) - T_{\rm CMB}}{T_{\rm CMB}} \ . \tag{1.37}$$

Since temperature fluctuations are defined on a spherical surface, we can expand this function in spherical harmonics as

$$\Theta(\hat{n}) = \sum_{\ell m} a_{\ell m} Y_{\ell m}(\hat{n}) \ . \tag{1.38}$$

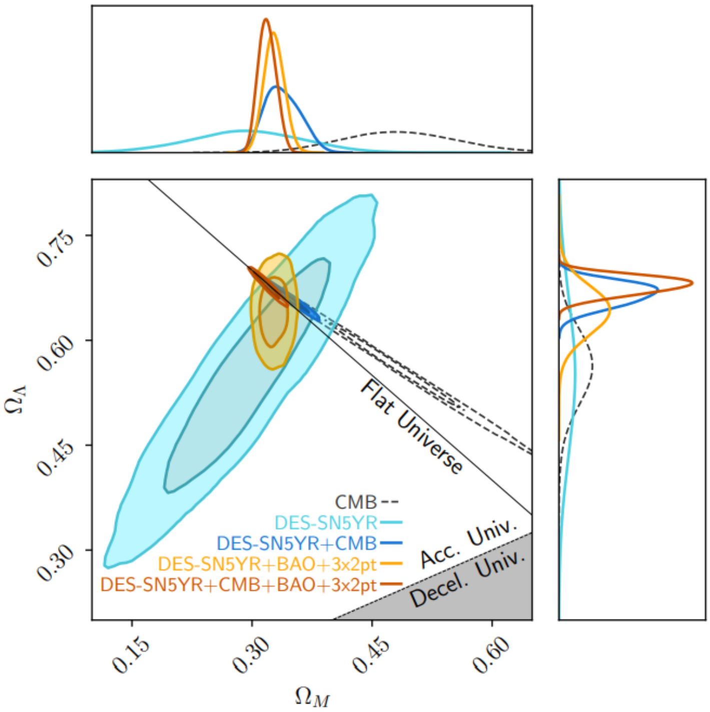

Figure 1.2: Constraints for the ΛCDM model (non-zero curvature allowed) from the DES-SN5YR dataset only (cyan), from DES-SN5YR combined with BAO and weak lensing measurements (orange), and from DES-SN5YR combined with CMB measurements (blue). For comparison, we also present cosmological constraints from Planck Collaboration (2020) only (black dashed). Figure taken from [43].

Assuming isotropy, we can define the power spectrum of the temperature anisotropies C_ℓ as an ensemble average of the expansion coefficients, which contain the information about the temperature perturbation,

$$C_\ell = \langle a_{\ell m} a^*_{\ell m} \rangle \ , \tag{1.39}$$

which does not depend on m due to isotropy. This is an important quantity since it can be predicted by cosmological models, meaning that a certain model can predict the statistic of the anisotropies. We cannot extract from observations the true power spectrum, but we can build an estimator,

$$\hat{C}_\ell = \frac{1}{2\ell + 1} \sum_{m=-\ell}^{\ell} a_{\ell m} a^*_{\ell m} \ . \tag{1.40}$$

This however is not a realistic way to calculate the spectrum, since the sky coverage is not complete and there are instrumental noises. This estimator is characterised by a

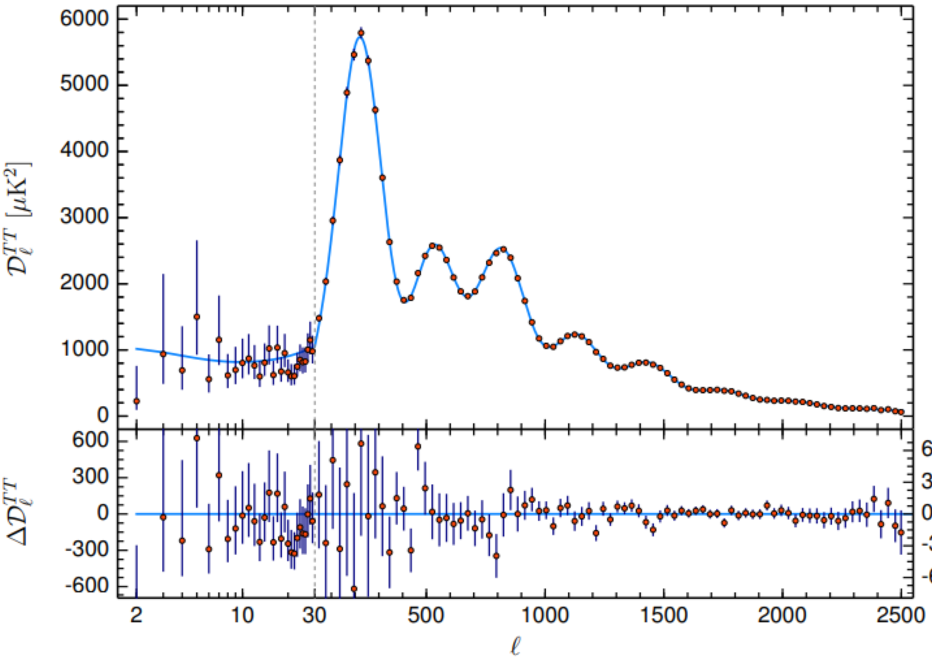

Figure 1.3: Planck 2018 temperature power spectrum. The base-ΛCDM theoretical spectrum best fit to the Planck TT,TE,EE+lowE+lensing likelihoods is plotted in light blue in the upper panel. Residuals with respect to this model are shown in the lower panel. Figure taken from [1].

variance, called cosmic variance,

$$\frac{\Delta C_\ell}{C_\ell} = \sqrt{\frac{2}{2\ell+1}}\,, \tag{1.41}$$

which decreases with increasing ℓ.

The relation between a certain multipole ℓ and the angular scale is such that $\theta\ell \sim \pi$, meaning that smaller (larger) multipoles correspond to large (small) angular scales.

From Fig. 1.3, we see that there are peaks in the power spectrum, a signal of correlations present between temperature anisotropies at different angular separations. These peaks are the acoustic waves generated in the early Universe from the primordial inhomogeneities in the distribution of dark matter.

The best data about the CMB are the one obtained by the Planck collaboration [1], the most recent release being the one in 2018. From these data, we can constraint the cosmological parameters: in particular, 6 parameters appear to be sufficient to describe the CMB spectra within the so-called concordance ΛCDM model (concordance because different observational probes of different nature all point to roughly the same values). These parameters are: the baryon density, $\omega_\mathrm{b} = \Omega_\mathrm{b}h^2$; the cold dark matter density, $\omega_\mathrm{dm} = \Omega_\mathrm{dm}h^2$; the optical depth τ; the characteristic angular size of the fluctuations in

the CMB (also called acoustic scale), $\theta_{\rm s}$; the scalar spectral index, $n_{\rm s}$; the amplitude of the primordial spectrum, $A_{\rm s}$. In [1], the values of these parameters, among the others, are given with 68% confidence regions.
Following [47], we can see how these parameters act on the CMB spectra, so how we can infer the constraints on them from the data:

- θ_s controls the peaks location. It is defined as the ratio between the sound horizon at decoupling, affected by changes in $\omega_{\rm b}$, and the angular diameter distance, which depends on the expansion history after decoupling and, for this reason, is controlled by Ω_Λ or h;
- the relative height between odd and even peaks depends on the ratio between $\Omega_{\rm b}$ and Ω_γ. Actually, we can say that Ω_γ is fixed since we know precisely T_{CMB};
- $\Omega_{\rm m}$ controls the amount of expansion between equality and decoupling, controlling the height of all peaks;
- the amplitude of the high-multipole is controlled by the expansion history before decoupling and so it depends on $\Omega_{\rm b}$ and $\Omega_{\rm m}$ $(= \Omega_{\rm b}+\Omega_{\rm dm})$;
- the overall amplitude of the power spectrum is controlled by $A_{\rm s}$;
- the overall tilt is controlled by $n_{\rm s}$;
- the slope at low multipoles is controlled by Ω_Λ and h;
- the amplitude at $\ell \gg 40$ versus at $\ell < 40$ is controlled by τ, that determines the suppression visible at high ℓ.

These are only the primary effects, those which held a higher effect, but there a number of other tiny dependencies that play a role, even if small: for example, from the first acoustic peak we can infer information about the geometry of the Universe. Moreover, CMB photons are polarized by the temperature quadrupole, sourced both by scalar perturbations and tensor perturbations (primordial gravitational waves), and they are affected by gravitational lensing.

Big Bang Nucleosynthesis

The primordial Universe is filled by a cosmic fluid consistent of relativistic particles in equilibrium and decoupled relativistic and non-relativistic particles. As the Universe cools down, at some point it will reach temperatures lower that the binding energy of light nuclei. This epoch of nuclear fusion is known as Big Bang Nucleosynthesis (BBN). In order to fully study this complex mechanism, one needs to consider the decoupling

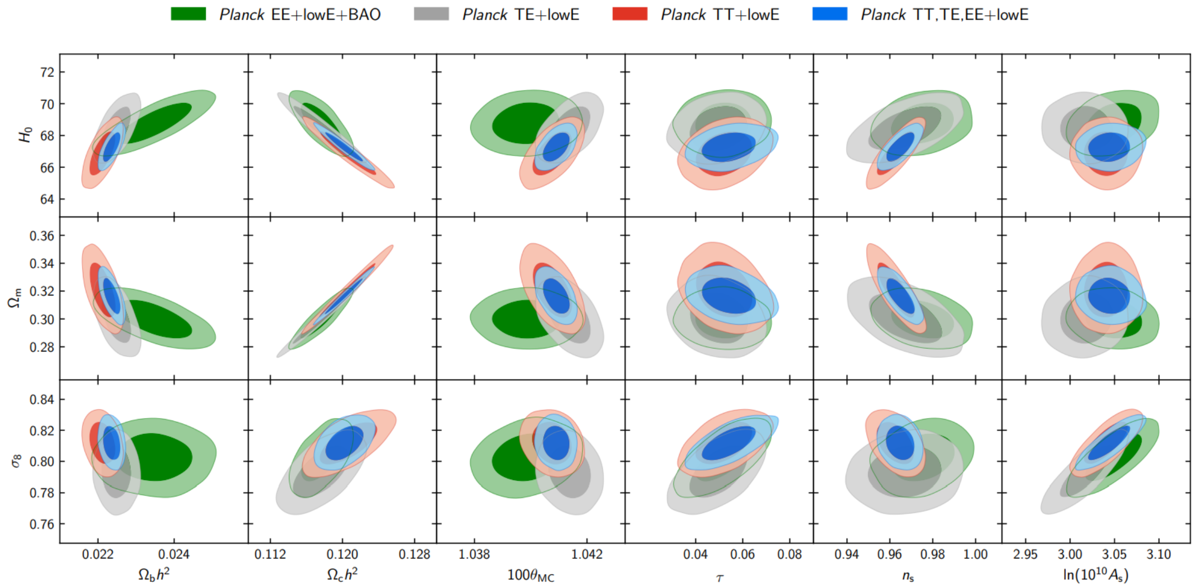

Figure 1.4: Constraints on parameters of the base-ΛCDM model from the separate Planck EE, TE, and TT high-ℓ spectra combined with low-ℓ polarization (lowE), and, in the case of EE also with BAO, compared to the joint result using Planck TT,TE,EE+lowE. Parameters on the bottom axis are our sampled MCMC parameters with flat priors, and parameters on the left axis are derived parameters (with H_0 in km s^{-1}Mpc^{-1}). Contours contain 68% and 95% of the probability. Figure taken from [1].

condition for each species present in the cosmic bath.
To describe BBN, we introduce the baryon-to-photon ratio η

$$\eta = \frac{n_{\mathrm{b}}}{n_\gamma} \ , \tag{1.42}$$

where

$$n_{\mathrm{b}} = \frac{n_{\mathrm{p}}}{X}, \text{ with } n_{\mathrm{p}} = g_{\mathrm{p}} \left(\frac{m_{\mathrm{p}} T}{2\pi}\right)^{3/2} e^{-\frac{m_{\mathrm{p}}}{T}} \tag{1.43}$$

is the number density of baryons (in terms of the ionisation fraction X) and

$$n_\gamma = \frac{2\zeta(3)}{\pi^2} T^3 \tag{1.44}$$

is the number density of photons.
Eq. (1.42) can be used to obtain the abundance of atomic nuclei, and the neutron-to-proton ratio

$$\frac{n_{\mathrm{n}}}{n_{\mathrm{b}}} = e^{-\frac{Q}{k_{\mathrm{b}} T}} \ , \tag{1.45}$$

where $Q = m_n - m_p$. If we assume that at a temperature of 0.1 MeV, the neutron-to-proton ratio has a value of 1/7, we find that the Helium abundance is $Y_{\rm He} \simeq 0.25$.
After BBN, only light nuclei are produced (Li^7 being the massive one) and their abundances can be used to constrain the cosmological parameters. In Fig. 1.5 we can see this, together with the Planck 2018 [1] results.

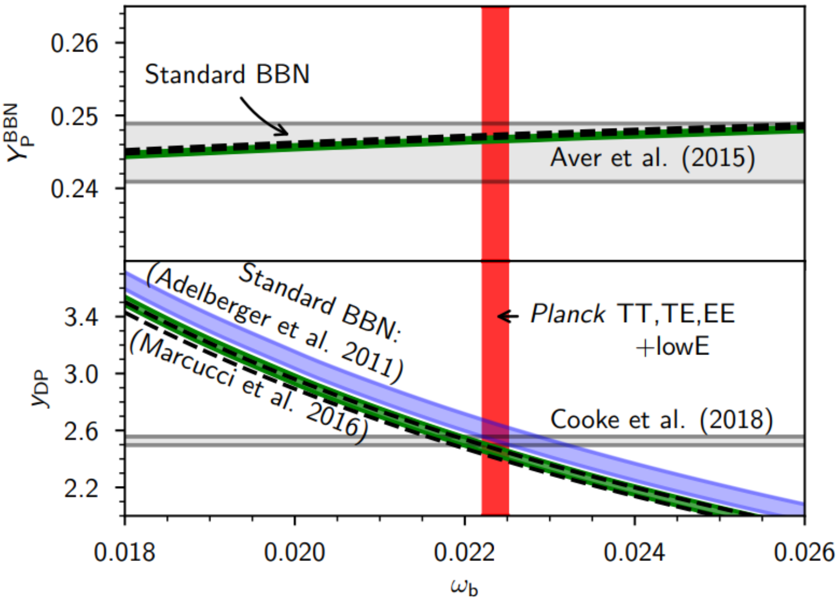

Figure 1.5: Summary of BBN results with $N_{\rm eff} = 3.046$, using Planck TT,TE,EE+lowE. All bands are 68% credible intervals. The standard BBN predictions computed with `PArthENoPE` are shown in green, while those from PRIMAT are in black dashed lines. The blue lines show the `PArthENoPE` results based on the experimental determination of nuclear rates by Adelberger et al. (2011), instead of the theoretical rate of Marcucci et al. (2016). Figure taken from [1].

Baryon Acoustic Oscillations

Before recombination, for $z > 1100$, the competition between gravity and radiation pressure brings to oscillations in the plasma that propagates as acoustic waves, known as Baryon Acoustic Oscillations (BAO). They were detected for the first time in 2005 by the Sloan Digital Sky Survey (SDSS) [48], but now there are several independent galaxy surveys that have detected them, spanning a range of redshifts.
At recombination, pressure waves get frozen and baryons accumulate at a fixed distance from the original overdensity. So acoustic oscillations imprint a characteristic scale in the clustering of matter, which can be seen at late times in the matter power spectrum as a sequence of peaks and troughs, corresponding to an oscillating mode caught at an extrema (peaks) or in phase with the background (troughs). BAO then provides a standard ruler to measure the distance to various redshifts using the clustering distribution of

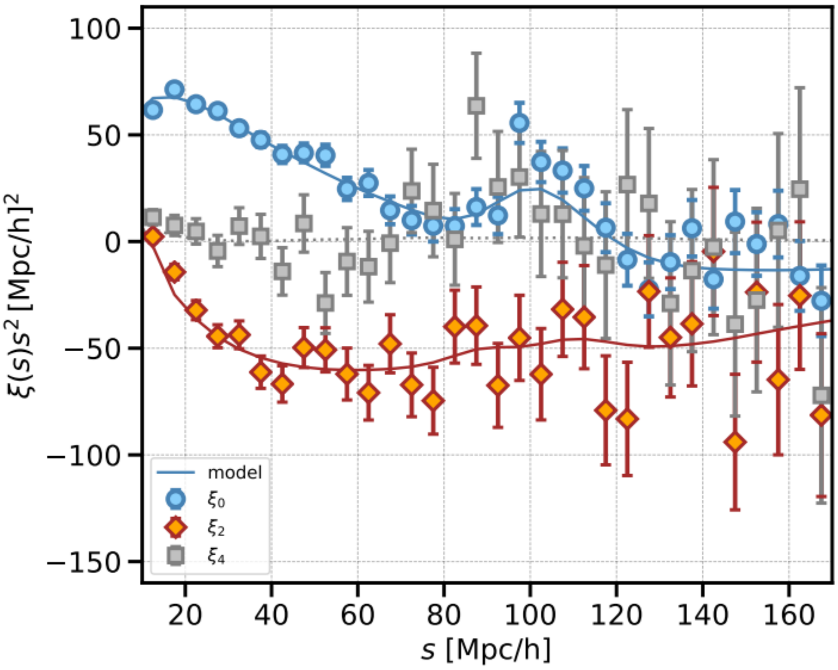

Figure 1.6: The measured correlation function for monopole ($\ell = 0$, blue), quadrupole ($\ell = 2$, red) and hexadecapole ($\ell = 4$, gray), with the best fitting full-shape model shown by the solid line. Figure taken from [49].

galaxies measured from large galaxy surveys. This relation depends on the cosmological parameters.

The BAO scale is set by the radius of the sound horizon at the time of photon decoupling, the end of baryon drag.

Moreover, the BAO and SNIa methods to estimate distances are completely complementary, since they are based on different principles.

The most precise BAO measurements today come from the extended Baryon Oscillation Spectroscopy Survey (eBOSS) DR16 galaxy sample [50, 51] and they allow to constrain the cosmological parameters through their impact on the sound horizon radius and on the distances $D_H = 1/H(z)$ and D_M, the comoving angular diameter distance. In particular, the most constrained parameters by BAO distance measurements are H_0 and $\Omega_{\rm m}$, making these measurements complementary to the CMB one and actually, the BAO measurements serve as a probe to break CMB's degeneracies.

Large Scale Structure

Under the effect of gravity, the tiny inhomogeneities at decoupling, that transforms in the anisotropies of the CMB, collapse to form the structures we see today in the Universe under the action of gravity. One of the main differences with the CMB is the fact that

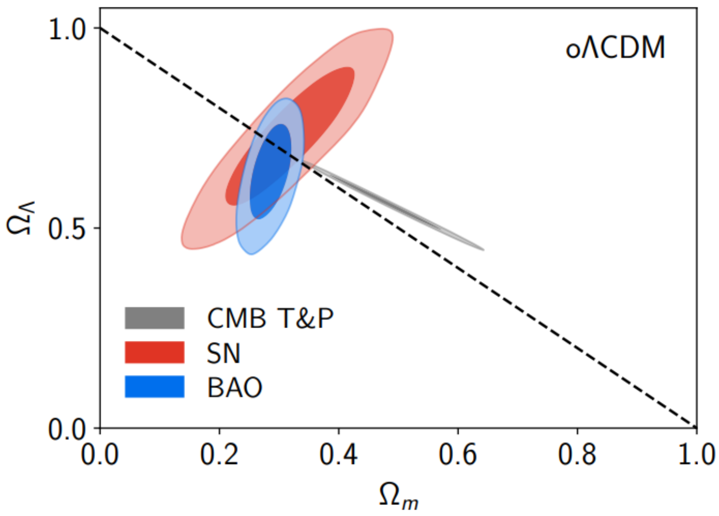

Figure 1.7: Cosmological constraints under the assumption of a model with a $w = -1$ cosmological constant with free curvature (oΛCDM). 68% and 95% constraints on $\Omega_\mathrm{m} - \Omega_\Lambda$ from the Planck CMB temperature and polarization data (gray), Pantheon SNe Ia sample (red), and SDSS BAO-only measurements (blue). The dashed line represents a model with zero curvature. Figure taken from [50].

we can observe the Large Scale Structure (LSS) at various redshifts.
We can define the power spectrum of matter density fluctuations P_m, which basically is the counterpart to the power spectrum C_ℓ of the CMB, as

$$P_\mathrm{m}(k,z)\delta(\mathbf{k}-\mathbf{k}') = \langle \delta_\mathrm{m}(\mathbf{k},z)\delta_\mathrm{m}(\mathbf{k}',z)\rangle \ , \tag{1.46}$$

where $\delta_\mathrm{m}(\mathbf{k},z)$ is the matter overdensity field. This result is obtained in Fourier space: working in real space, we have $\xi(r)$, which is known as the correlation function. Even if they represent the same quantity, $P_\mathrm{m}(k,z)$ is used to measure the galaxy power spectrum, depending both on background and perturbation evolution, while $\xi(r)$ is used to provide a BAO distance measurement, essentially a background probe. In both cases, the spectrum depends on the cosmological parameters.
Among all the galaxy surveys aimed at measuring the LSS of our Universe, we name the SDSS and the BOSS ones, which uses BAO, together with the most recent DESI.
One can also consider the so called Redshift Space Distortions (RSD) [52] to study the LSS, serving as a probe for linear growth of structures. In particular, RSD's serve as a probe for the combined quantity $f\sigma_8$, which is the product between the linear growth rate (which we will discuss more in detail in the next section) and the root mean square mass fluctuation amplitude for spheres of size $8h^{-1}$ Mpc.
The mass variance of the matter clustering, for a generic physical scale R, is given by [53]

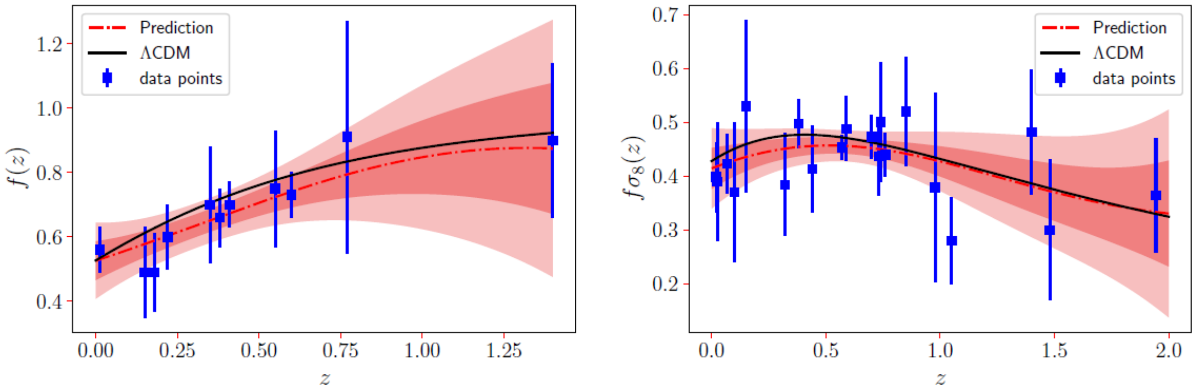

Figure 1.8: Left panel: Growth rate reconstruction $f^{GP}(z)$ from Tab. 1.1. Right panel: The reconstruction of $[f^{GP}\sigma_8](z)$ function using the sample in Tab. 1.2. In both plots the shaded areas represent the 1σ and 2σ CL regions. Figure taken from [53].

$$\sigma_R^2 = \frac{1}{2\pi^2}\int_0^\infty P(k,z)W_R^2(k)dk \ , \tag{1.47}$$

where $P(k,z)$ is the matter power spectrum and $W_R(k)$ is the window function.
The matter power spectrum can be written, introducing the transfer function $T^2(k)$ and the linear growth function $D(z)$, as

$$P(k,z) = \left[\frac{D(z)}{D(z=0)}\right]^2 T^2(k)P(k,z=0) \ . \tag{1.48}$$

If we fix $R = 8$ Mpc$/h$, combining Eqs. (1.47) and (1.48) we obtain that $\sigma_8(z) = D(z)\sigma_8(z=0)$.
The $f(z)$ data are shown in Tab. 1.1, while the $[f\sigma_8](z)$ data are shown in Tab. 1.2. [53]

Survey	z	f	Reference	Cosmological tracer
ALFALFA	0.013	0.56 ± 0.07	[54]	HI extragalactic sources
2dFGRS	0.15	0.49 ± 0.14	[55, 56]	galaxies
GAMA	0.18	0.49 ± 0.12	[57]	multiple-tracer: blue and red gals.
WiggleZ	0.22	0.60 ± 0.10	[58]	galaxies
SDSS	0.35	0.70 ± 0.18	[59]	luminous red galaxies (LRG)
GAMA	0.38	0.66 ± 0.09	[57]	multiple-tracer: blue and red gals.
WiggleZ	0.41	0.70 ± 0.07	[58]	galaxies
2SLAQ	0.55	0.75 ± 0.18	[60]	LRG & quasars
WiggleZ	0.60	0.73 ± 0.07	[58]	galaxies
VIMOS-VLT Deep Survey	0.77	0.91 ± 0.36	[56]	faint galaxies
2QZ & 2SLAQ	1.40	0.90 ± 0.24	[61]	quasars

Table 1.1: Data compilation of 11 $f(z)$ measurements. [53]

Survey	z	$f\sigma_8$	Reference	Cosmological tracer
SnIa + IRAS	0.02	0.398 ± 0.065	[62]	SNIa + galaxies
6dFGS	0.025	0.39 ± 0.11	[63]	void
6dFGS	0.067	0.423 ± 0.055	[64]	galaxies
SDSS-veloc	0.10	0.37 ± 0.13	[65]	DR7 galaxies
SDSS-IV	0.15	0.53 ± 0.16	[66]	eBOSS DR16 MGS
BOSS-LOWZ	0.32	0.384 ± 0.095	[67]	DR10, DR11
SDSS-IV	0.38	0.497 ± 0.045	[66]	eBOSS DR16 galaxies
WiggleZ	0.44	0.413 ± 0.080	[68]	LRG & bright emission-line galaxies
CMASS-BOSS	0.57	0.453 ± 0.022	[69]	DR12 voids + galaxies
SDSS-CMASS	0.59	0.488 ± 0.060	[70]	DR12
SDSS-IV	0.70	0.473 ± 0.041	[66]	eBOSS DR16 LRG
WiggleZ	0.73	0.437 ± 0.072	[68]	bright emission-line galaxies
SDSS-IV	0.74	0.50 ± 0.11	[71]	eBOSS DR16 voids
VIPERS v7	0.76	0.440 ± 0.040	[72]	galaxies
SDSS-IV	0.85	0.52 ± 0.10	[71]	eBOSS DR16 voids
SDSS-IV	0.978	0.379 ± 0.176	[73]	eBOSS DR14 quasars
VIPERS v7	1.05	0.280 ± 0.080	[72]	galaxies
FastSound	1.40	0.482 ± 0.116	[74]	ELG
SDSS-IV	1.48	0.30 ± 0.13	[71]	eBOSS DR16 voids
SDSS-IV	1.944	0.364 ± 0.106	[73]	eBOSS DR14 quasars

Table 1.2: Data compilation of 20 $[f\sigma_8](z)$ measurements. [53]

1.2 Cosmological perturbation theory

The nonlinear structures that we see today in our Universe, as galaxies or clusters, were generated by small initial perturbations due to gravitational instabilities that evolved after the CMB decoupling. The non linearity of these structures is the reason why the cosmological principle is true only on large scales.

If we consider a non relativistic fluid, perturbation theory can be simply described by the Newtonian theory of gravity, but for what is of interest to us later, we will consider a relativistic fluid and therefore we need to use the theory of General Relativity, even though this brings in the issue of gauge freedom.

When studying perturbation theory, one needs to distinguish two possibilities: introducing the scale that governs the growth of perturbations $R_H = H^{-1}$, a perturbation with wavelength λ, at a certain time t, is inside the horizon if $a\lambda < H^{-1}$, while is outside the horizon if $a\lambda > H^{-1}$. The horizon crossing of a perturbation corresponds to $a\lambda = H^{-1}$.

We start the study of cosmological perturbations by perturbing the metric, namely

$$g_{\mu\nu} = g^{(0)}_{\mu\nu} + g^{(1)}_{\mu\nu} \ , \tag{1.49}$$

where $g^{(0)}_{\mu\nu}$ represent the homogeneous background and is only (cosmic) time dependent, while $g^{(1)}_{\mu\nu}$ represents the small (with respect to the background) spatially dependent perturbation.

The equations of General Relativity are invariant under a general change of coordinates, meaning that ds^2 must remain constant. What we want to do here is a gauge transformation: we select a class of transformations that leave $g^{(0)}_{\mu\nu}$ invariant and only change the $g^{(1)}_{\mu\nu}$ part of the metric.

In the literature, the most common gauge choices are represented by the synchronous gauge and the conformal Newtonian (or longitudinal) gauge [75]. In the following we will only consider the Newtonian gauge as it is particularly convenient to study scalar perturbations (we neglect the study of vector and tensor perturbations).

With this gauge choice and introducing the conformal time τ defined as $d\tau = dt/a(t)$, the perturbed line element is obtained adding two additional functions that depend both on space and time, taking into account the fact that at small scales the Universe is not homogeneous and isotropic

$$ds^2 = a^2(\tau)\{-(1+2\psi)d\tau^2 + (1-2\phi)dx^i dx_i\} \ , \tag{1.50}$$

where $\psi{=}\psi(\tau,\vec{x})$ and $\phi{=}\phi(\tau,\vec{x})$ are two scalars potentials characterizing the perturbations. An advantage of using this gauge is that, in the Newtonian limit, ψ reduces to the gravitational potential. ϕ, instead, is the spatial curvature perturbation.

The metric $\mathrm{g}_{\mu\nu}$ is given by:

$$g_{\mu\nu} = a^2(\tau)\begin{pmatrix} -1-2\psi & 0 & 0 & 0 \\ 0 & 1-2\phi & 0 & 0 \\ 0 & 0 & 1-2\phi & 0 \\ 0 & 0 & 0 & 1-2\phi \end{pmatrix} , \tag{1.51}$$

and the inverse can be easily obtained by simply inverting the diagonal element and Taylor expanding as we consider small perturbations

$$g^{\mu\nu} = a^{-2}(\tau)\begin{pmatrix} -1+2\psi & 0 & 0 & 0 \\ 0 & 1+2\phi & 0 & 0 \\ 0 & 0 & 1+2\phi & 0 \\ 0 & 0 & 0 & 1+2\phi \end{pmatrix} . \tag{1.52}$$

With this new metric, we want now to write the Einstein equations (1.7) at linear order in perturbation theory.

Computing all the necessary ingredients and moving to Fourier space, what we obtain is [75]:

$$k^2\phi + 3\frac{\dot{a}}{a}\left(\dot{\phi} + \frac{\dot{a}}{a}\psi\right) = 4\pi G a^2 \delta T^0_0 \ ; \tag{1.53a}$$

$$k^2\left(\dot{\phi} + \frac{\dot{a}}{a}\psi\right) = 4\pi G a^2 (\rho + p)\theta \ ; \tag{1.53b}$$

$$\ddot{\phi} + \frac{\dot{a}}{a}\left(2\dot{\phi} + \dot{\psi}\right) + \left(2\frac{\ddot{a}}{a} - \frac{\dot{a}^2}{a^2}\right)\psi + \frac{k^2}{3}(\phi - \psi) = \frac{4\pi G a^2}{3}\delta T^i_i \ ; \tag{1.53c}$$

$$k^2(\phi - \psi) = 12\pi G a^2(\rho + p)\sigma \ , \tag{1.53d}$$

where θ is defined such that $(\rho + p)\theta = ik^j \delta T^0_j$ and σ is defined such that $(\rho + p)\sigma = -(\hat{k}_i \hat{k}_j - 1/3\delta_{\mathrm{ij}})\Sigma^i_j$. $\Sigma^i_j = T^i_j - \delta^i_j T^k_k/3$ represents the traceless component of T^i_j and σ is related to the anisotropic stress perturbation Π by $3\sigma(\rho + p) = 2\Pi p$.
To linear order in the perturbations, the components of the stress-energy tensor are:

$$T^0_0 = -(\rho + \delta\rho) \ ; \tag{1.54a}$$
$$T^0_i = -T^i_0 = (\rho + p)v_i \ ; \tag{1.54b}$$
$$T^i_j = (p + \delta p)\delta^i_j + \Sigma^i_j \ , \tag{1.54c}$$

where we allowed an anisotropic shear perturbation in T^i_j $(\Sigma^i_i = 0)$ and $v^i = dx^i/dt$ is a small coordinate velocity.
The conservation of the energy-momentum tensor is a consequence of the Einstein equations

$$T^{\mu\nu}_{;\mu} = \partial_\mu T^{\mu\nu} + \Gamma^\nu_{\alpha\beta}T^{\alpha\beta} + \Gamma^\alpha_{\alpha\beta}T^{\nu\beta} = 0 \ . \tag{1.55}$$

Using this result, we obtain:

$$\dot{\delta} = -(1 + w)(\theta - 3\dot{\phi}) - 3\frac{\dot{a}}{a}\left(\frac{\delta p}{\delta\rho} - w\right)\delta \ ; \tag{1.56a}$$
$$\dot{\theta} = -\frac{\dot{a}}{a}(1 - 3w)\theta - \frac{\dot{w}}{w + 1}\theta + \frac{\delta p}{\delta\rho}\frac{k^2\delta}{1 + w} - k^2(\sigma - \psi) \ , \tag{1.56b}$$

where $\delta = \delta\rho/\rho$ and θ is the divergence of the fluid velocity, $\theta = \partial_i v^i$. These equations are valid for a single uncoupled fluid or for the net (mass-averaged) δ and σ for all fluids. If there is a coupling among different components, we need to modify these results for the involved components.
Considering Cold Dark Matter (CDM), we can set $\theta = \sigma = w = \dot{w} = 0$, and neglecting the $\dot{\phi}$ term since it gives a smaller contribution than the others (we are considering the Newtonian limit, i.e. i.e. $k \gg \mathcal{H}$), the above equations reduce to

$$\dot{\delta}_{\mathrm{dm}} = -\theta_{\mathrm{dm}} \ ; \tag{1.57a}$$
$$\dot{\theta}_{\mathrm{dm}} = -\frac{\dot{a}}{a}\theta_{\mathrm{dm}} + k^2\psi \ . \tag{1.57b}$$

We want to obtain an equation for δ_{dm}, so we take the time derivative of Eq. (1.57a) and we substitute Eq. (1.57b)

$$\ddot{\delta}_{\rm dm} = -\dot{\theta}_{\rm dm} = \mathcal{H}\theta_{\rm dm} - k^2\psi \ , \tag{1.58}$$

where $\mathcal{H} = \dot{a}/a$. From Eq. (1.53d) we see that $\phi = \psi$ and using Eq. (1.53a), we can substitute

$$k^2\psi = -4\pi G a^2 \rho\delta_{\rm dm} \tag{1.59}$$

inside Eq. (1.58) and, using Eq. (1.57a), the result we obtain is

$$\ddot{\delta}_{\rm dm} + \mathcal{H}\dot{\delta}_{\rm dm} - 4\pi G a^2 \rho_{\rm dm}\delta_{\rm dm} = 0 \ . \tag{1.60}$$

Now, we want to go from having derivatives with respect to conformal time τ to have derivatives with respect to the scale factor a. This means that

$$\dot{\delta}_{\rm dm} = \frac{d\delta_{\rm dm}}{d\tau} = \frac{d\delta_{\rm dm}}{da}\frac{da}{d\tau} = \delta'_{\rm dm}\dot{a} = \delta'_{\rm dm}a\mathcal{H} \ . \tag{1.61}$$

Inserting this in Eq. (1.60) and dividing by $a^2\mathcal{H}^2$, we obtain

$$\delta''_{\rm dm} + \left(\frac{2}{a} + \frac{\mathcal{H}'}{\mathcal{H}}\right)\delta'_{\rm dm} - \frac{4\pi G}{\mathcal{H}^2}\rho_{\rm dm}\delta_{\rm dm} = 0 \ . \tag{1.62}$$

We can now manipulate some of the terms appearing in this equation.
Let us firstly consider $\mathcal{H}'$: we rewrite it back in terms of derivative with respect to τ

$$\mathcal{H}' = \frac{d\mathcal{H}}{da} = \frac{d\mathcal{H}}{d\tau}\frac{d\tau}{da} = \dot{H}\dot{a}^{-1} \ . \tag{1.63}$$

in such a way that we can introduce the deceleration parameter q, defined as

$$q = -\frac{\dot{\mathcal{H}}}{\mathcal{H}^2} = \frac{1}{2}(1 + 3w\Omega_{\rm de}) \ . \tag{1.64}$$

Let us now work on the last term in Eq. (1.62): we see that we can introduce the critical density ρ_{cr} as long as we substitute the Hubble parameter in proper time τ, $\mathcal{H}(\tau)$, with the one in cosmological time t, $H(t)$, using the following relation $\mathcal{H}(\tau) = aH(t)$.
Then,

$$\frac{4\pi G}{\mathcal{H}^2}\rho_{\rm dm} = \frac{4\pi G}{a^2H^2}\rho_{\rm dm} = \frac{3}{2a^2}\frac{\rho_{\rm dm}}{\rho_{cr}} = \frac{3}{2a^2}\Omega_{\rm dm} \tag{1.65}$$

and, putting everything inside Eq. (1.62), we obtain the result we were looking for:

$$\delta''_{\rm dm} = -(2-q)\frac{\delta'_{\rm dm}}{a} + \frac{3\Omega_{\rm dm}}{2}\frac{\delta_{\rm dm}}{a^2} \ . \tag{1.66}$$

One could try to solve now this equation numerically, considering the simple case of $w = -1$, corresponding to having the dark energy described by a cosmological constant.

In Fig. 1.10, we can see the behaviour of $\delta_{\rm dm}/a$ as a function of a, obtained solving numerically Eq. (1.66) (to solve it we used a Python code).
In order to do this, we use the expression of the deceleration parameter q in terms of $\Omega_{\rm de}$, as written in Eq. (1.64). We must keep in mind that the density parameters appearing in the equations are the time dependent relative ones, meaning that we must substitute $\Omega_{\rm i}$ with $\Omega_{\rm i}/\Omega_{\rm tot}$ in the equations. Assuming $\Omega_{\rm tot}$ is simply given by the dark energy and the dark matter contribution, we have

$$\Omega_{\rm de} \rightarrow \frac{\Omega_{\rm de}}{\Omega_{\rm de} + \Omega_{\rm dm} a^{-3}} \text{ and } \Omega_{\rm dm} \rightarrow \frac{\Omega_{\rm dm} a^{-3}}{\Omega_{\rm de} + \Omega_{\rm dm} a^{-3}} \ . \tag{1.67}$$

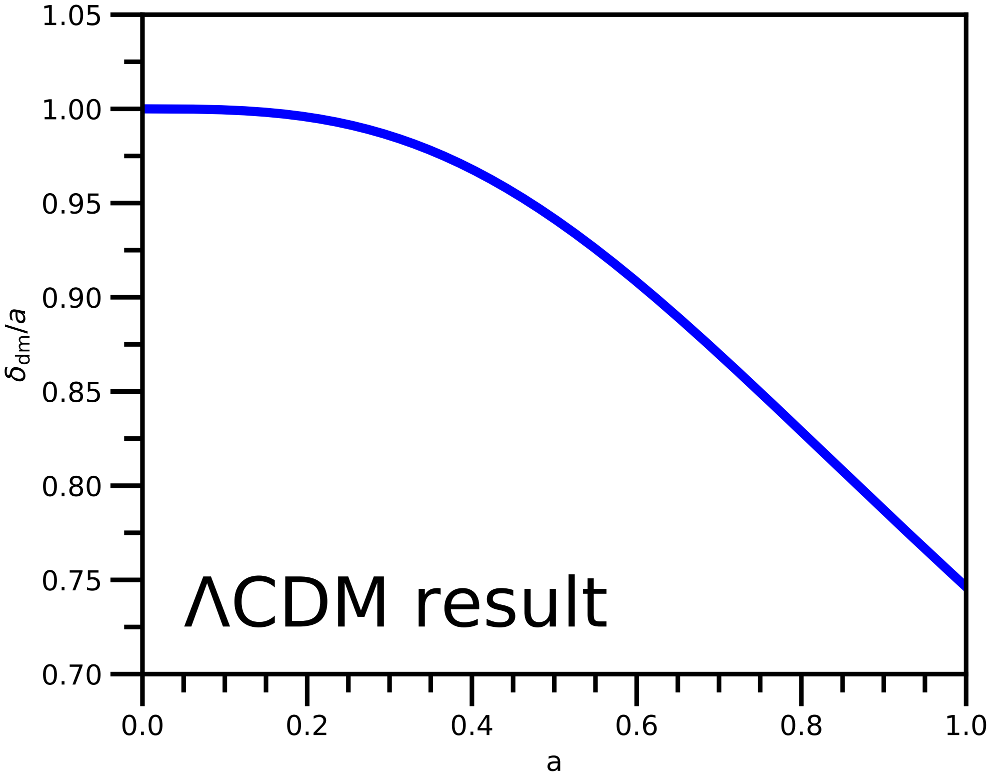

Figure 1.9: Plot of $\delta_{\rm dm}/a$ as a function of a. As initial conditions to solve Eq. (1.66) numerically, we have used $\delta_{\rm dm}(a \simeq 10^{-3}) = a$ and $\delta'_{\rm dm}(a \simeq 10^{-3}) = 1$. The plot is obtained considering $\Omega_{\rm dm} = 0.25$ and $\Omega_{\rm de} = 0.75$.

Once we solved the equation numerically, we are now able to compute the growth rate f, defined as

$$f = \frac{d \ln \delta_{\rm dm}}{d \ln a} = \frac{\delta'_{\rm dm}}{\delta_{\rm dm}} a \ . \tag{1.68}$$

f represents a measure of the matter clustering evolution from the primordial density fluctuations to the large-scale structure observed today.
We expect that the growth rate can be parameterized as

$$f = [\Omega_{\rm dm}]^{\gamma} = \left[\frac{\Omega_{\rm dm} a^{-3}}{\Omega_{\rm de} + \Omega_{\rm dm} a^{-3}}\right]^{\gamma} \ , \tag{1.69}$$

where γ, called growth index, is defined as a constant if we consider dark energy models within General Relativity. In particular, what one finds is that $\gamma \simeq 3(w-1)/(6w-5)$ [30]. For the ΛCDM model, $w = -1$ and so $\gamma = 6/11 \simeq 0.55$ [29], namely

$$f = \left[\frac{\Omega_{\rm dm} a^{-3}}{\Omega_{\rm de} + \Omega_{\rm dm} a^{-3}}\right]^{0.55} \ . \tag{1.70}$$

The result is shown in Fig. 1.10.

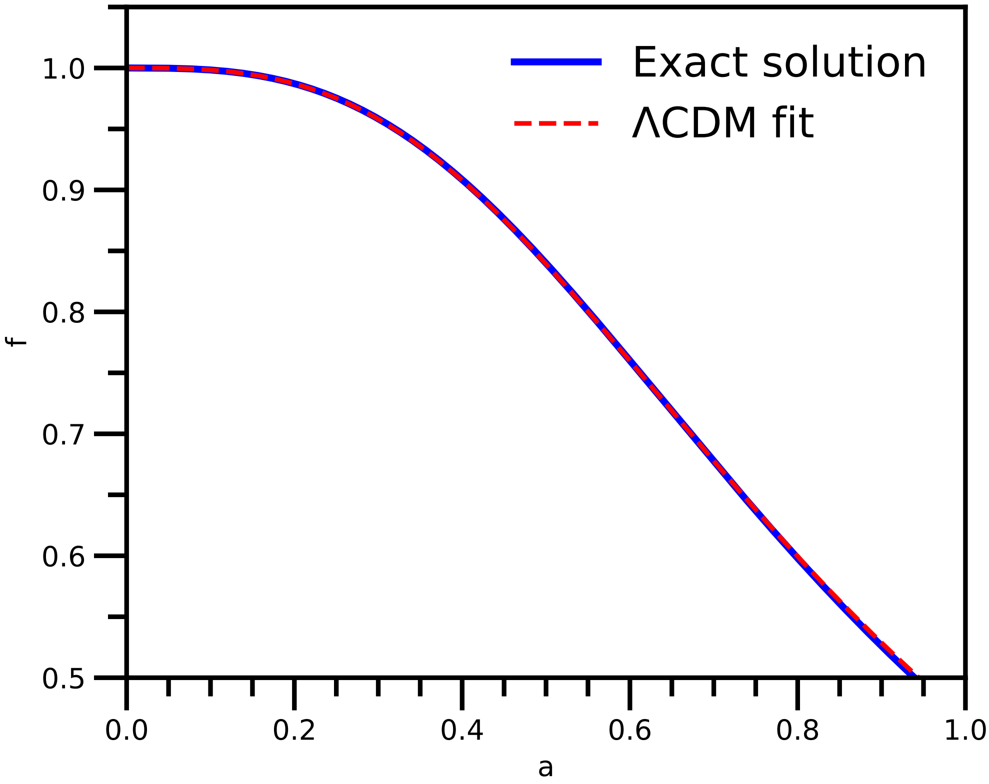

Figure 1.10: Plot of f. The blue solid line is the result obtained considering the numerical result of the differential equation while the red dashed line is obtained from Eq. (1.70). The plot is obtained considering $\Omega_{\rm dm} = 0.25$ and $\Omega_{\rm de} = 0.75$.

Chapter 2

Coupled cosmologies

As reported in the previous chapter, the Planck measurements [1] show that only 5% of the total energy density of the Universe today is related to baryonic matter, 26% comes from dark matter and the remaining 69% comes from dark energy, which is described by a cosmological constant in the ΛCDM model. It is difficult to understand the value of this constant Λ from the quantum field theory approach, as the predicted energy for the vacuum fluctuations is $\sim$120 orders of magnitude larger than the observed value. This is usually referred to as the *cosmological constant problem.*

There is another problem concerning these two dark components of the Universe: the so-called *coincidence problem* (also known as the *why now? problem*) related to the fact that now dark energy and dark matter contribute to the total energy density with the same amount, regardless of their different evolution history.

Possible solutions to these problems are related to the nature of dark energy: one possibility is that dark energy is a dynamical fluid and, for example, the quintessence option consists of a quintessence field which changes with time and varies in space [9].

As a note, all the plots presented in this chapter are obtained using Python codes.

2.1 Dark coupling

Cosmology gives us evidences for the existence of dark energy and dark matter, but we still do not know what they actually are. Since observations allows it, we could extend the ΛCDM model by introducing a new non-gravitational interaction in the dark sector, i.e. between dark energy and dark matter. While the strength of interactions between ordinary matter and the dark energy fields is severely constrained by observations [76], interactions among the dark sectors are still allowed.

For this reason, we explore the idea that the densities of dark matter and dark energy do not evolve independently, but coupled [10]. This "dark coupling", based on models of coupled quintessence [77, 78, 79, 80], could affect significantly the evolution history of the Universe and the density perturbation evolution. Moreover, it could alleviate the coincide problem since the introduction of a coupling could stabilise the ratio of the two dark components during the entire expansion history. These are known as interacting dark energy (IDE) models [9, 10, 11, 12, 13, 14, 15, 16, 17, 18, 19, 20, 21, 22, 23, 24, 25, 26, 27, 28].

To introduce the interaction, we write an additional term in the stress-energy tensor entering Einstein equations. In this coupled scenario, the dark energy and dark matter components of $T^{\mu\nu}$ are no longer separately conserved [9], namely:

$$\nabla_\mu T^\mu_{(\mathrm{dm})\nu} = Q_\nu \ ; \tag{2.1a}$$

$$\nabla_\mu T^\mu_{(\mathrm{de})\nu} = - Q_\nu \ , \tag{2.1b}$$

where the four-vector Q_ν governs the energy-momentum transfer between the dark components. One should notice that the energy-momentum tensor of the whole dark sector, $T^\mu_{(\mathrm{dark})\nu} = T^\mu_{(\mathrm{dm})\nu} + T^\mu_{(\mathrm{de})\nu}$, is still conserved, $\nabla_\mu T^\mu_{(\mathrm{dark})\nu} = 0$.

We consider two families of four momentum-energy transfer Q_ν. In the first family of models (called DEvel), Q_ν is parallel to the dark energy four-velocity, while in the second family of models (called DMvel), Q_ν is parallel to the dark matter four-velocity

$$Q_\nu = Q u_\nu^{(\mathrm{de})}/a \ (\mathrm{DEvel}) \ ; \tag{2.2a}$$

$$Q_\nu = Q u_\nu^{(\mathrm{dm})}/a \ (\mathrm{DMvel}) \ . \tag{2.2b}$$

The scale factor in the denominator is introduced because - at least at linear order - the velocity u is proportional to a, as can be seen in Equation (2.8) [9]. In addition, we introduce the parameter Q, which drives the exchange between dark matter and dark energy.

In DEvel models, there is no momentum transfer to the dark energy frame, i.e. momentum must be conserved in the dark energy frame. This translates in having an extra source of acceleration for the dark matter fluid, appearing in the dark matter velocity perturbation equation. Due to the presence of this additional force felt by dark matter, which violates the equivalence principle, DEvel models are effectively modified gravity models.

In DMvel models, instead, this additional term will not appear since both momentum and energy density are transferred from the dark matter system to the dark energy one. DMvel models are not a modification of gravity, but their growth can be quite different from the growth in a General Relativity dynamical dark energy model which has the same background history, since dark matter does not behave like dust.

Both for DEvel and DMvel models, we introduce two sub-classes of models:

$$Q = \Sigma \rho_{\mathrm{dm}} \ (\text{class I}) \ ; \tag{2.3a}$$

$$Q = \Sigma\rho_{\rm de} \text{ (class II)} \ , \tag{2.3b}$$

where Σ is the interaction rate. One must keep in mind that other possibilities for the coupling, which do not belong to this classification can be used as well, i.e. this classification should be considered as a "basis set".
The expansion history does not depend on the choice of DEvel or DMvel models, but does depend on the form of Q. Unfortunately, we can write an analytic form for the expansion history only with the choice $Q = \xi\mathcal{H}\rho_{\rm de}$ or $Q = \xi\mathcal{H}\rho_{\rm dm}$, where ξ and the equation of state parameter w are constants [9]. Generically, the explicit expression for the coupling Q is purely phenomenologically motivated.

2.2 Background evolution

The evolution equations for the dark matter and dark energy background energy densities are given by [10]

$$\dot{\rho}_{\rm dm} + 3\mathcal{H}\rho_{\rm dm} = Q \ ; \tag{2.4a}$$

$$\dot{\rho}_{\rm de} + 3\mathcal{H}\rho_{\rm de}(1+w) = -Q \ , \tag{2.4b}$$

where dot represents derivative with respect to conformal time τ ($d/d\tau$), w is the dark energy equation of state parameter ($w = P_{\rm de}/\rho_{\rm de}$) and we assume dark matter to be pressureless ($w_{\rm dm} = 0$).
The sign of Q determines the direction of energy transfer: if Q is positive, energy flows from the dark energy system to the dark matter one; if Q is negative, the flow is reversed [9]. Moreover, a positive (negative) Q contribute as an effective negative (positive) pressure in the dark matter background equation, leading to less (more) dark matter in the past (with respect to the uncoupled case). As a consequence, the matter-radiation equality will happen later (earlier) on [10].
From Eqs. (2.4a) and (2.4b) we can also see that dark matter and dark energy, due to the presence of the coupling, will have an extra contribution to their effective equation of state

$$w_{\rm dm}^{eff} = -\frac{Q}{3\mathcal{H}\rho_{\rm dm}} \ ; \tag{2.5a}$$

$$w_{\rm de}^{eff} = w + \frac{Q}{3\mathcal{H}\rho_{\rm de}} \ . \tag{2.5b}$$

The deceleration parameter still satisfies the very same relation than in the uncoupled case

$$q = -\frac{\dot{\mathcal{H}}}{\mathcal{H}^2} = \frac{1}{2}(1 + 3w\Omega_{\mathrm{de}}) \ , \tag{2.6}$$

so we still need to require $w < -1/3$ to have an accelerated expansion.
Having stated the general result equations, we can now consider a particular case, namely we consider a coupling Q given by $Q = \xi \mathcal{H} \rho_{\mathrm{de}}$, where $\mathcal{H}$ governs the time dependence of the interaction rate. With this particular choice for Q, an analytical solution of the background evolution equations can be found [10]:

$$\rho_{\mathrm{dm}} = \rho_{\mathrm{dm}}^{(0)} a^{-3} + \rho_{\mathrm{de}}^{(0)} \frac{\xi}{3w_{\mathrm{de}}^{eff}} (1 - a^{-3w_{\mathrm{de}}^{eff}}) a^{-3} \ ; \tag{2.7a}$$

$$\rho_{\mathrm{de}} = \rho_{\mathrm{de}}^{(0)} a^{-3(1+w_{\mathrm{de}}^{eff})} \ . \tag{2.7b}$$

While the dark energy density ρ_{de} is always positive during the cosmic evolution, we must fix some conditions in order to have the same for ρ_{dm}: all values of $w < 0$ are acceptable for $\xi < 0$, but if $\xi > 0$, we must impose that $\xi \lesssim -w$ [10].
To solve these equations with the proper background conditions, we use the publicly available code `CLASS` (Cosmic Linear Anisotropy Solving System)[2] [31, 32], modifying it to introduce this coupled scenario (the modified part of the code can be found in the Appendix A). Solving the background evolution, we obtain the value of ρ_{dm} and ρ_{de} for different values of the coupling as a function of a. The relative densities ($\Omega_{\mathrm{dm,de}}/\Omega_{\mathrm{tot}}$, with $\Omega_{\mathrm{tot}} = \Omega_{\mathrm{dm}} + \Omega_{\mathrm{de}}$) obtained for different couplings are shown in Figure 2.1: it is evident that their evolution changes as the value of the coupling changes.

2.3 Perturbation theory in coupled cosmologies

The presence of the dark coupling will also affect the evolution of the dark matter and dark energy density perturbations, δ_{dm} and δ_{de}, as well as the divergences of their proper velocities, θ_{dm} and θ_{de}.
Considering the perturbed line element (1.50), we obtain that the four-velocity is given by

$$u_\nu = a(-(1+\psi), v_i) \ . \tag{2.8}$$

The continuity and Euler equations for the coupled dark matter and dark energy components, at linear order, are given by [9]

---

[2] The unmodified version of the codes is public available and can be found at this link: `https://github.com/lesgourg/class_public`

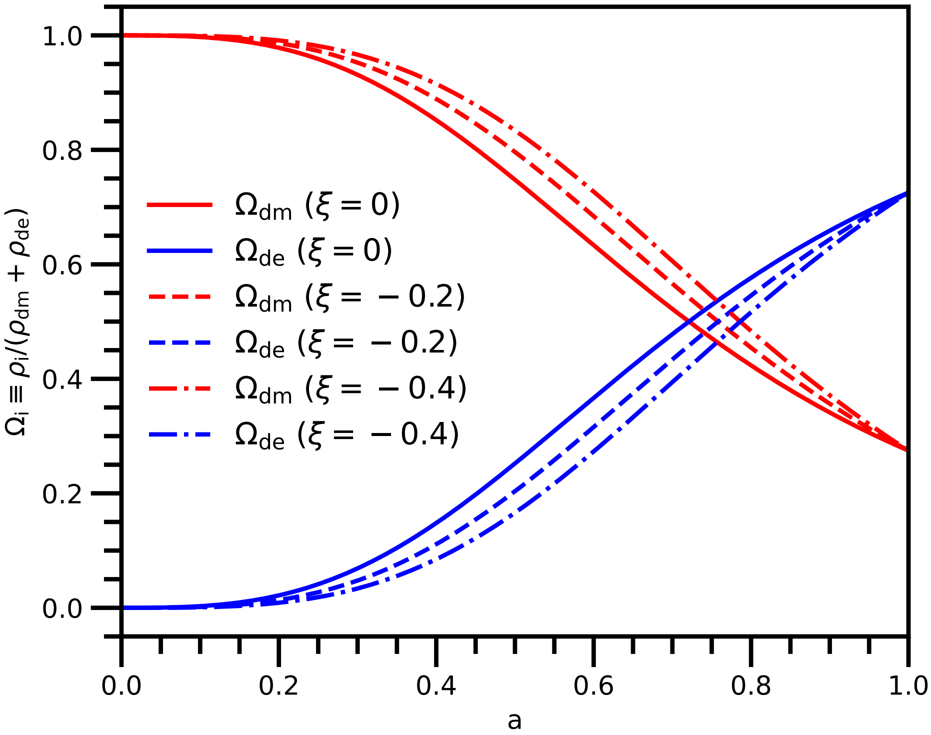

Figure 2.1: Plot of the relative energy densities (i.e. $\Omega_{\rm dm,de}/\Omega_{\rm tot}$, with $\Omega_{\rm tot} = \Omega_{\rm dm} + \Omega_{\rm de}$) for dark matter (red lines) and dark energy (blue lines). In particular, we consider three different values for the coupling: $\xi = 0$ (solid lines); $\xi = -0.2$ (dashed lines); $\xi = -0.4$ (dash-dotted lines). We push the value of the coupling in this plot way beyond the allowed values (as can be seen in Fig. 2.9). The results are obtained using a suitable modified version of `CLASS` [31, 32], whose output is consistent with the one that we obtain solving numerically the background evolution equations (2.4a) and (2.4b) in Python.

$$\dot{\delta}_{\rm dm} = -\left(\theta_{\rm dm} - 3\dot{\phi}\right) + \frac{Q}{\rho_{\rm dm}}\left(\frac{\delta Q}{Q} - \delta_{\rm dm} + \psi\right) \; ; \tag{2.9a}$$

$$\dot{\theta}_{\rm dm} = -\mathcal{H}\theta_{\rm dm} + (1-b)\frac{Q}{\rho_{\rm dm}}(\theta_{\rm de} - \theta_{\rm dm}) + k^2\psi \; ; \tag{2.9b}$$

$$\begin{aligned}\dot{\delta}_{\rm de} = &-(1+w)(\theta_{\rm de} - 3\dot{\phi}) - \frac{Q}{\rho_{\rm de}}\left(\frac{\delta Q}{Q} - \delta_{\rm de} + \psi\right) \\ &- 3\mathcal{H}(\hat{c}^2_{sde} - w)\left[\delta_{\rm de} + \mathcal{H}\left(3(1+w) + \frac{Q}{\rho_{\rm de}}\right)\frac{\theta_{\rm de}}{k^2}\right] \; ;\end{aligned} \tag{2.9c}$$

$$\dot{\theta}_{\rm de} = -\mathcal{H}\left(1 - 3\hat{c}^2_{sde} - \frac{\hat{c}^2_{sde} + b}{1+w}\frac{Q}{\mathcal{H}\rho_{\rm de}}\right)\theta_{\rm de} + \frac{k^2}{1+w}\hat{c}^2_{sde}\delta_{\rm de}$$

$$+ k^2\psi - b\frac{Q}{\rho_{\rm de}}\frac{\theta_{\rm dm}}{1+w} \ , \tag{2.9d}$$

where $b = 0$ refers to DEvel models and $b = 1$ refers to DMvel models, $\hat{c}^2_{sde}$ is the dark energy pressure perturbation sound speed in the rest frame of the dark energy, defined such that [10]

$$\delta p_{\rm de} = \hat{c}^2_{sde}\delta\rho_{\rm de} + (\hat{c}^2_{sde} - \hat{c}^2_{ade})\dot{\rho}_{\rm de}\frac{\theta_{\rm de}}{k^2} \ . \tag{2.10}$$

$\hat{c}^2_{ade}$ is the so-called adiabatic sound speed and it is defined as $\hat{c}^2_{ade} = \dot{p}_{\rm de}/\dot{\rho}_{\rm de}$. In the case of a constant equation of state parameter w, $\hat{c}^2_{ade} = w$. We assume $\hat{c}^2_{sde} = 1$, in such a way that we can neglect dark energy perturbations, as they will not cluster significantly, in the perturbation evolution. Another consideration we can make is that the Euler equation for dark matter is only modified for DEvel models, violating the weak equivalence principle.

When considering these coupled models, one must be careful as it is well known that there could be the appearance of non adiabatic, early time instabilities, as reported for example in [10, 15]. The onset of non-adiabatic instabilities depends on the form of the dark coupling (DEvel or DMvel and class I or class II, with a stronger dependence on this second distinction) and on the equation of state parameter w. We introduce a doom factor $\mathbf{d}$ [10], defined independently of the dark coupling scenario one chooses, as

$$\mathbf{d} = \frac{Q}{3\mathcal{H}\rho_{\rm de}(1+w)}. \tag{2.11}$$

Since for $\mathbf{d}>1$ large-scale instabilities could arise, we consider as viable only those models for which the doom factor is always negative, i.e. $\xi < 0$ and $w > -1$ or $\xi > 0$ and $w < -1$ [10].

The growth equation for dark matter can easily be derived from Eqs. (2.4a), (2.4b), (2.9a) and (2.9b) going to the Newtonian limit (i.e. $k \gg \mathcal{H}$). The result of this calculation is very sensible to the type of coupling.

The simplest case is obtained for DMvel class I, $Q \propto \rho_{\rm dm}$, coupled models, for which we simply recover the result obtained in the uncoupled case, i.e.

$$\delta''_{\rm dm} = -(2-q)\frac{\delta'_{\rm dm}}{a} + \frac{3\Omega_{\rm dm}}{2}\frac{\delta_{\rm dm}}{a^2}, \tag{2.12}$$

and the difference between non interacting cosmologies arise exclusively due to the different background evolution of $\mathcal{H}$ and $\Omega_{\rm dm}$. The prime appearing in Eq. (2.12) represents derivatives with respect to a.

For all other cases, i.e. DMvel class II and DEvel class I and II, the dark matter linear perturbation equations and the growth equations will both depend on the coupling term, so in order to obtain them we must give an explicit form for the interaction term Q.

To obtain the growth equation for dark matter, we will consider, as we did in the previous section, $Q = \xi\mathcal{H}\rho_{\rm de}$, where ξ is a constant. Neglecting the dark energy perturbations ($\hat{c}^2_{sde}$ = 1), using the form of Q given above and working in the Newtonian limit, Eqs. (2.9a) and (2.9b) reduce to

$$\dot{\delta}_{\rm dm} = -\,\theta_{\rm dm} - \xi\mathcal{H}\frac{\rho_{\rm de}}{\rho_{\rm dm}}\delta_{\rm dm}\ ; \tag{2.13a}$$

$$\dot{\theta}_{\rm dm} = -\,\mathcal{H}\theta_{\rm dm} - (1-b)\xi\mathcal{H}\frac{\rho_{\rm de}}{\rho_{\rm dm}}\theta_{\rm dm} + k^2\psi\ . \tag{2.13b}$$

Taking the derivative of Eq. (2.13a), using Eq. (2.13b) and $k^2\psi = -4\pi G a^2\rho_{\rm dm}\delta_{\rm dm}$, what we obtain is

$$\begin{aligned}&\ddot{\delta}_{\rm dm} - \mathcal{H}\theta_{\rm dm} - (1-b)\xi\mathcal{H}\frac{\rho_{\rm de}}{\rho_{\rm dm}}\theta_{\rm dm} - 4\pi G a^2\rho_{\rm dm}\delta_{\rm dm} + \xi\dot{\mathcal{H}}\frac{\rho_{\rm de}}{\rho_{\rm dm}}\delta_{\rm dm}\\ &+\xi\mathcal{H}\left(\frac{\dot{\rho}_{\rm de}\rho_{\rm dm} - \rho_{\rm de}\dot{\rho}_{\rm dm}}{\rho^2_{\rm dm}}\right)\delta_{\rm dm} + \xi\mathcal{H}\frac{\rho_{\rm de}}{\rho_{\rm dm}}\dot{\delta}_{\rm dm} = 0\ .\end{aligned} \tag{2.14}$$

Using again Eq. (2.13a) to get rid of $\theta_{\rm dm}$, we are left with an equation only for $\delta_{\rm dm}$, namely

$$\begin{aligned}&\ddot{\delta}_{\rm dm} + \mathcal{H}\dot{\delta}_{\rm dm} + \xi\mathcal{H}^2\frac{\rho_{\rm de}}{\rho_{\rm dm}}\delta_{\rm dm} + (1-b)\xi\mathcal{H}\frac{\rho_{\rm de}}{\rho_{\rm dm}}\left(\dot{\delta}_{\rm dm} + \xi\mathcal{H}\frac{\rho_{\rm de}}{\rho_{\rm dm}}\right) - 4\pi G a^2\rho_{\rm dm}\delta_{\rm dm}\\ &+\xi\dot{\mathcal{H}}\frac{\rho_{\rm de}}{\rho_{\rm dm}}\delta_{\rm dm} + \xi\mathcal{H}\left(\frac{\dot{\rho}_{\rm de}\rho_{\rm dm} - \rho_{\rm de}\dot{\rho}_{\rm dm}}{\rho^2_{\rm dm}}\right)\delta_{\rm dm} + \xi\mathcal{H}\frac{\rho_{\rm de}}{\rho_{\rm dm}}\dot{\delta}_{\rm dm} = 0.\end{aligned} \tag{2.15}$$

As we did in the uncoupled case, we want to go from having derivatives with respect to τ to have derivatives with respect to the scale factor $a(\tau)$. Using Eq. (1.61), the result is

$$\begin{aligned}&\delta''_{\rm dm} + \left[\frac{2}{a} + \frac{\mathcal{H}'}{\mathcal{H}} + \frac{\xi(2-b)}{a}\frac{\rho_{\rm de}}{\rho_{\rm dm}}\right]\delta'_{\rm dm} + \left[\frac{\xi}{a^2}\frac{\dot{\mathcal{H}}}{\mathcal{H}}\frac{\rho_{\rm de}}{\rho_{\rm dm}} + \frac{\xi}{a^2\mathcal{H}}\left(\frac{\dot{\rho}_{\rm de}\rho_{\rm dm} - \rho_{\rm de}\dot{\rho}_{\rm dm}}{\rho^2_{\rm dm}}\right)\right.\\ &\left.-\frac{4\pi G}{\mathcal{H}^2}\rho_{\rm dm} + \frac{\xi}{a^2}\frac{\rho_{\rm de}}{\rho_{\rm dm}} + (1-b)\frac{\xi^2}{a^2}\frac{\rho^2_{\rm de}}{\rho^2_{\rm dm}}\right]\delta_{\rm dm} = 0\ ,\end{aligned} \tag{2.16}$$

where we divided by $a^2\mathcal{H}^2$. Now, using Eqs. (2.4a) and (2.4b) to get rid of the derivatives of the energy densities, introducing, with the tricks used in the uncoupled case (see Eq. (2.6)), the deceleration parameter q and the density parameter for dark matter $\Omega_{\rm dm}$ (see Eq. (1.65)), we obtain

$$\delta''_{\rm dm} + \left[\frac{2-q}{a} + \frac{\xi(2-b)}{a}\frac{\rho_{\rm de}}{\rho_{\rm dm}}\right]\delta'_{\rm dm} + \left[-\frac{q\xi}{a^2}\frac{\rho_{\rm de}}{\rho_{\rm dm}} - \frac{3w\xi}{a^2}\frac{\rho_{\rm de}}{\rho_{\rm dm}} - \frac{\xi^2}{a^2}\frac{\rho_{\rm de}}{\rho_{\rm dm}} \right.$$
$$\left. -\frac{\xi^2}{a^2}\frac{\rho^2_{\rm de}}{\rho^2_{\rm dm}} - \frac{3\Omega dm}{2a^2} + \frac{\xi}{a^2}\frac{\rho_{\rm de}}{\rho_{\rm dm}} + (1-b)\frac{\xi^2}{a^2}\frac{\rho^2_{\rm de}}{\rho^2_{\rm dm}}\right]\delta_{\rm dm} = 0 \ . \tag{2.17}$$

Rearranging all of the terms, we finally find that the result we were looking for, so the growth equation for dark matter perturbations in the Newtonian limit, is given by

$$\delta''_{\rm dm} = -B\frac{\delta'_{\rm dm}}{a} + \frac{3}{2}A\Omega_{\rm dm}\frac{\delta_{\rm dm}}{a^2} \ , \tag{2.18}$$

where

$$A = 1 + \frac{2}{3}\frac{1}{\Omega_{\rm dm}}\frac{\rho_{\rm de}}{\rho_{\rm dm}}\left[-\xi(1-q-3w) + \xi^2\left(1 + b\frac{\rho_{\rm de}}{\rho_{\rm dm}}\right)\right] \ ; \tag{2.19a}$$

$$B = 2 - q + (2-b)\xi\frac{\rho_{\rm de}}{\rho_{\rm dm}} \ . \tag{2.19b}$$

As before, $b = 0$ is the case of DEvel models while $b = 1$ is the case of DMvel models. From now on, we shall consider $b = 1$, therefore we shall focus on a specific DMvel model.

2.4 Growth factor f

The growth factor f, as defined in the previous chapter in Eq. (1.68), is an important parameter to consider as, not only is sensitive to modifications of General Relativity, but can give us information about departures from the ΛCDM model, which is what we are interested in.

As we did in the uncoupled scenario, we would like to find a way to parameterise f. Starting from the known result in Eq. (1.70), true in the ΛCDM model, we try to find how the presence of a coupling modifies it. The most simple parametrisation for the fitting function to f is the following one:

$$f(\xi) = \left[\frac{\Omega_{\rm dm}}{\Omega_{\rm dm} + \Omega_{\rm de}}\right]^{\gamma_0(\xi) + a\gamma_1(\xi) + a^2\gamma_2(\xi)} \ . \tag{2.20}$$

To explicitly derive the dependence of the $\gamma_{\rm i}$'s on the coupling, as this is what we would like to see, we did a plot of them as a function of the coupling, shown in Fig. 2.2, and then tried to do a fit to these curves.

The best fitting function to all of the $\gamma_{\rm i}(\xi)$, i = 0, 1, 2, is found to be given by a polynomial of sixth order in the coupling, namely

$$\gamma_{\rm i}(\xi) = a_{\rm i} + b_{\rm i}\xi + c_{\rm i}\xi^2 + d_{\rm i}\xi^3 + e_{\rm i}\xi^4 + f_{\rm i}\xi^5 + g_{\rm i}\xi^6. \tag{2.21}$$

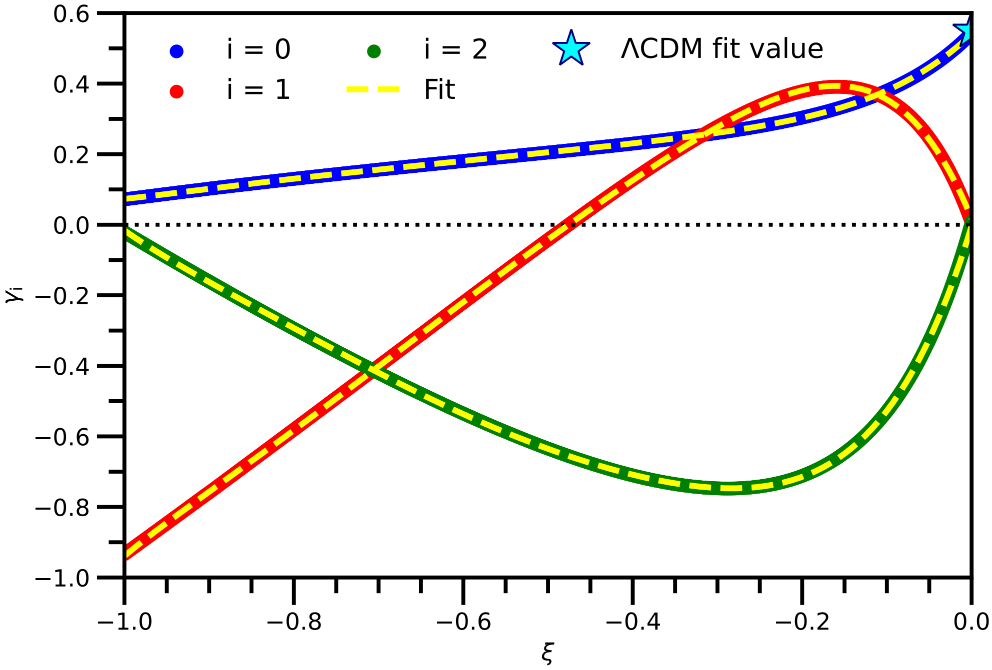

Figure 2.2: Plot of the three $\gamma_i(\xi)$ in Eq. (2.20) as a function of the coupling. The dark yellow star represents the value of the uncoupled case, i.e. $\gamma = 0.55$, while the yellow dashed line is the fit given by Eq. (2.21). This plot is obtained considering $\Omega_{dm} = 0.25$ and $\Omega_{de} = 0.75$.

The results of this fitting procedure are shown in Fig. 2.2 and in Tab. 2.1, which shows the values of the fitting coefficients. From the plot, it is possible to notice that γ_0 converges to the value of the ΛCDM parametrization, i.e. to 0.55 (the cyan star), when the coupling goes to zero, while the other γ_i, i $\neq$ 0, converge to 0: this is consistent with the fact that when the coupling ξ is zero, we should recover the uncoupled scenario result, Eq. (1.70).

i	a_i	b_i	c_i	d_i	e_i	f_i	g_i
0	0.541	2.259	8.215	18.320	23.180	15.518	4.235
1	0.017	-5.877	-31.240	-70.487	-90.224	-60.824	-16.681
2	-0.004	7.858	32.350	69.457	87.636	58.768	16.084

Table 2.1: Values of the coefficients appearing in the parametrisation of the γ_i's, as reported in Eq. (2.21). These values are obtained using a Python code, considering $\Omega_{dm} = 0.25$ and $\Omega_{de} = 0.75$.

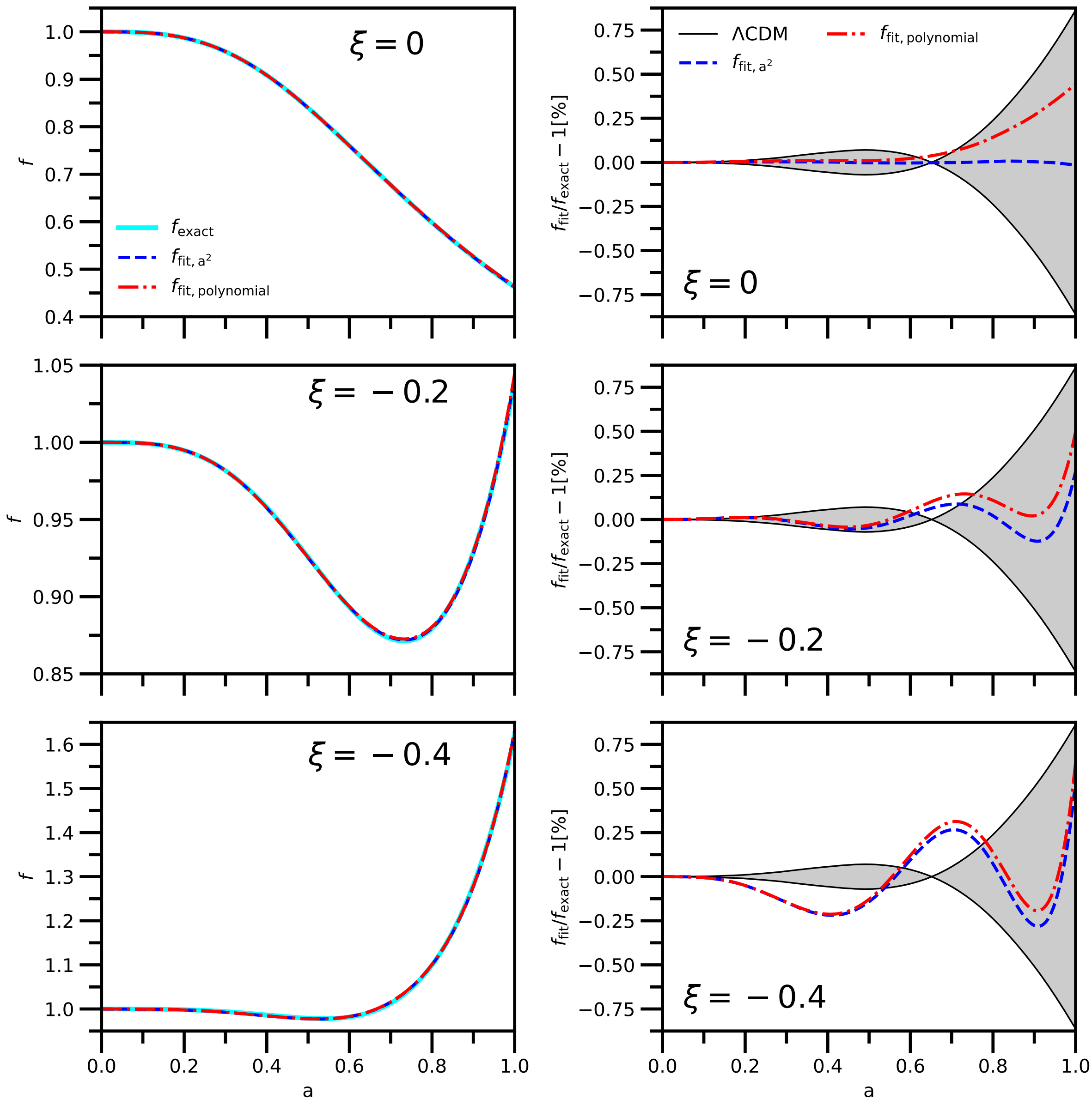

Figure 2.3: Left panels: fitting function and numerical solutions for f (light blue solid line), for three different values of the coupling. Right panels: relative deviations. The grey area represents the deviation for the uncoupled case, that we consider as a bound for the deviations in the coupled case. In all plots, the blue dashed line ('a^2') depicts the exact fit using Eq. (2.20), while the red dash-dotted line ('polynomial') uses the polynomial approximation to the exact fit, see Eq. (2.21). These plots are obtained considering $\Omega_{\mathrm{dm}} = 0.25$ and $\Omega_{\mathrm{de}} = 0.75$.

All of the above results are obtained working in the simplified case in which we consider, as components of the Universe, only dark matter and dark energy, with fixed values for

$\Omega_{\rm dm}$ and $\Omega_{\rm de}$, namely $\Omega_{\rm dm} = 0.25$ and $\Omega_{\rm de} = 0.75$. However, to be more precise, one should also take into account the baryonic component in the evolution of the Universe by considering $\Omega_{\rm m}$ (instead of $\Omega_{\rm dm}$), i.e. $\Omega_{\rm m} = \Omega_{\rm b} + \Omega_{\rm dm}$ is the sum of the energy densities of baryons and dark matter (this is precisely what `CLASS` [31, 32] does). Fig. 2.3 depicts how both the exact fit using Eq. (2.20) and that in which the coefficients of Eq. (2.20) are assumed to follow a 6th order polynomial function (see Eq. (2.21)), compare to the numerical solution for f, for three different values of the coupling ξ. We also show the relative deviations, i.e. the ratio between the fit function and the exact solution (minus one), obtained numerically with Python codes. The result is shown in Fig. 2.3 as well.

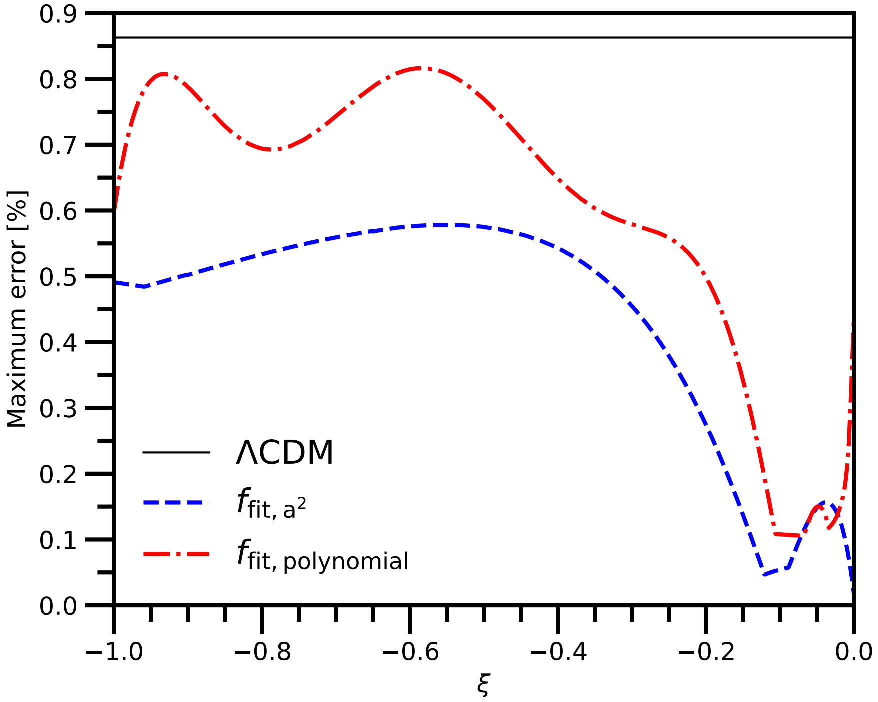

Figure 2.4: Plot of the maximum error for the parametrisation considered, both without the explicit expressions for the $\gamma_{\rm i}$'s (blue dash-dotted line), Eq. (2.20), and with that result (red dashed line), Eq. (2.21), as a function of the coupling. This plot is obtained considering $\Omega_{\rm dm}$ = 0.25 and $\Omega_{\rm de} = 0.75$.

The maximum error obtained for each parametrisation is given in Fig. 2.4. It is possible to see that, in both cases, the maximum deviation is always smaller than the one in the uncoupled case, that we take as a bound.

We notice that this parametrisation for f, differently for the result obtained in the uncoupled case (Eq. (1.70)), is not independent on the value of $\Omega_{\rm dm}$, as can be seen in Fig. 2.5. Nonetheless, for small deviations from the value of $\Omega_{\rm dm}$ for which the parametrisation is obtained, i.e. $\Omega_{\rm dm} = 0.25$, we find that the relative deviations are always smaller than the smallest error associated to the reference value of $[f\sigma_8](z)$ reported in Tab. 1.2, as can be seen in Figure 2.5. However, to get a more complete and correct result, one should consider this dependence in the parametrisation for f.

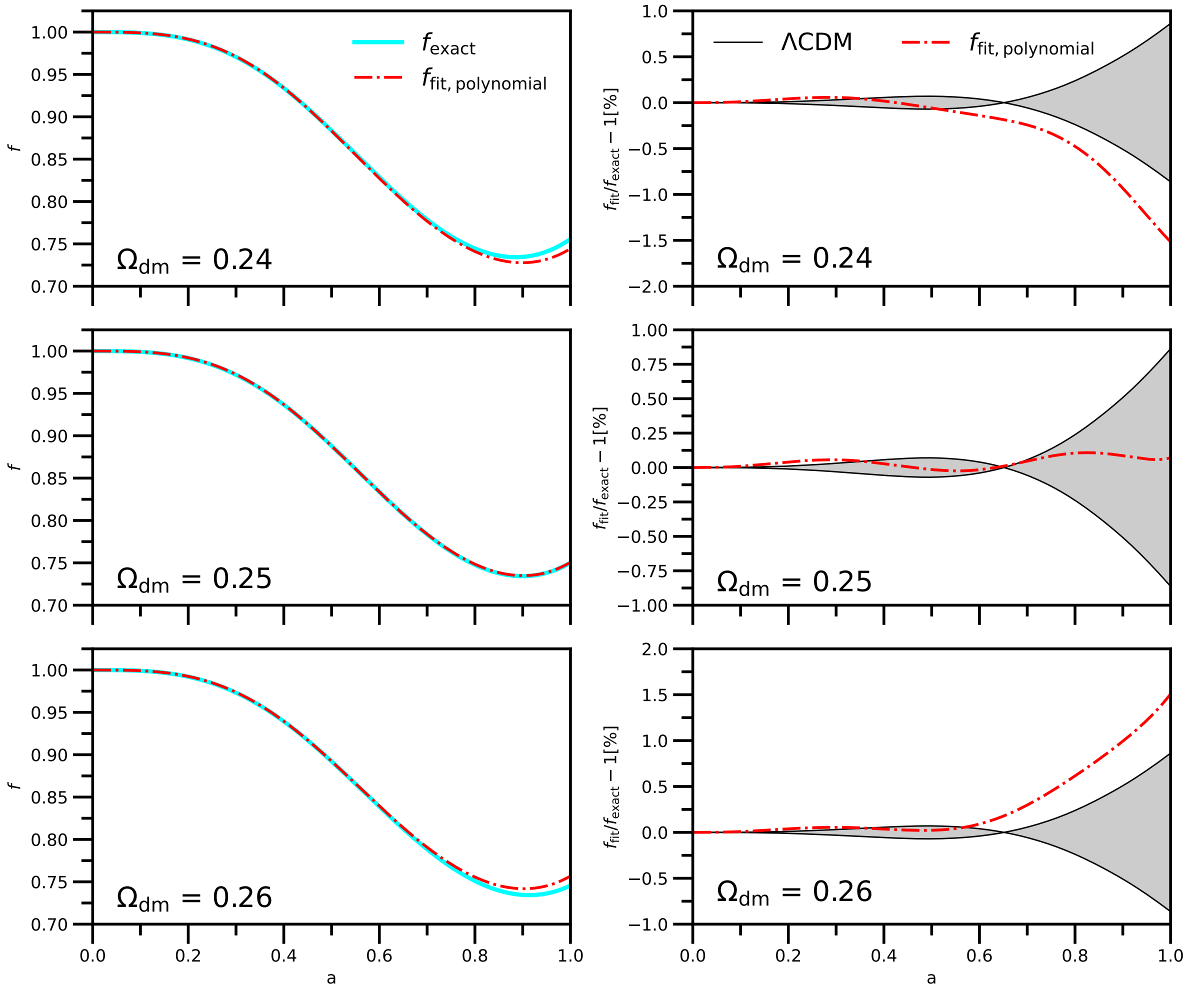

Figure 2.5: Plot of the f function (left plots) and of the relative deviations (right plots), considering small deviations from $\Omega_{\rm dm} = 0.25$, fixing the coupling to $\xi = -0.1$. The gray area represents the deviation for the uncoupled case, that we consider as a bound for the deviations in the coupled case. The red-dashed line (labelled 'polynomial') represent the fit line obtained the value of the coefficients of the fit function reported in Tab. 2.1, obtained using $\Omega_{\rm dm} = 0.25$.

2.5 σ_8

Given the fact that we shall also employ observations of the clustering parameter $f\sigma_8$, we also consider how the value of σ_8 changes as the coupling ξ does. For simplicity, as σ_8

is indeed a function of the redshift z, we have only considered the value of this parameter today ($z = 0$), $\sigma_{8,0} = \sigma_8(z = 0)$. The results, taken as an output of `CLASS` [31, 32], are presented in Tab. 2.2.

ξ	$\sigma_{8,0}$
0.00	0.823
-0.05	0.874
-0.10	0.924
-0.15	0.973
-0.20	1.021
-0.25	1.068
-0.30	1.114
-0.35	1.159
-0.40	1.203
-0.45	1.246
-0.50	1.288
-0.55	1.329
-0.60	1.369
-0.65	1.409
-0.70	1.447
-0.75	1.485
-0.80	1.522
-0.85	1.558
-0.90	1.594
-0.95	1.628
-1.00	1.662

Table 2.2: Values of $\sigma_{8,0}$, obtained from `CLASS` [31, 32], for different values of the coupling ξ.

Using these data, we try to find a fitting function. In this case, we consider two different parametrisations: in the first one we impose the condition that $\sigma_{8,0}(\xi = 0)$ is equal to the value obtained in the output from `CLASS` [31, 32]:

$$\sigma_{8,0}(\xi) = 0.823 + \alpha_1 \, \xi + \alpha_2 \, \xi^2 \ , \tag{2.22}$$

while in second one, we leave it as a free parameter:

$$\sigma_{8,0}(\xi) = \beta_0 + \beta_1 \, \xi + \beta_2 \, \xi^2 \ . \tag{2.23}$$

The value of the coefficients are presented in Tab. 2.3, while the plots showing how the fitting functions compare to the "exact" solution and the relative deviations are reported in Figs. 2.6 and 2.7, respectively.

α_1	α_2
-1.022	-0.185

β_0	β_1	β_2
0.824	-1.019	-0.182

Table 2.3: Values of the coefficients appearing in the two different parametrisations of $\sigma_{8,0}$, as reported in Eq. (2.22) (left table) and Eq. (2.23) (right table).

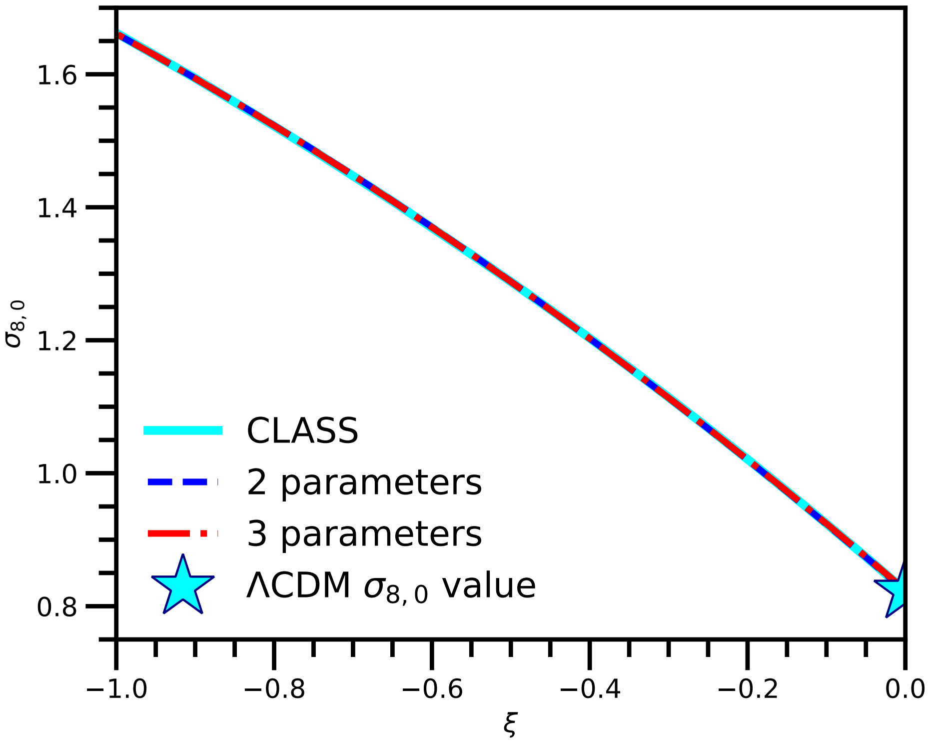

Figure 2.6: Fit to the $\sigma_{8,0}$ values, obtained as an output of `CLASS` [31, 32], as a function of the coupling ξ. The solid cyan line is the exact result, the blue dashed line corresponds to eq. (2.22) with the coefficients shown in the left part of Table 2.3 while the red dot-dashed line corresponds to eq. (2.23) with the coefficients shown in the right part of Table 2.3.

2.6 $f\sigma_8$

The observational values of $[f\sigma_8](z)$ are the ones reported in Tab. 1.2. To check the consistency of the `CLASS` [31, 32] output, we tried to recreate the right plot of Fig. 1.8, finding that the output of the public available `CLASS` perfectly recreates the black solid line.

We then change the value of the coupling, fixing $\Omega_{\rm dm}$ to the value $\Omega_{\rm dm} = 0.25$ [3]. We also

---

[3] We shall see that this generates a small difference with the standard `CLASS` output since the best fit-value for $\Omega_{\rm dm}$ from Planck18 [1] is slightly different.

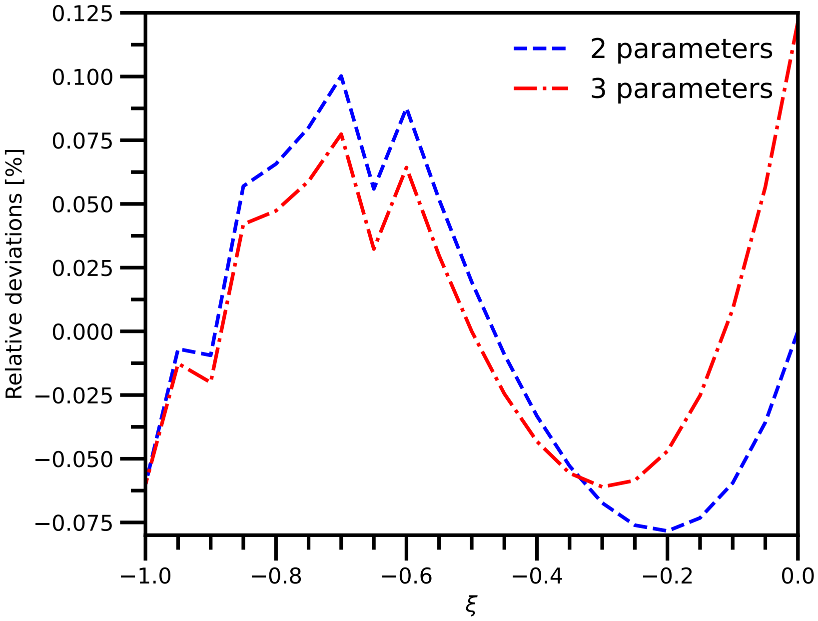

Figure 2.7: Relative deviation for the two fitting functions considered, namely Eqs. (2.22) and (2.23). The behaviour is not smooth due to having considered only few values of the coupling.

obtain the very same plot fixing the coupling ξ to the value $\xi = -0.1$ and changing $\Omega_{\rm dm}$. These results are reported in Fig. 2.8.
The values of $\Omega_{\rm dm}$ and ξ are chosen accordingly to the χ^2 contour plot in the $(\Omega_{\rm dm},\, \xi)$ plane obtained with a Python code and shown in Fig. 2.9.
Now that we have implemented our model numerically and we have also developed an analytical expression for the growth factor, we are ready to compute the χ^2 analysis of the $[f\sigma_8](z)$ quantity to test the validity of the growth formula derived here.
The χ^2 function reads as:

$$\chi^2 = \sum_{i=1}^{N} \left[\frac{[f\sigma_8]^{(theo)}(z_i) - [f\sigma_8]^{(obs)}(z_i)}{\sigma^{(obs)}_{f\sigma_8}(z_i)} \right]^2 , \tag{2.24}$$

where the subscript (obs) refers to the observational values in Tab. 1.2, while the subscript $(theo)$ refers to the values obtained either analytically or from `CLASS` [31, 32]. To the values obtained using this formula, we subtract the minimum value of the χ^2 function that we have.
The results from the χ^2 analysis are shown in Fig. 2.9, where it is shown the best fit point (the yellow circle in the plot), given by $(\Omega_{\rm dm},\, \xi) = (0.248,\, 0.0)$, and therefore explaining the choice of the value of $\Omega_{\rm dm}$ fixed to $\Omega_{\rm dm} = 0.25$ to obtain the left plot in

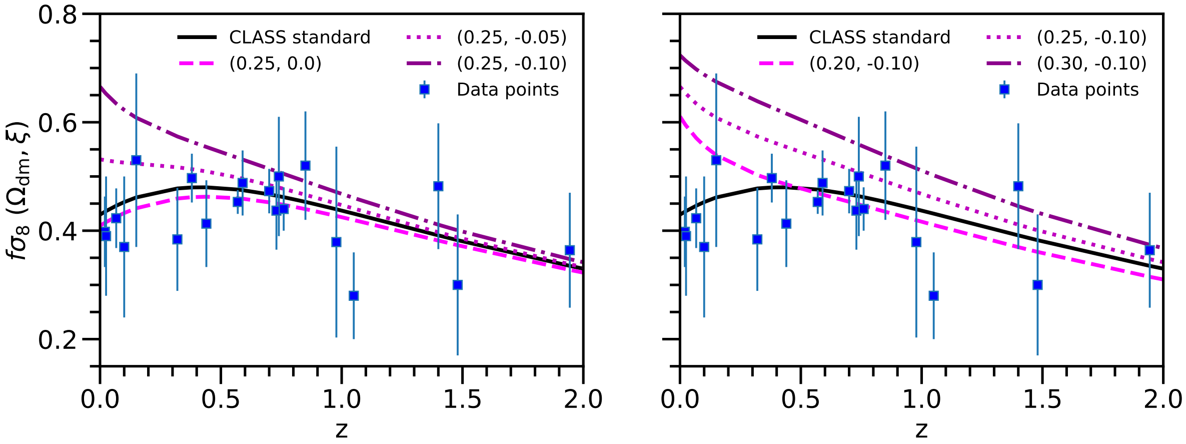

Figure 2.8: These two plots are similar to the right plot of Fig. 1.8. The values in the legend must be interpreted as ($\Omega_{\rm dm}$, ξ). The data points are the ones in Tab. 1.2. The black solid line is obtained considering the unmodified `CLASS` [31, 32], while the other lines are obtained considering our modification of `CLASS` (as reported in Appendix A). Left panel: the different lines are obtained fixing $\Omega_{\rm dm} = 0.25$ and changing the coupling. Right panel: the different lines are obtained fixing the coupling $\xi = -0.1$ and changing $\Omega_{\rm dm}$.

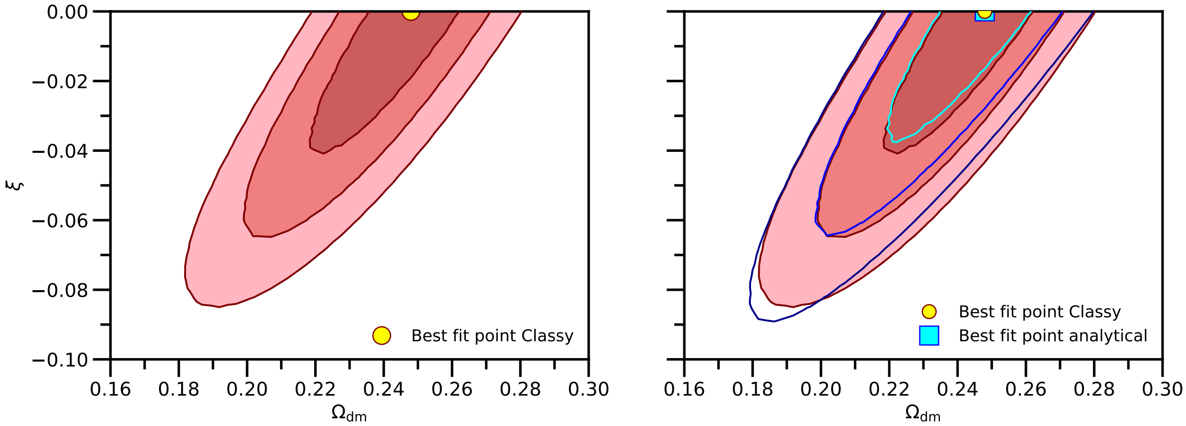

Figure 2.9: Contour plot in the ($\Omega_{\rm dm}$,ξ) plane for the χ^2 for $[f\sigma_8](z)$. Left: contour plot obtained considering $f\sigma_8$ as the output of `CLASS` [31, 32]. Regions from 1σ (darker color) to 3σ (lighter color) are shown. Right: the contour plot obtained considering f from Equations (2.20) and (2.21) and σ_8 as an output of `CLASS` is given by the blue lines shown on top of the left contour plot. In this case, the 1σ line is the lighter color and the 3σ line is the darkest one.

Fig. 2.8. The value of the coupling, $\xi = -0.1$, was instead chosen since it is excluded at 3σ by observations and therefore it can be regarded as an "lower bound" to the value the coupling can take.

In the right plot of Fig. 2.9, one can also see which is the effect of the parametrisation that we obtained for the f factor. Notice that the best fit point of the two contour plots match almost exactly, as well as the 1σ and 2σ regions. The difference that we see is related to the error that we introduce since our parametrisation is actually dependent on $\Omega_{\rm dm}$ (actually on $\Omega_{\rm m}$), as can be seen from Fig. 2.5. The main effect of this dependence is to allow for more negative values of the coupling ξ and for lower values of the dark matter energy density $\Omega_{\rm dm}$. Nevertheless we can conclude that the fitting function used here is perfectly able to reproduce to a very large extent the numerical results.

Chapter 3

Cosmological analysis

ìIn this chapter, we discuss the key role of statistical analysis in the field of cosmology, introducing in particular the concept of Bayesian statistics. We describe how to obtain constraints on the parameter of our model and how to sample them, describing the efficient method of Markov Chain Monte Carlo. We describe the datasets and measurements we are going to use for our analysis and we present the results obtained.

3.1 Statistical methods in cosmology

There is a strong connection between the field of cosmology and that of statistics, in order to understand and analyse all the data collected from observations of our Universe. In particular, the framework of Bayesian statistics, born from the paper published by Reverend Thomas Bayes [81], underlies most of the statistical methods adopted in cosmology.

The Bayesian school of thought is contrasted by the frequentist one. While the frequentist notion of probability is that probabilities are tied to the frequency of outcomes over a long series of trials, therefore repeatability of an experiment is essential, the Bayesian outlook is that probability expresses a degree of belief in a proposition, based on the available knowledge of the experiment, so repeatability is not a key concept [82].

We see that the main difference in these two points of view is that in one case (frequentist) model parameters and hypothesis are fixed, while in the other (Bayesian) the probability of an event changes as new data are considered.

3.1.1 Bayesian statistics

For the purposes of cosmology, we can say that the Bayesian approach can be considered as better to use, for different reasons, among which [82]:

- application of Bayes' theorem recovers frequentist results (in the long run) for cases simple enough where such results exist, while remaining applicable to questions that cannot even be asked in a frequentist context;

- Bayesian inference deals effortlessly with nuisance parameters, which are parameters that, even though they have an effect on the data, we are not interested in;
- prior information can be very relevant in some situations: Bayes' theorem ensures that relevant prior information is accounted for in the final inference;
- it only deals with data that were actually observed.

The whole Bayesian approach rests upon the simple mathematics described by the Bayes theorem [81]. This result is a general one of probability theory, coming from the fact that, for any given two propositions A and B, their joint probability satisfies $P(A, B) = P(B, A)$. This leads to:

$$P(A|B) = \frac{P(B|A)P(A)}{P(B)} \ , \tag{3.1}$$

where $P(A|B)$ is the probability we assign to proposition A conditional on assuming that proposition B is true.
For our purposes, Bayes theorem becomes interesting when A represents the parameters θ of a model and B represents the observed data d, so that

$$P(\theta|d) = \frac{P(d|\theta)P(\theta)}{P(d)} \ . \tag{3.2}$$

Notice that now we are working with continuous random variables, so that the P's are not probabilities but probability distribution functions.
On the left-hand side of Eq. (3.2), $P(\theta|d)$ is the posterior probability for θ, representing our degree of belief about the value of θ after we have seen the data d. On the right-hand side of Eq. (3.2), instead, $P(d|\theta)$ is the likelihood $\mathcal{L}(\theta)$, i.e. the probability of the data given a certain value of the parameters. $P(\theta)$ is the prior probability distribution that represents our degree of belief in the value of θ before we see the data, while $P(d)$ is a normalizing constant (called marginal likelihood or Bayesian evidence) defined as [82]

$$P(d) = \int d\theta P(d|\theta)P(\theta) \ . \tag{3.3}$$

We notice that the Bayesian evidence is independent on the parameters of the model considered.
Bayesian inference works by updating our state of knowledge about a parameter as new data flow in, meaning that the posterior from a previous cycle becomes the prior for the next observations. Essentially, Bayes' theorem can be seen as a guide for how we

gain knowledge from experience: we begin with a certain belief, regardless of the data, represented by $p(\theta)$, and then adjust our belief system once we have taken in the data, resulting in $p(\theta|d)$.

The price that we need to pay is that we need to specify an initial prior (not determined by the theory). Moreover, the final result will inevitably depend on the prior choice. Even though there is no indication as how to choose the prior, a common choice is to take a so-called "flat prior", i.e. a uniform prior [82].

Therefore, the general recipe is:

- choose a model containing a set of parameters θ;
- specify the priors for the parameters: they should summarize your state of knowledge, before considering the new data, about the parameters;
- construct the likelihood function, usually reflecting the way the data are obtained. Nuisance parameters, related to the measurement process, are included in the likelihood;
- obtain the posterior distribution by numerical methods, like MCMC, usually up to an overall normalisation constant.

3.1.2 Markov Chain Monte Carlo (MCMC) methods

In cosmology, we want to apply Bayesian statistics to perform parameter estimation. We have some data d and a model specified by some parameters θ. Each evaluation of the likelihood typically involves a call to Boltzmann solvers (in our case `CLASS` [31, 32]). Evaluating the posterior is done using Bayes theorem (see Eq. (3.3)), but since practically we usually deal with $\mathcal{O}(10)$ parameters, we need a way to improve efficiency by considering a smarter way of sampling. Nowadays the most widely used method is the Markov Chain Monte Carlo (MCMC) method [83].

The purpose of a MCMC algorithm is to construct a sequence of points in parameter space, called chain. The generation of the elements of the chain is probabilistic in nature and is described by a transition probability $T(\theta^{(t)}, \theta^{(t+1)})$. A sufficient condition to obtain a Markov Chain is that the transition probability satisfies the detailed balance condition [82]

$$p(\theta^{(t)}|d)T(\theta^{(t)}, \theta^{(t+1)}) = p(\theta^{(t+1)}|d)T(\theta^{(t)}, \theta^{(t+1)}) \; . \tag{3.4}$$

The simplest MCMC algorithm is the Metropolis-Hastings algorithm [84, 85]. It works as follows:

1. start from a random point $\theta^{(0)}$ with associated posterior probability $p_0 = p(\theta^{(0)}|d)$;

2. propose a candidate point $\theta^{(c)}$ by drawing from the posterior distribution $q(\theta^{(0)}, \theta^{(c)})$;
3. evaluate the posterior at the candidate point $p_c = p(\theta^{(c)}|d)$. Accept the candidate point with probability

$$\alpha = min\left(\frac{p_c q(\theta^{(c)}, \theta^{(0)})}{p_0 q(\theta^{(0)}, \theta^{(c)})}, 1\right) \ . \tag{3.5}$$

   This can be performed by generating a random number u from the uniform distribution [0,1) and accepting the candidate sample if $u < \alpha$, rejecting otherwise;
4. if the candidate point is accepted, add it to the chain and move there, otherwise stay in the old point (which is counted twice) and go back to point number 2.

The choice of proposal distribution q is crucial for the efficient exploration of the posterior. We also notice that, at each step, the next sample depends only on the current sample, and not on the previous ones.
If the posterior distribution is symmetric, i.e. $q(\theta^{(0)}, \theta^{(c)}) = q(\theta^{(c)}, \theta^{(0)})$, the algorithm is called Metropolis (not Metropolis-Hasting), and the acceptance probability simply reduces to

$$\alpha = min\left(\frac{p_c}{p_0}, 1\right) \ . \tag{3.6}$$

An important problem when working with MCMC is the assessment of chain convergence [82], aiming at establishing when the obtained samples are enough so that the estimate is sufficiently accurate. Useful diagnostic tools include, for example, the Gelman and Rubin criterion [86].
MCMC methods are widely used in cosmology and there are several public available codes available, like `Cobaya`[4] [33, 34], used in this work, interfaced with the Boltzmann solver `CLASS` [31, 32].

3.2 Cosmological measurements

In this section we presents the datasets and likelihoods used to put constraints on our model.

---

[4] The codes are public available and can be found at this link: `https://github.com/CobayaSampler/cobaya/tree/master`

3.2.1 CMB measurements

The Planck mission [1, 87, 88] has achieved exceptionally precise measurements of the power spectra of CMB anisotropies. The CMB power spectra contains a vast amount of information. We use as our baseline data set the temperature (TT) and polarisation (EE) auto-spectra, plus their cross-spectra (TE), as incorporated in the `Commander` (for multipoles $\ell < 30$) and `plik` (for multipoles $\ell > 30$) likelihoods from the PR3 release [88]. In addition to the primary temperature and polarization anisotropy power spectra, we also have information on the power spectrum of the gravitational lensing potential [89]. All of the likelihoods described above are already included in `Cobaya`.
In the following, we will denote with ***Planck*** the results obtained using temperature, polarisation and lensing measurements.

3.2.2 RSD measurements

As RSD reference measurements, we consider the data points in Tab. 1.2. These data are chosen following these three criteria [53]:

- when the data concern the same cosmological tracer, the considered $[f\sigma_8](z)$ data are obtained from uncorrelated redshift bins, while data are taken from possibly correlated redshift bins when different cosmological tracers were analysed;
- direct measurements of $f\sigma_8$ are taken into account;
- when the same survey collaboration performed two or more measurements corresponding to different data releases, the latest measurement of $f\sigma_8$ is considered.

For what regards the likelihood, we built our own as the data points used (i.e. the ones in Tab. 1.2) are not (all) included in `Cobaya` [33, 34], taking as example the one already implemented in the codes for BAO measurements. We built the covariance matrix as a diagonal matrix that has the square of the errors of the different points of Tab. 1.2 as diagonal elements. This matrix is taken to be diagonal because we assume that the different data points are all uncorrelated.
In the following, we will denote this dataset as ***RSD***.

3.2.3 Supernovae measurements

Type Ia Supernovae (SN Ia) serve as standardizable candles, that can be used to measure the expansion of the Universe. It was indeed thanks to these kind of measurements that we were able to discover the accelerating expansion of our Universe [90, 91]. Within the ΛCDM model, SN Ia have lower statistical power with respect to modern BAO measurements, but are still useful to gain some more informations on dark energy.

We consider, as SN Ia dataset, the Pantheon+ compilation [92]. It consists of 1550 spectroscopically confirmed SN Ia in the redshift range $0.001 < z < 2.26$. The total number of Supernovae, compiled across 18 different surveys, is significantly increased with respect to the first Pantheon analysis (1048 SN), particularly at low redshifts [44]. We use the public likelihood [93], included in `Cobaya`.

In the following, we will denote this dataset as ***PantheonPlus***, instead of using Pantheon+, to avoid confusion with the + sign used to express the considered measurements combinations.

3.2.4 DESI measurements

DESI spectroscopic targets are selected from photometric catalogs of the 9th public data release of the DESI Legacy Imaging Surveys. The five tracer samples, covering a total redshift range from $z = 0.1$ to $z = 4.2$, are the following ones [94]:

- the Bright Galaxy Samples (BGS) [95], in the range $0.1 < z < 0.4$, containing 854 targets per square degree. The final BGS clustering sample used for the BAO measurement comprises 300,017 redshifts in $0.1 < z < 0.4$;
- the Luminous Red Galaxy Sample (LRG) [96], in the range $0.4 < z < 0.6$ and $0.6 < z < 0.8$. The DESI DR1 LRG clustering sample used for BAO measurements consists of 2,138,600 redshifts in the interval $0.4 < z < 1.1$. The lower redshift bound was chosen to separate the sample from BGS, as most low-redshift LRG targets are also BGS targets;
- the Emission Line Galaxy Sample (ELG) [97], in the range $1.1 < z < 1.6$. The DR1 ELG sample comprises 2,432,022 reliable redshifts in the interval $0.8 < z < 1.6$;
- the combined LRG and ELG Sample (LRG+ELG), in the range $0.8 < z < 1.1$. As reported in [98], the combined LRG+ELG BAO measurement is $\sim 10\%$ more precise, so it is used for the cosmological inference;
- the Quasar Sample (QSO) [99], in the range $0.8 < z < 2.1$. The DR1 QSO sample used for BAO measurements consists of 856,652 redshifts;
- the Lyman-α Forest Sample (Lyα) [100], in the range $1.77 < z < 4.16$. This represent the highest-redshift BAO measurement from DESI DR1 and is obtained from a combined analysis of correlations of three different datasets.

In the following, we will denote this dataset as ***DESI***.

3.2.5 Cosmological inference

As a Boltzmann solver to interface with the cosmological inference code that we chose to use, i.e. `Cobaya` [33, 34], we decided to use a suitable modified version of the Cosmic Linear Anisotropy Solving System code, `CLASS` [31, 32].

All Bayesian inference is performed using the Metropolis-Hastings MCMC sampler [101, 102], developed for `CosmoMC` [101] and implemented in `Cobaya` [33, 34]. To test the convergence of the chains obtained using this approach, we utilize the Gelman-Rubin criterion [86], and we establish a threshold for chain convergence of $R-1 \lesssim 0.01$.

The figures shown in this chapter are obtained using `getdist` [103] (only the plot shown in Fig. 3.1 is obtained with a Python code).

We sample in the set of parameters of the ΛCDM model plus the coupling ξ, i.e. $\{w_{\rm b}, w_{\rm dm}, 100\theta_{\rm s}, \ln(10^{10}A_{\rm s}), n_{\rm s}, \tau, \xi\}$, where $w_{b(dm)} = \Omega_{\rm c(b)}h^2$ is the baryon (cold dark matter) energy density, $\theta_{\rm s}$ is the angular size of the horizon at the last scattering surface, τ is the optical depth, $\log(10^{10}A_{\rm s})$ is the amplitude of primordial scalar perturbation and $n_{\rm s}$ is the scalar spectral index.

The combinations of the previously described datasets considered are:

- ***Planck***;
- ***Planck*** + ***RSD***;
- ***Planck*** + ***DESI***;
- ***Planck*** + ***DESI*** + ***RSD***;
- ***Planck*** + ***DESI*** + ***PantheonPlus*** ;
- ***Planck*** + ***DESI*** + ***PantheonPlus*** + ***RSD***;

3.3 Results

Up to now we have presented the constraints on $\Omega_{\rm dm}h^2$ and ξ using the Python wrapper of `CLASS`, `Classy` (see Fig. 2.9) obtained considering the RSD measurements reported in Tab. 1.2.

To check for consistency between the different codes, our first result from `Cobaya` was aimed to reproduce the very same plot.

In order to obtain it, we fixed all the cosmological parameters to their best-fit values, except for $\Omega_{\rm dm}$ and ξ, that were being sampled by `Cobaya` [33, 34]. As a prior for the coupling, we considered a flat prior between -1 and 0 (this will be the case for all of the results obtained). In `Cobaya`, we use as a sampling parameter $\Omega_{\rm dm}h^2$ [5]. The prior chosen

---

[5] To obtain the values of $\Omega_{\rm dm}$, we multiplied the values of the output of `Cobaya` by the value of h in the *explanatory.ini* file of `CLASS`, i.e. $h = 0.67810$.

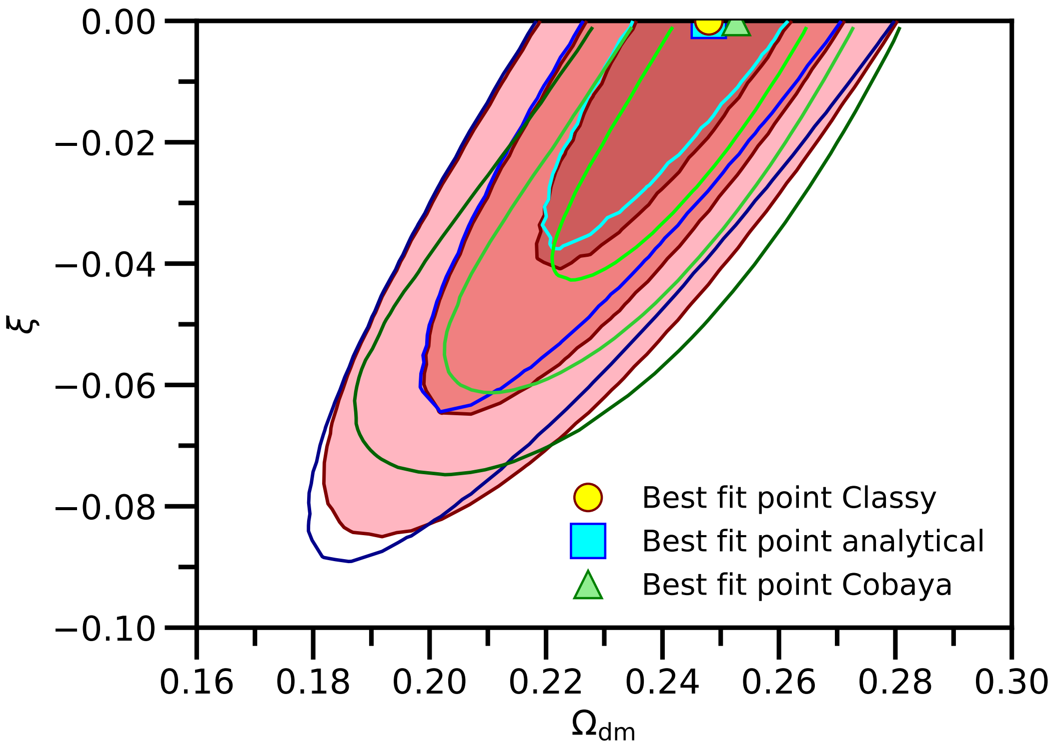

Figure 3.1: Contour plot in the ($\Omega_{\rm dm}$, ξ) plane from the χ^2 analysis for $[f\sigma_8](z)$ measurements. Regions from 1σ (darker color) to 3σ (lighter color) are shown. We show the contour plot obtained considering $f\sigma_8$ as the output of `CLASS` (colored shapes), the contour plot obtained considering f (from Eqs. (2.20) and (2.21)) and σ_8 as an output of `CLASS` (blue lines) and the contour plot obtained running `Cobaya` (green lines). We also show the three best fit points.

for $\Omega_{\rm dm}h^2$ is a flat prior between 0.001 and 0.99 (this will actually be true for all of the results obtained). Fig. 3.1 shows the results of the `Cobaya` analyses (green contours), compared to the contour plot obtained using `Classy` (red-colored shapes) and to the one obtained using our parametrisation for the growth factor f (blue contours) (see the caption of Fig. 2.9 for more details). The agreement between the three results is very good, as we notice that they all almost overlap.

In the following subsections, we shall present the constraints coming from different cosmological measurements. We shall denote with ΛCDM the results obtained using the standard, unmodified version of `CLASS`, while we shall denote with $\Lambda CDM + \xi$ the results obtained considering the studied IDE model and using our modified version of `CLASS`. In Appendix B one can find a table with the priors used for all the six (plus one) sampled parameters in the MCMC analyses in the ΛCDM (+ξ) case. Moreover, we considered the equation of state parameter for dark energy, w, to be $w = -1 + \epsilon$, with $\epsilon = 0.01$ (so $w = -0.99$) in order to regularise early-time super-horizon instabilities in the dynamics of cosmological perturbations [10, 15].

3.3.1 Planck results

In this subsection we present the results obtained considering ***Planck*** data. As a first check, we obtained the results considering the public version of `CLASS`, which should reproduce the ones presented in [1]. Then, we used our modified version of the codes to obtain the constraint on the IDE model considered. We shall comment on how the presence of the coupling ξ affects the best-fit values of the cosmological parameters within the ΛCDM model.

Planck in ΛCDM

Parameter	68% limits	68% limits from [1]
$\boldsymbol{\log(10^{10}A_\mathrm{s})}$	3.046 ± 0.014	3.044 ± 0.014
$\boldsymbol{n_\mathrm{s}}$	0.9644 ± 0.0041	0.9649 ± 0.0044
$\boldsymbol{100\theta_\mathrm{s}}$	1.04184 ± 0.00029	1.04090 ± 0.00031
$\boldsymbol{\Omega_\mathrm{b}h^2}$	0.02236 ± 0.00015	0.02237 ± 0.00015
$\boldsymbol{\Omega_\mathrm{dm}h^2}$	0.1200 ± 0.0012	0.1200 ± 0.0012
$\boldsymbol{\tau_\mathrm{reio}}$	0.0552 ± 0.0073	0.0544 ± 0.0073

Table 3.1: Table showing the 68% CL parameter intervals for the base-ΛCDM model from Planck CMB power spectra, in combination with CMB lensing reconstruction, using the public (unmodified) version of `CLASS`. All parameters are sampled in the MCMC analysis with flat priors. Left column: results arising from our simulation. Right column: constraints from Planck18 [1].

The results presented here, in Tab. 3.1 and in Fig. 3.2, are obtained considering the combination of TT, EE, TE and lensing spectra of Planck [1].
We see that all parameters are in excellent agreement with each other, except for a mildly shift in $100\theta_\mathrm{s}$, related to having considered different initial conditions in CLASS.

Planck in ΛCDM + ξ

The effect of the introduced coupling between dark matter and dark energy, as expected, has a significant influence mostly on the $\Omega_\mathrm{dm}h^2$ parameter. Indeed, as one can see from Fig. 3.3, there is a strong degeneracy between $\Omega_\mathrm{dm}h^2$ and ξ, with lower values of $\Omega_\mathrm{dm}h^2$ being permissible (with respect to the ΛCDM results) for more negative values of the coupling ξ. As a consequence, from Tab. 3.2, we can notice that the best-fit value for $\Omega_\mathrm{dm}h^2$ is significantly lower with respect to the ΛCDM value. All the other parameters, instead, appear to be less sensitive to the introduced coupling between dark energy and

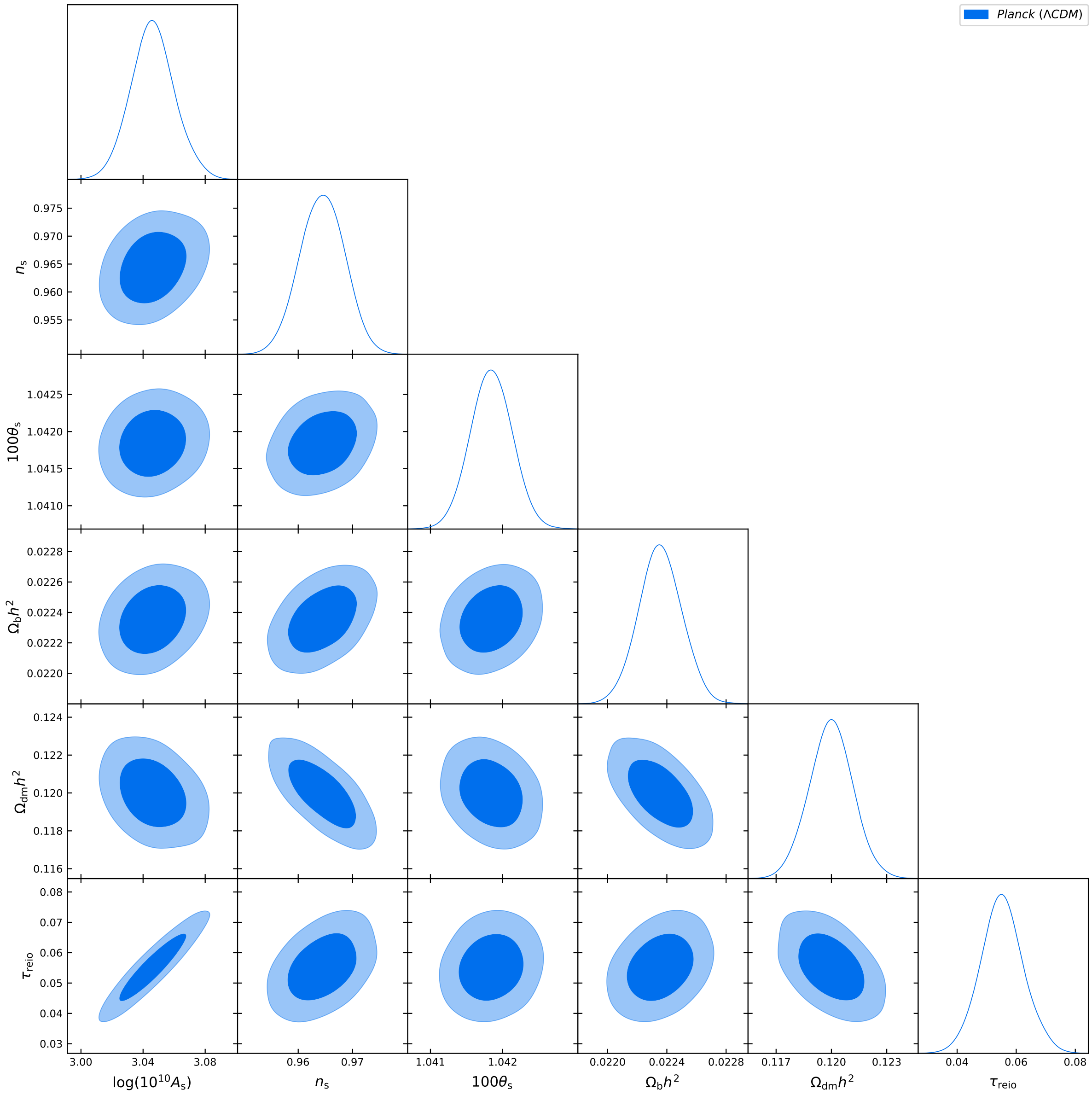

Figure 3.2: 68% and 95% CL constraints on the parameters of the base-ΛCDM model using the combination of TT, EE, TE and lensing spectra of Planck.

dark matter, as the obtained results are consistent with those obtained in the ΛCDM case (see Fig. 3.3). These results are consistent with the fact that Planck is not sensitive to very late time physics and the coupling between dark matter and dark energy changes the cosmological observables mainly at very low redshifts.

Parameter	68% limits
$\boldsymbol{\log(10^{10} A_\mathrm{s})}$	3.044 ± 0.014
$\boldsymbol{n_\mathrm{s}}$	0.9657 ± 0.0042
$\boldsymbol{100\theta_\mathrm{s}}$	1.04190 ± 0.00030
$\boldsymbol{\Omega_\mathrm{b} h^2}$	0.02238 ± 0.00015
$\boldsymbol{\Omega_\mathrm{dm} h^2}$	$0.066^{+0.052}_{-0.023}$
$\boldsymbol{\tau_\mathrm{reio}}$	0.0541 ± 0.0075
$\boldsymbol{\xi}$	> -0.565

Table 3.2: 68% CL intervals for the IDE model considered from Planck CMB power spectra, in combination with CMB lensing reconstruction, using our modified version of `CLASS`. We add the coupling ξ as an additional parameter. All parameters are sampled in the MCMC analysis with flat priors.

3.3.2 Planck + RSD results

In this subsection we present the results obtained considering ***Planck*** and ***RSD*** data. To compare how the coupling affects the parameters, we obtained the results considering the public version of `CLASS`, so in the standard cosmological model. Then, we used our modified version of the codes to obtain the constraint on the IDE model considered. We comment on how the presence of the coupling ξ affects the best-fit values of the ΛCDM model. To use the redshift space distortion measurements, we built our own likelihood since the likelihood for the measurements presented in Tab. 1.2 are not present in the available version of `Cobaya`.

Planck + RSD in ΛCDM

Parameter	68% limits
$\boldsymbol{\log(10^{10} A_\mathrm{s})}$	3.043 ± 0.014
$\boldsymbol{n_\mathrm{s}}$	0.9646 ± 0.0041
$\boldsymbol{100\theta_\mathrm{s}}$	1.04186 ± 0.00029
$\boldsymbol{\Omega_\mathrm{b} h^2}$	0.02237 ± 0.00015
$\boldsymbol{\Omega_\mathrm{dm} h^2}$	0.1198 ± 0.0012
$\boldsymbol{\tau_\mathrm{reio}}$	0.0538 ± 0.0073

Table 3.3: Table showing the 68% CL parameter intervals for the base-ΛCDM model from Planck CMB power spectra, in combination with CMB lensing reconstruction and redshift space distortions measurements, using the public (unmodified) version of `CLASS`. All parameters are sampled in the MCMC analysis with flat priors.

The results of this analysis can be found in Tab. 3.3 and in Fig. 3.4. We see that the results are perfectly in agreement with the results obtained considering Planck data

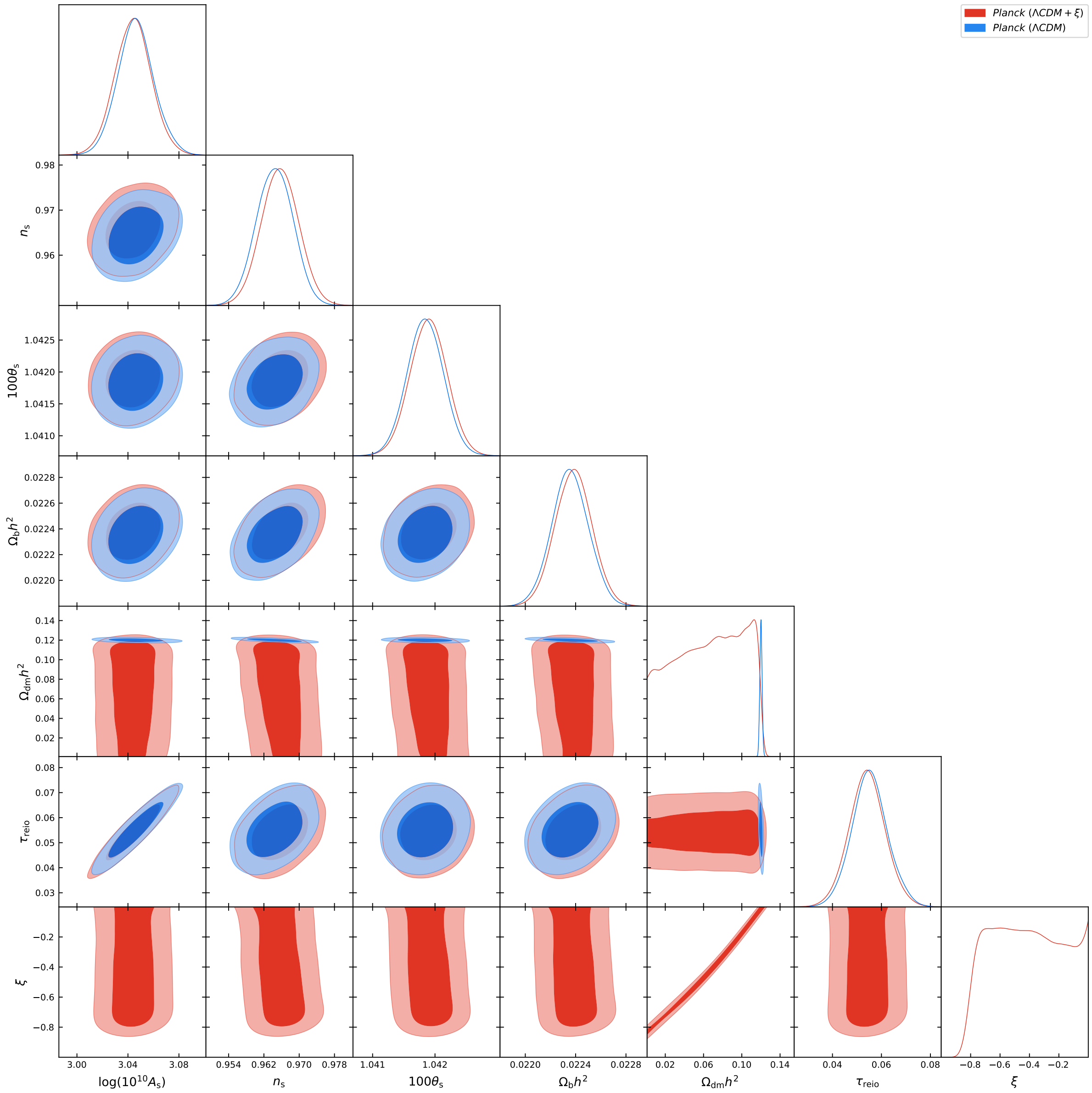

Figure 3.3: 68% and 95% CL constraints on the parameters of our IDE model using the combination of TT, EE, TE and lensing spectra of Planck. We show how the results for our model (red regions) compared to those obtained in the ΛCDM case (blue regions, see Fig. 3.2).

only. While RSD measurements provide important information about the growth of structure in the Universe, their constraints, in the minimal ΛCDM scenario, are less tight compared to the Planck CMB constraints. As a result, the MCMC analysis reflects the Planck results, with only minor adjustments from the RSD data.

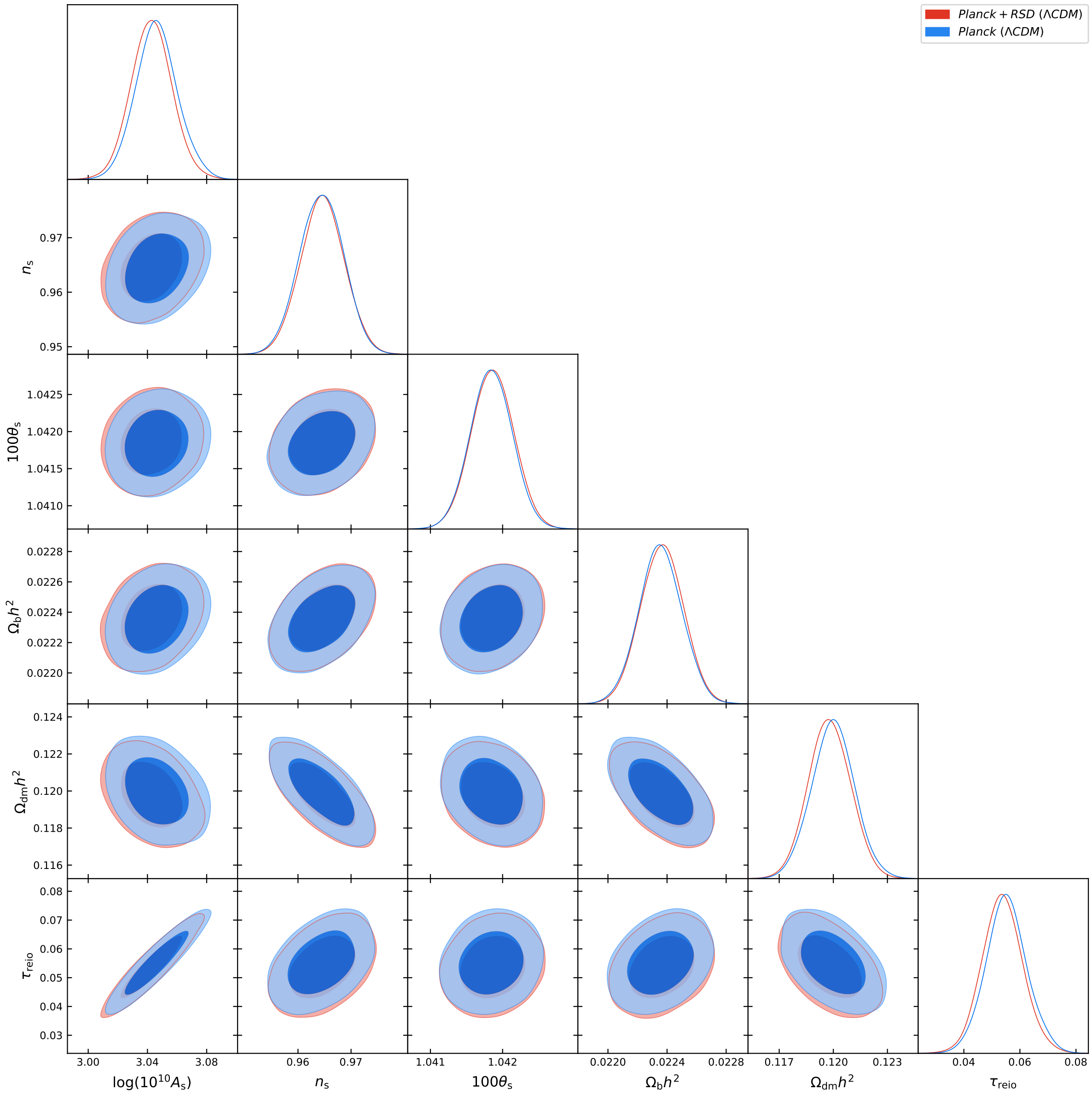

Figure 3.4: 68% and 95% CL constraints on the parameters of the base-ΛCDM model using the combination of TT, EE, TE and lensing spectra of Planck, together with redshift space distortions measurements. We show how the results of this combination of data (red regions) compare to those obtained for Planck alone (blue regions, see Fig. 3.2).

Planck + RSD in ΛCDM + ξ

Also in this case, the only parameter affected by the presence of the coupling is $\Omega_{dm}h^2$. Differently from the results obtained considering Planck alone, we see that the redshift

Parameter	68% limits
$\boldsymbol{\log(10^{10}A_\mathrm{s})}$	$3.043^{+0.015}_{-0.013}$
$\boldsymbol{n_\mathrm{s}}$	0.9654 ± 0.0041
$\boldsymbol{100\theta_\mathrm{s}}$	1.04188 ± 0.00029
$\boldsymbol{\Omega_\mathrm{b}h^2}$	0.02239 ± 0.00015
$\boldsymbol{\Omega_\mathrm{dm}h^2}$	$0.1184^{+0.0017}_{-0.0014}$
$\boldsymbol{\tau_\mathrm{reio}}$	0.0539 ± 0.0072
$\boldsymbol{\xi}$	> -0.0134

Table 3.4: Table showing the 68% CL parameter intervals for the IDE model considered from Planck CMB power spectra, in combination with CMB lensing reconstruction and redshift space distortions measurements, using our modified version of `CLASS`. We add the coupling ξ as an additional parameter to be constrained. All parameters are sampled in the MCMC analysis with flat priors.

space distortion measurements are more constraining (from Fig. 3.5 we see a smaller degeneracy with respect to Planck alone). Indeed, we find that the best-fit value of $\Omega_\mathrm{dm}h^2$ (see Tab. 3.4), is consistent with the result obtained in the standard cosmological model using Planck data only.
These results are consistent with the fact that RSD measurements reflect the late time physics of the Universe, i.e. when the coupling ξ should become more important. RSD measurements help to break the degeneracy between ξ and $\Omega_\mathrm{dm}h^2$, placing a tighter constraint on the coupling ξ. When Planck data is combined with RSD measurements, the constraints mainly improve on the parameters related to the growth rate of structure.

3.3.3 Planck + DESI results

In this subsection we present the results obtained considering ***Planck*** and ***DESI*** data. To compare how the coupling affects the parameters, we obtain the results considering the public version of `CLASS`, i.e. in the standard cosmological model. Then, we use our modified version of the codes to obtain the constraint on the IDE model considered. We comment on how the presence of the coupling ξ affects the best-fit values of the ΛCDM model.

Planck + DESI in ΛCDM

Comparing the results presented in Tab. 3.1 to those in Tab. 3.5, we notice that the combination of Planck + DESI shifts all the parameters values. In particular, we notice that the combination of Planck and DESI seems to prefer slightly lower values for $\Omega_\mathrm{dm}h^2$ with respect to Planck alone. Nevertheless, the results obtained considering both Planck and DESI are compatible at 1σ level with those obtained considering Planck alone.

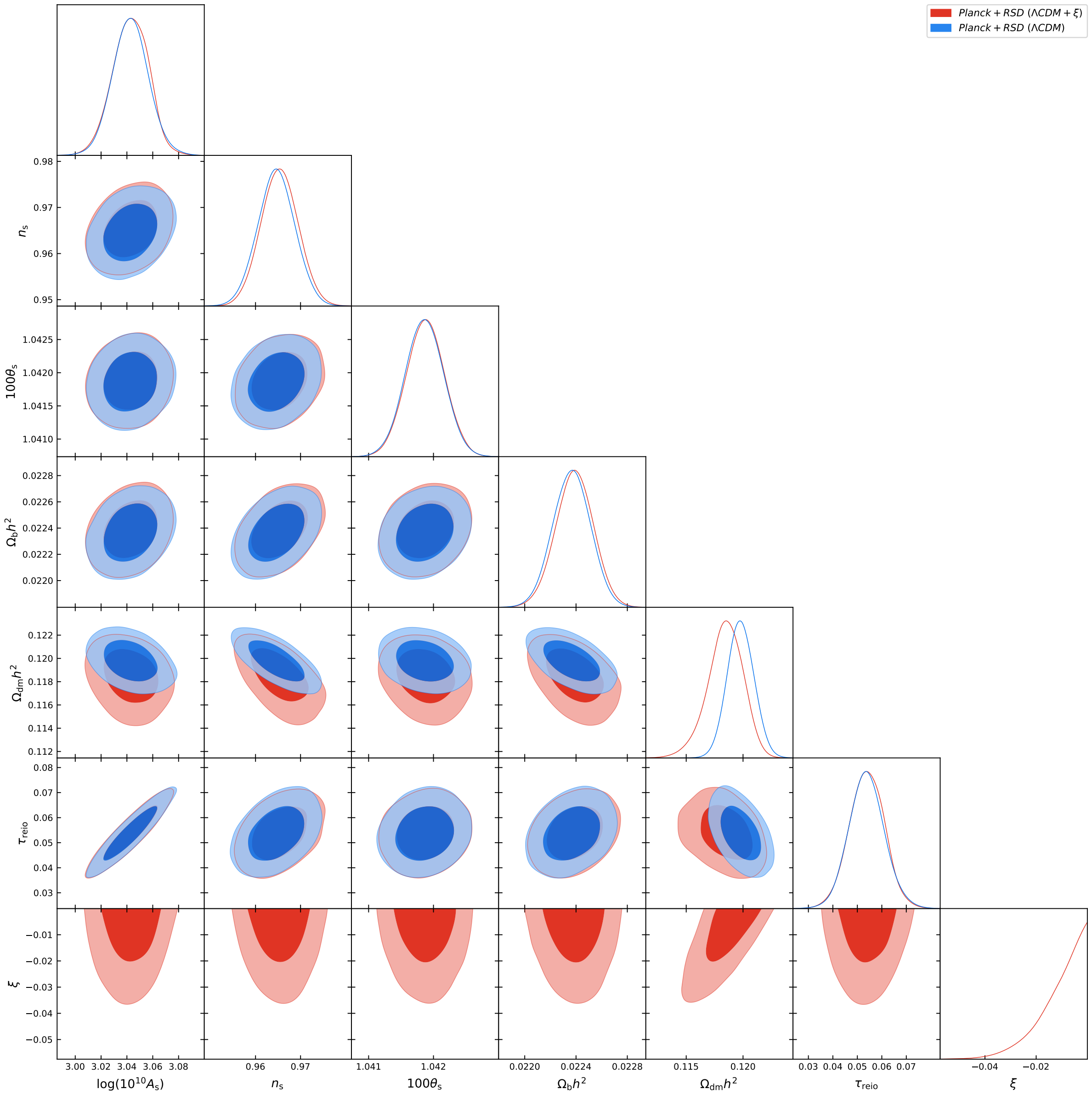

Figure 3.5: 68% and 95% CL constraints on the parameters of our IDE model using the combination of TT, EE, TE and lensing spectra of Planck, together with redshift space distortions measurements. We show how the results of our model (red regions) compare to those obtained in the ΛCDM case (blue regions, see Fig. 3.4).

Considering that we are dealing with the first DESI analysis of the cosmological data, one would need to wait for future data releases from DESI to better understand their results.

Parameter	68% limits
$\boldsymbol{\log(10^{10}A_\mathrm{s})}$	$3.051^{+0.013}_{-0.015}$
$\boldsymbol{n_\mathrm{s}}$	0.9686 ± 0.0037
$\boldsymbol{100\theta_\mathrm{s}}$	1.04203 ± 0.00028
$\boldsymbol{\Omega_\mathrm{b}h^2}$	0.02248 ± 0.00013
$\boldsymbol{\Omega_\mathrm{dm}h^2}$	0.11823 ± 0.00088
$\boldsymbol{\tau_\mathrm{reio}}$	$0.0594^{+0.0066}_{-0.0079}$

Table 3.5: Table showing the 68% CL parameter intervals for the base-ΛCDM model from Planck CMB power spectra, in combination with CMB lensing reconstruction and DESI BAO measurements, using the public (unmodified) version of `CLASS`. All parameters are sampled in the MCMC analysis with flat priors.

Planck + DESI in ΛCDM + ξ

Parameter	68% limits
$\boldsymbol{\log(10^{10}A_\mathrm{s})}$	3.048 ± 0.014
$\boldsymbol{n_\mathrm{s}}$	0.9674 ± 0.0037
$\boldsymbol{100\theta_\mathrm{s}}$	1.04198 ± 0.00028
$\boldsymbol{\Omega_\mathrm{b}h^2}$	0.02244 ± 0.00014
$\boldsymbol{\Omega_\mathrm{dm}h^2}$	$0.086^{+0.029}_{-0.012}$
$\boldsymbol{\tau_\mathrm{reio}}$	0.0569 ± 0.0073
$\boldsymbol{\xi}$	$-0.268^{+0.26}_{-0.083}$

Table 3.6: Table showing the 68% CL parameter intervals for the IDE model considered from Planck CMB power spectra, in combination with CMB lensing reconstruction and BAO measurements from DESI, using our modified version of `CLASS`. We add the coupling ξ as an additional parameter to be constrained. All parameters are sampled in the MCMC analysis with flat priors.

As can be noticed from Fig. 3.7, the degeneracy between $\Omega_\mathrm{dm}h^2$ and ξ is the main effect of the coupling, as all other parameters perfectly reproduce the results obtained in the ΛCDM case. Interestingly, since both the redshift space distortion measurements and the DESI BAO measurements provide information on late time physics, we notice that the combination of Planck and DESI seems to prefer a more negative value of the coupling with respect to the case of Planck and RSD. This, as we shall see, is due to the slightly larger value of the Hubble constant preferred by DESI observations. Even though the best-fit for ξ differs from zero, the results are compatible at 95% C.L. with a vanishing value of the coupling. Therefore, there is no strong evidence for a non-zero coupling. One must keep in mind that, in order to fully understand this result, we should wait for future DESI data releases. Based on the results of DESI analysis reported in [94], they seem to

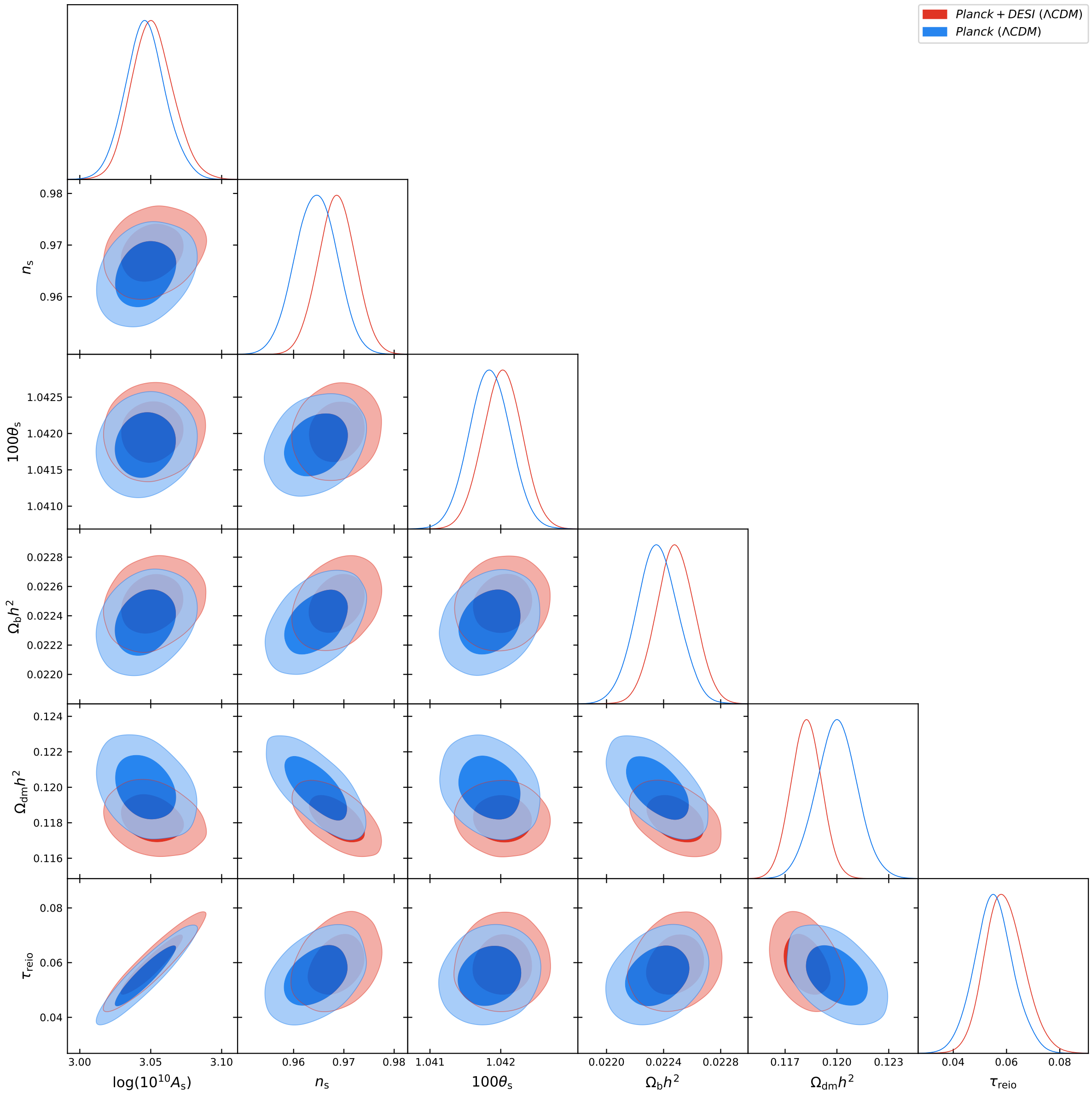

Figure 3.6: 68% and 95% CL constraints on the parameters of the base-ΛCDM model using the combination of TT, EE, TE and lensing spectra of Planck, together with BAO measurements from DESI. We show how the results of this combination of data (red regions) compare with those obtained for Planck alone (blue regions, see Fig. 3.2).

prefer a time-varying equation of state for dark energy. Our model could be re-conducted to this situation if we consider the fact that we can introduce an effective equation of state for dark energy, as shown in Eq. (2.5b). As we said for the base-ΛCDM case, we should need future data releases from the DESI collaboration to fully understand these

results.
Moreover, as one could expect, this analysis is more constraining than the case of Planck alone, reducing the lower bound on ξ.

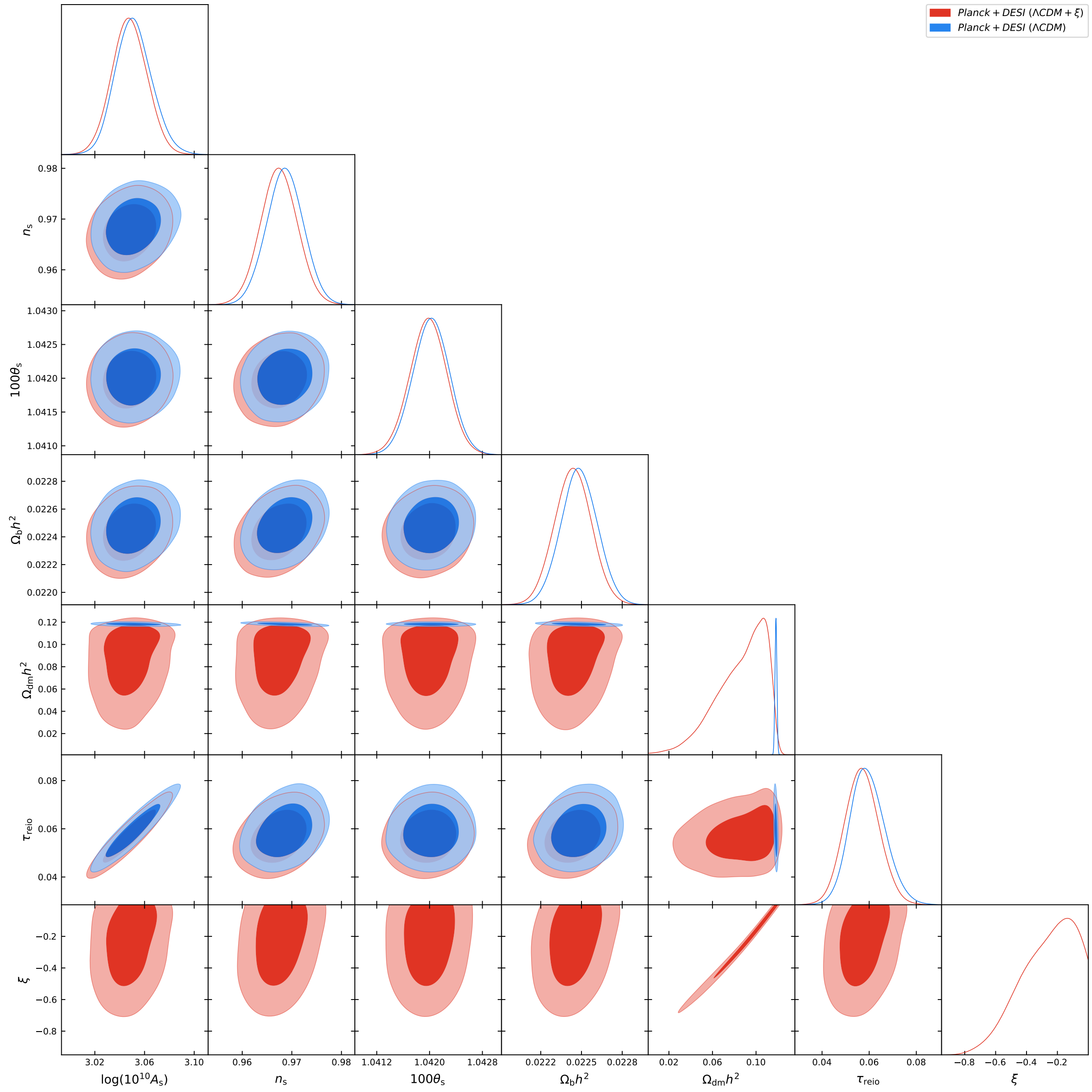

Figure 3.7: 68% and 95% CL constraints on the parameters of our IDE model using the combination of TT, EE, TE and lensing spectra of Planck, together with BAO measurements from DESI. We show how the results of our model (red regions) compare with those obtained in the ΛCDM case (blue regions, see Fig. 3.6).

3.3.4 Planck + DESI + RSD results

In this subsection we present the results obtained considering ***Planck***, ***DESI*** and ***RSD*** data. To compare how the coupling affects the parameters, we shall proceed as in the previous sections: we first obtain the results considering the publicly available version of `CLASS`, i.e. in the standard cosmological model. Then, we use our modified version of the codes to obtain the constraints on the IDE model considered. We comment on how the presence of the coupling ξ affects the best-fit values of the ΛCDM model. To use the ***RSD*** measurements, we built our own likelihood since not all of the data points in Tab. 1.2 are present in `Cobaya`.

Planck + DESI + RSD in ΛCDM

Parameter	68% limits
$\boldsymbol{\log(10^{10} A_\mathrm{s})}$	$3.050^{+0.013}_{-0.015}$
$\boldsymbol{n_\mathrm{s}}$	0.9688 ± 0.0037
$\boldsymbol{100\theta_\mathrm{s}}$	1.04203 ± 0.00028
$\boldsymbol{\Omega_\mathrm{b} h^2}$	0.02249 ± 0.00013
$\boldsymbol{\Omega_\mathrm{dm} h^2}$	0.11812 ± 0.00087
$\boldsymbol{\tau_\mathrm{reio}}$	$0.0589^{+0.0066}_{-0.0077}$

Table 3.7: Table showing the 68% CL parameter intervals for the base-ΛCDM model from Planck CMB power spectra, in combination with CMB lensing reconstruction, BAO measurements from DESI and redshift space distortions measurements, using the publicly available version of `CLASS`. All parameters are sampled in the MCMC analysis with flat priors.

Notice that, when combining both DESI and RSD measurements with the Planck ones, the results we obtain are dominated by Planck and DESI. Indeed, the shift in the best-fit values is still present, as found for Planck + DESI (see Figs. 3.8 and 3.6). Also, the best-fit values presented in Tab. 3.7 are closer to the ones presented in Tab. 3.5, with respect to those in Tab. 3.3.

When adding RSD to the Planck+DESI combination, the overall improvement in the constraints is not significant. This is because DESI already provides comprehensive information on the large-scale structure, including aspects that overlap with what RSD measures. Therefore, DESI data dominates the RSD one, which simply provide small differences to the results obtained considering Planck+DESI alone.

Planck + DESI + RSD in ΛCDM + ξ

When including the coupling, we notice instead that the RSD measurements appear to have a much stronger effect on ξ, thanks to the fact that they directly measure the impact

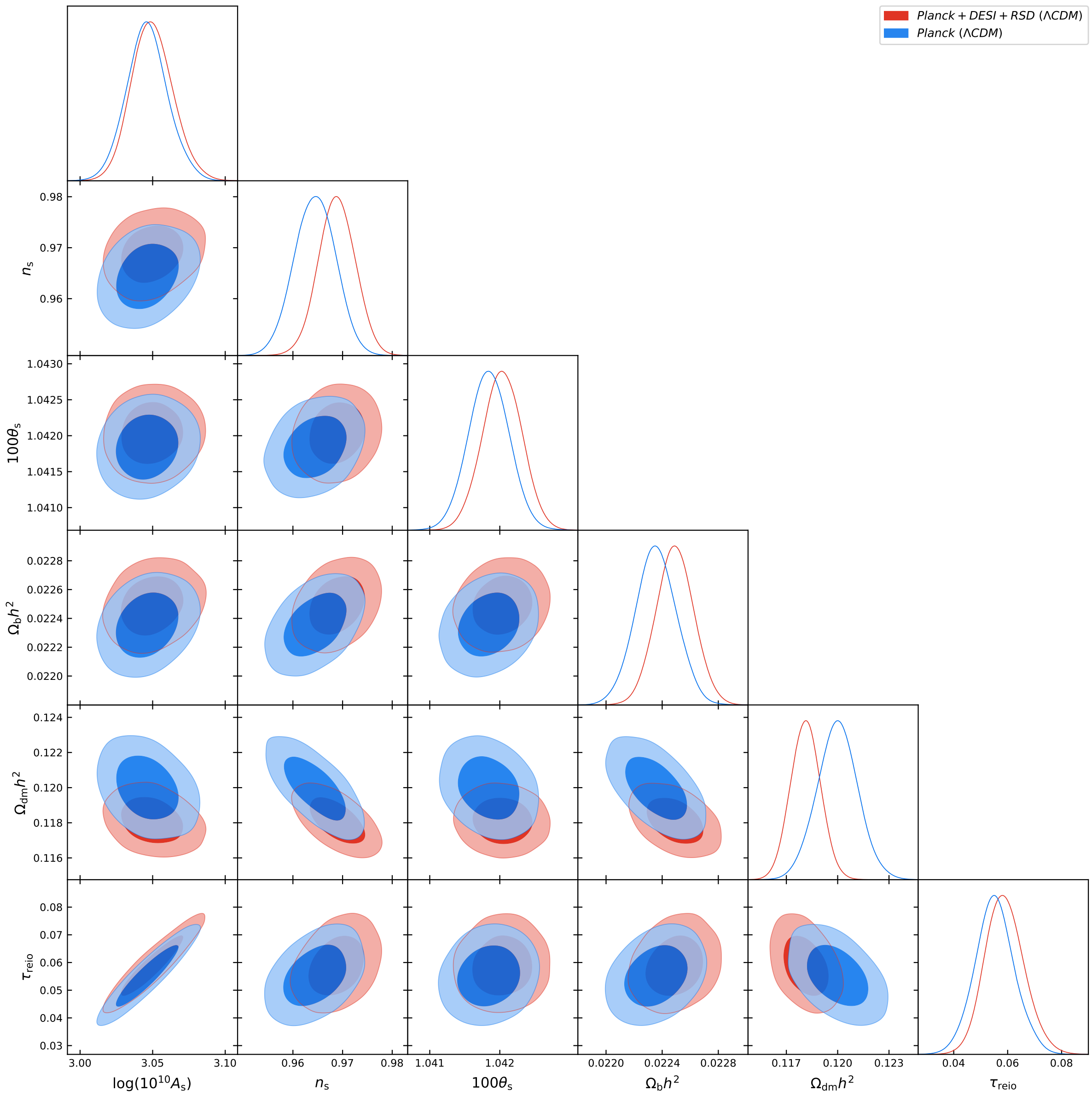

Figure 3.8: 68% and 95% CL constraints on the parameters of the base-ΛCDM model using the combination of TT, EE, TE and lensing spectra of Planck, together with BAO measurements from DESI and redshift space distortions measurements. We show how the results of this combination of data (red regions) compare with those obtained for Planck alone (blue regions, see Fig. 3.2).

of the interaction rate on the growth of structures. Indeed, we notice (see Tab. 3.8) that the constraint on ξ is less strong than the one obtained considering Planck+RSD, but stronger than the one obtained considering Planck+DESI. Therefore, adding RSD

Parameter	68% limits
$\boldsymbol{\log(10^{10}A_s)}$	$3.050^{+0.013}_{-0.015}$
$\boldsymbol{n_s}$	0.9692 ± 0.0036
$\boldsymbol{100\theta_s}$	1.04204 ± 0.00028
$\boldsymbol{\Omega_b h^2}$	0.02251 ± 0.00013
$\boldsymbol{\Omega_{dm} h^2}$	$0.1167^{+0.0016}_{-0.0011}$
$\boldsymbol{\tau_{reio}}$	$0.0589^{+0.0065}_{-0.0079}$
$\boldsymbol{\xi}$	> -0.0155

Table 3.8: Table showing the 68% CL parameter intervals for the IDE model considered from Planck CMB power spectra, in combination with CMB lensing reconstruction, BAO measurements from DESI and redshift space distortions measurements, using our modified version of `CLASS`. We add the coupling ξ as an additional parameter to be constrained. All parameters are sampled in the MCMC analysis with flat priors.

to Planck+DESI changes the parameter constraints more significantly than within the ΛCDM model. Once again, the only parameter on which the coupling has a noticeable impact is on $\Omega_{\rm dm}h^2$. In Fig. 3.9, we can still see the degeneracy with the coupling ξ, favouring lower values of $\Omega_{\rm dm}h^2$. However, RSD data imposes a tighter lower bound on ξ, making the value of the $\Omega_{\rm dm}h^2$ parameter closer to its (and Planck) ΛCDM result.

3.3.5 Planck + DESI + PantheonPlus results

In this subsection we present the results obtained considering ***Planck***, ***DESI*** and ***PantheonPlus*** data. To explore how the coupling affects the parameters, we obtain the results considering the public version of `CLASS`, i.e. in the standard cosmological model. Then, we use our modified version of the codes to obtain the constraints on the IDE model considered, commenting on how the presence of the coupling ξ affects the best-fit values of the ΛCDM model.

Planck + DESI + PantheonPlus in ΛCDM

The PantheonPlus dataset provides precise supernova data, which gives robust measurements of the expansion history of the Universe at late times. However, the constraining power of DESI dominates over the PantheonPlus one when considering the six standard parameters of the concordance cosmological model (ΛCDM) due to its comprehensive large-scale structure data and its ability to provide precise measurements of the matter power spectrum, BAO, and RSD. While PantheonPlus observations are important for constraining the Hubble constant and the late-time expansion history, DESI data are more powerful for the full set of ΛCDM parameters.

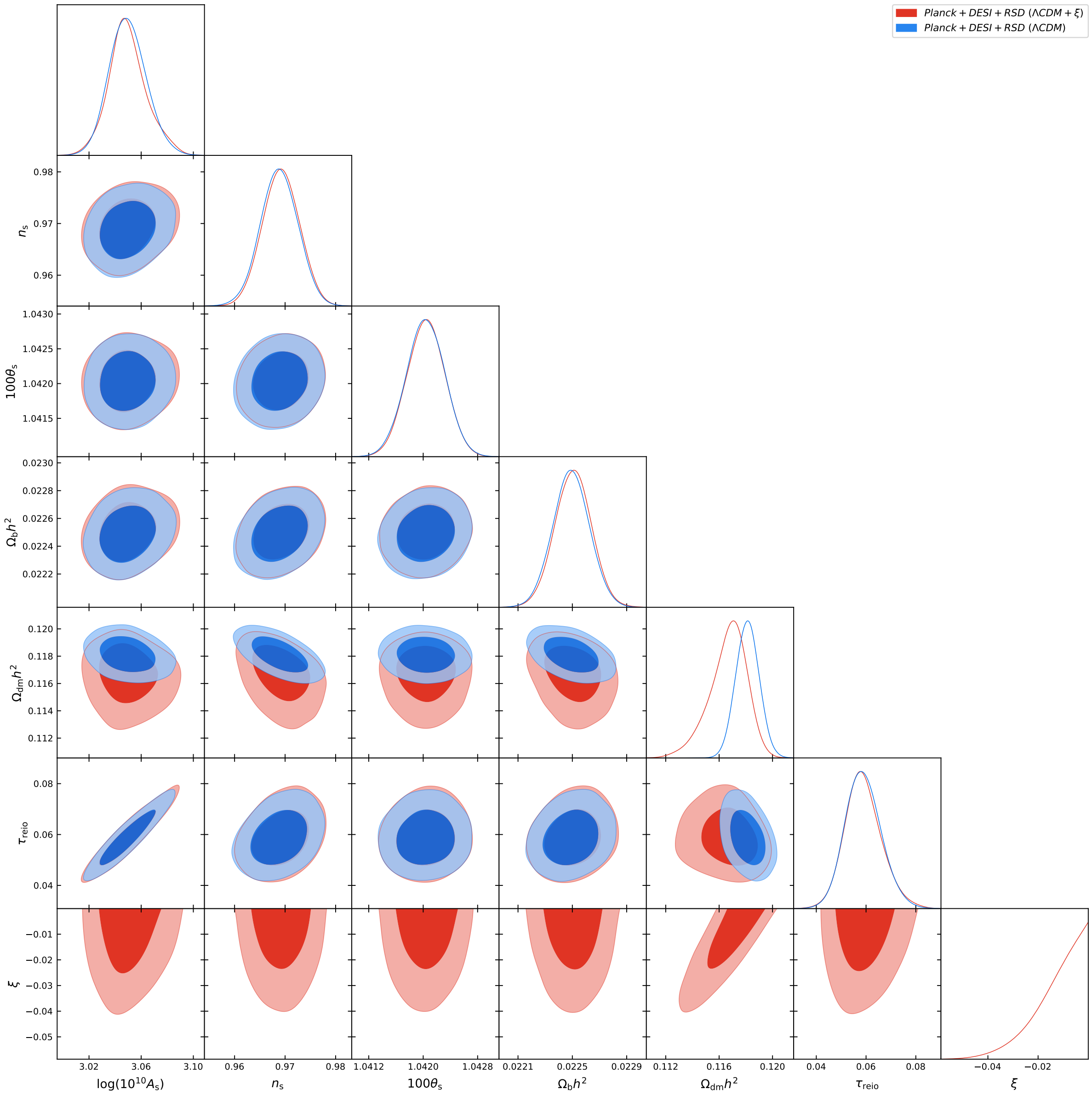

Figure 3.9: 68% and 95% CL constraints on the parameters of our IDE model using the combination of TT, EE, TE and lensing spectra of Planck, together with BAO measurements from DESI and redshift space distortions measurements. We show how the results of our model (red regions) compare with those obtained in the ΛCDM case (blue regions, see Fig. 3.8).

Planck + DESI + PantheonPlus in ΛCDM + ξ

Also for this data combination the effect of the coupling is reflected only in the degeneracy between $\Omega_{\rm dm}h^2$ and ξ. The presence of the Supernovae measurements makes the

Parameter	68% limits
$\boldsymbol{\log(10^{10}A_\mathrm{s})}$	3.050 ± 0.014
$\boldsymbol{n_\mathrm{s}}$	0.9681 ± 0.0036
$\boldsymbol{100\theta_\mathrm{s}}$	1.04201 ± 0.00028
$\boldsymbol{\Omega_\mathrm{b}h^2}$	0.02246 ± 0.00013
$\boldsymbol{\Omega_\mathrm{dm}h^2}$	0.11848 ± 0.00085
$\boldsymbol{\tau_\mathrm{reio}}$	$0.0588^{+0.0066}_{-0.0075}$

Table 3.9: Table showing the 68% CL parameter intervals for the base-ΛCDM model from Planck CMB power spectra, in combination with CMB lensing reconstruction, BAO measurements from DESI and Supernovae measurements from PanthoenPlus, using the public (unmodified) version of `CLASS`. All parameters are sampled in the MCMC analysis with flat priors.

Parameter	68% limits
$\boldsymbol{\log(10^{10}A_\mathrm{s})}$	$3.049^{+0.013}_{-0.015}$
$\boldsymbol{n_\mathrm{s}}$	0.9676 ± 0.0036
$\boldsymbol{100\theta_\mathrm{s}}$	1.04199 ± 0.00028
$\boldsymbol{\Omega_\mathrm{b}h^2}$	0.02245 ± 0.00013
$\boldsymbol{\Omega_\mathrm{dm}h^2}$	$0.1127^{+0.0056}_{-0.0022}$
$\boldsymbol{\tau_\mathrm{reio}}$	$0.0578^{+0.0066}_{-0.0074}$
$\boldsymbol{\xi}$	> -0.0686

Table 3.10: Table showing the 68% CL parameter intervals for the IDE model considered from Planck CMB power spectra, in combination with CMB lensing reconstruction, BAO measurements from DESI and Supernovae measurements from PanthoenPlus, using our modified version of `CLASS`. We add the coupling ξ as an additional parameter to be constrained. All parameters are sampled in the MCMC analysis with flat priors.

constraint on the coupling tighter with respect to the case of Planck and DESI. The reason is the same as for the RSD measurements, as also Supernovae data is very sensitive to late time physics, placing a more restrictive lower bound on the coupling ξ.

3.3.6 Planck + DESI + PantheonPlus + RSD results

In this subsection we present the results obtained considering ***Planck***, ***DESI***, ***PantheonPlus*** and ***RSD*** data. To compare how the coupling affects the parameters, we proceed as in the previous sections, obtaining first the results considering the public version of `CLASS`, e.g. in the standard cosmological model. Then, we use our modified version of the codes to obtain the constraints on the IDE model considered. We comment on how the presence of the coupling ξ affects the best-fit values of the ΛCDM model. To remind here that, in order to use the ***RSD*** measurements, we built our own likelihood

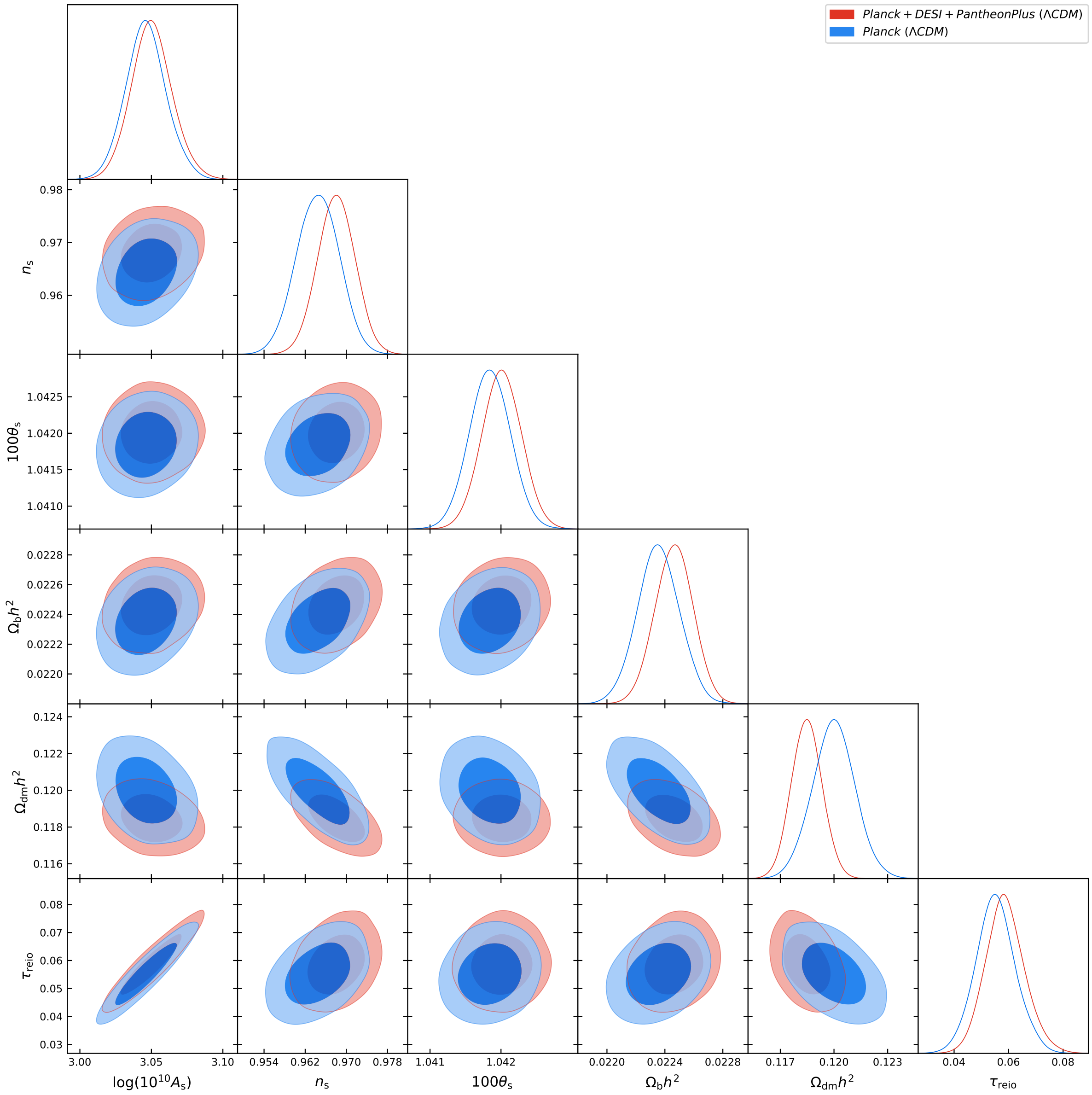

Figure 3.10: 68% and 95% CL constraints on the parameters of the base-ΛCDM model using the combination of TT, EE, TE and lensing spectra of Planck, together with BAO measurements from DESI and Supernovae measurements from PantheonPlus. We show how the results of this combination of data (red regions) compare with those obtained for Planck alone (blue regions, see Fig. 3.2).

since the data points were not present in `Cobaya`.

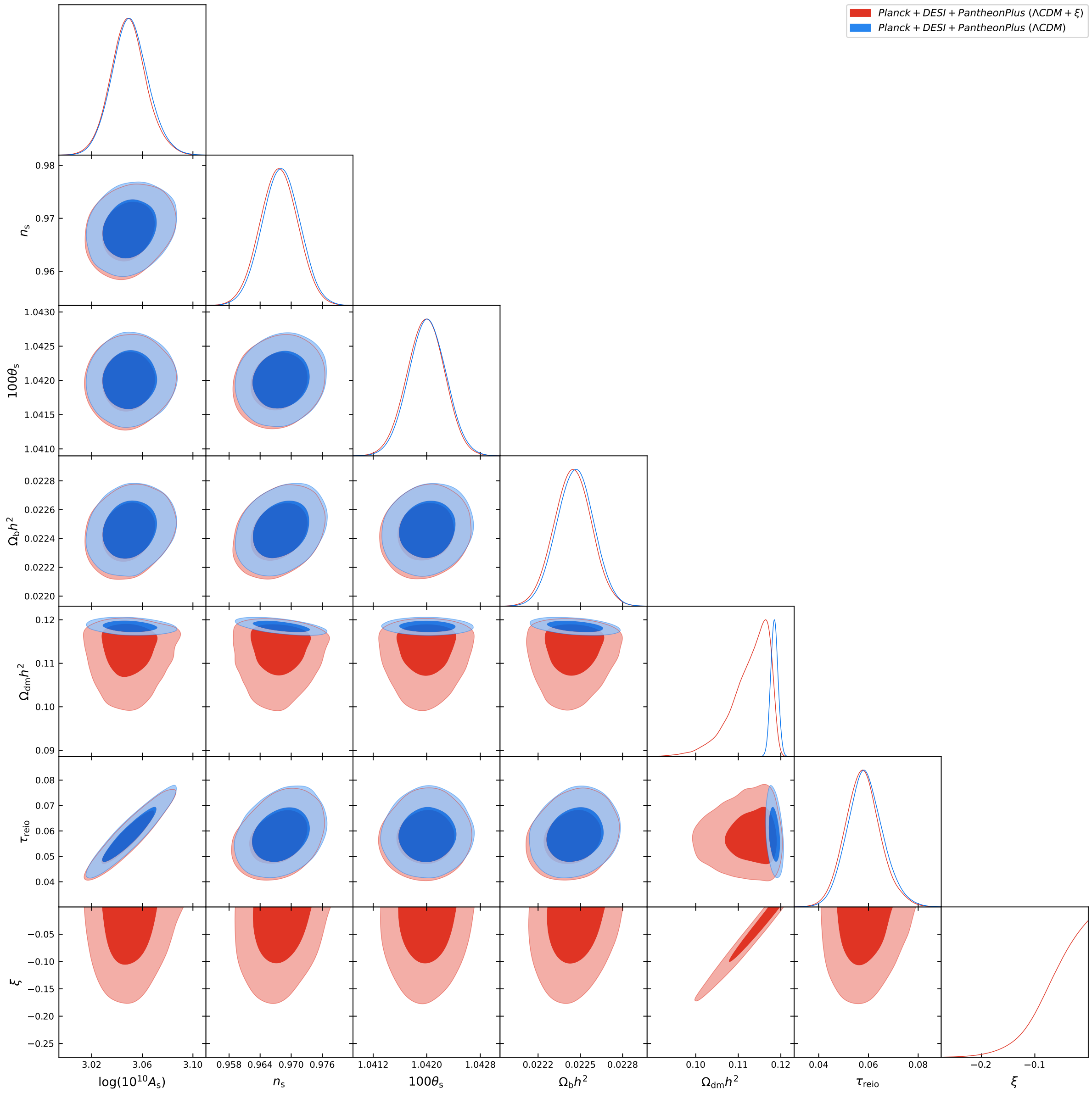

Figure 3.11: 68% and 95% CL constraints on the parameters of our IDE model using the combination of TT, EE, TE and lensing spectra of Planck, together with BAO measurements from DESI and Supernovae measurements from PantheonPlus. We show how the results of our model (red regions) compare to those obtained in the ΛCDM case (blue regions, see Fig. 3.10).

Planck + DESI + PantheonPlus + RSD in ΛCDM

Notice from Fig. 3.12 that even when we consider the three low redshift datasets, the dominating one is the DESI dataset. Nevertheless, the shifts in best-fit values (with

Parameter	68% limits
$\log(10^{10}A_\mathrm{s})$	3.049 ± 0.014
n_s	0.9681 ± 0.0036
$100\theta_\mathrm{s}$	1.04201 ± 0.00028
$\Omega_\mathrm{b}h^2$	0.02247 ± 0.00013
$\Omega_\mathrm{dm}h^2$	0.11839 ± 0.00084
τ_reio	$0.0582^{+0.0066}_{-0.0074}$

Table 3.11: Table showing the 68% Cl parameter intervals for the base-ΛCDM model from Planck CMB power spectra, in combination with CMB lensing reconstruction, BAO measurements from DESI, Supernovae measurements from PantheonPlus and redshift space distortions measurements, using the publicly available (unmodified) version of `CLASS`. All parameters are sampled in the MCMC analysis with flat priors.

respect to Planck alone) are smaller now because we have also two additional dataset that have an effect (even if small with respect to DESI) on the results that one would obtain considering Planck+DESI only.

Planck + DESI + PantheonPlus + RSD in ΛCDM + ξ

Parameter	68% limits
$\log(10^{10}A_\mathrm{s})$	3.047 ± 0.014
n_s	0.9684 ± 0.0036
$100\theta_\mathrm{s}$	1.04200 ± 0.00028
$\Omega_\mathrm{b}h^2$	0.02247 ± 0.00013
$\Omega_\mathrm{dm}h^2$	$0.1172^{+0.0014}_{-0.0010}$
τ_reio	0.0572 ± 0.0072
ξ	> -0.0136

Table 3.12: Table showing the 68% CL parameter intervals for the IDE model considered from Planck CMB power spectra, in combination with CMB lensing reconstruction, BAO measurements from DESI, Supernovae measurements from PantheonPlus and redshift space distortions measurements, using our modified version of `CLASS`. We add the coupling ξ as an additional parameter to be constrained. All parameters are sampled in the MCMC analysis with flat priors.

When considering all datasets together, we see that the constraints on the ΛCDM + ξ model become quite strong and the most constraining measurements are the RSD ones. Indeed, we notice that the degeneracy between $\Omega_\mathrm{dm}h^2$ and ξ is much smaller than in all the other cases in which the RSD measurements were not taken into account. All other parameters reproduce the ΛCDM results, with the particular DESI induced-shift.

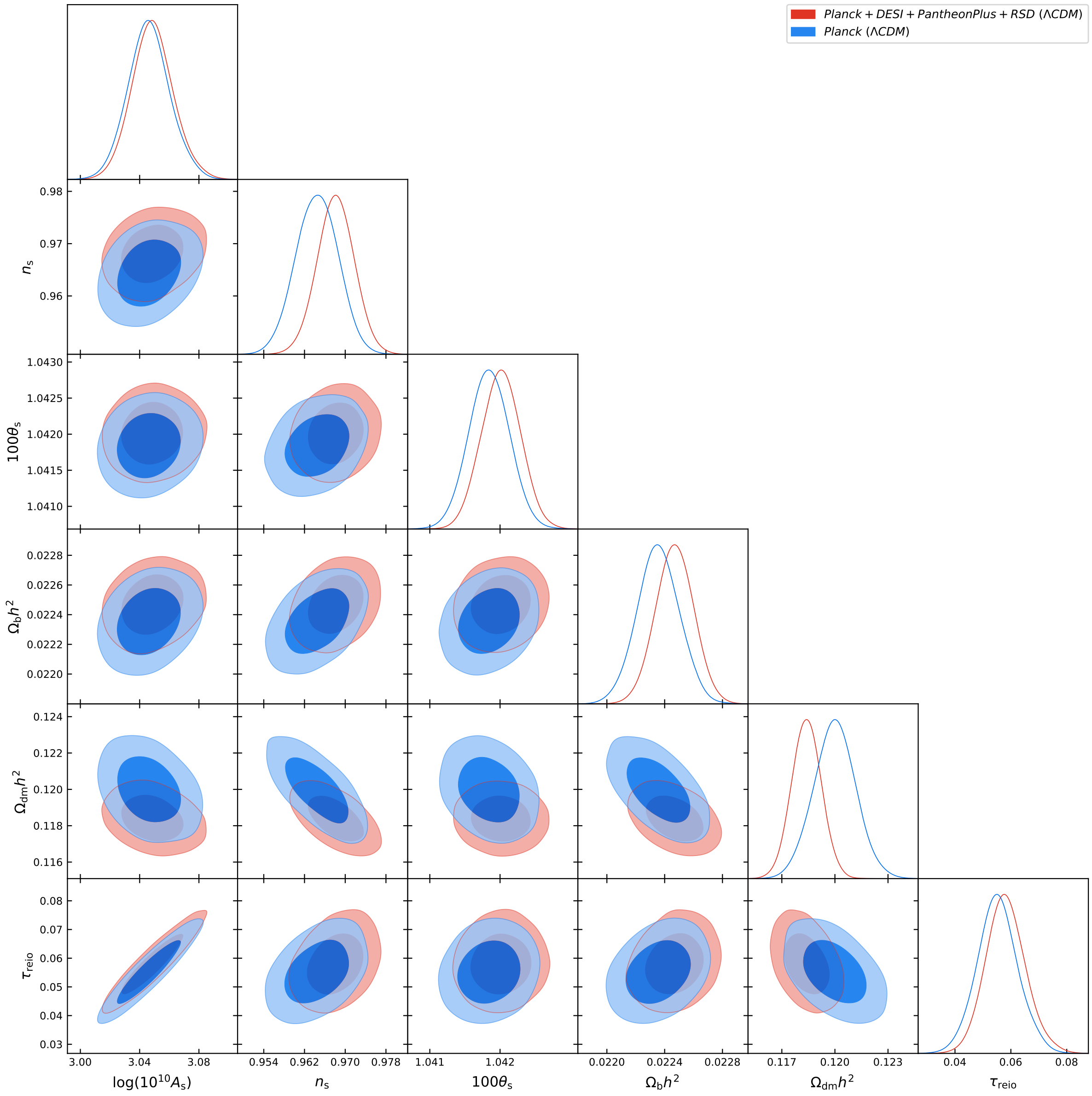

Figure 3.12: 68% and 95% CL constraints on the parameters of the base-ΛCDM model using the combination of TT, EE, TE and lensing spectra of Planck, together with BAO measurements from DESI, Supernovae measurements from PantheonPlus and redshift space distortions. We show how the results of this combination of data (red regions) compare with those obtained for Planck alone (blue regions, see Fig. 3.2).

Therefore, it is crucial to take RSD measurements into account when studying coupled cosmologies, since these data are the ones constraining the most the coupling ξ.

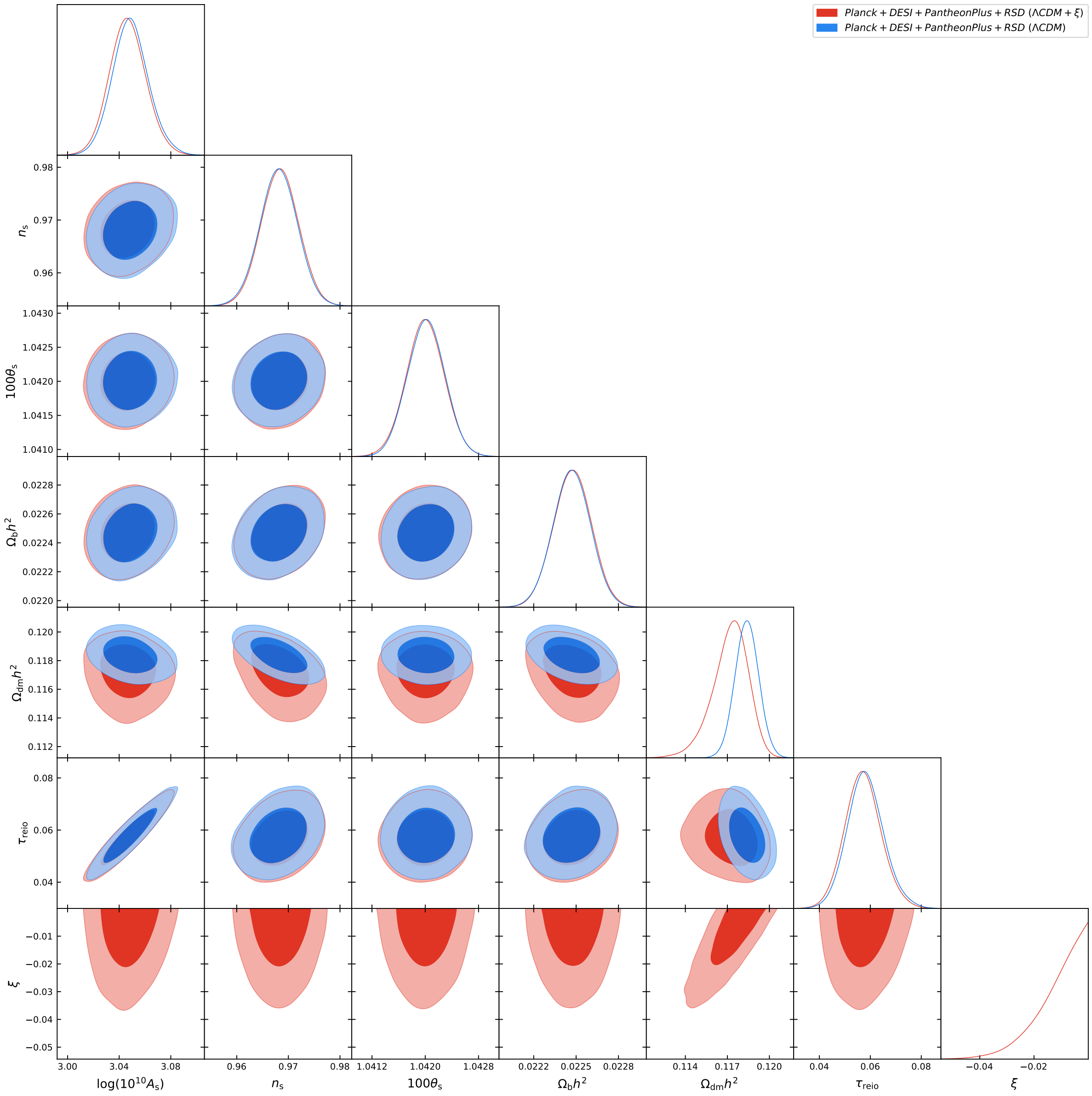

Figure 3.13: 68% and 95% CL constraints on parameters of our IDE model using the combination of TT, EE, TE and lensing spectra of Planck, together with BAO measurements from DESI, Supernovae measurements from PantheonPlus and redshift space distortions measurements. We show how the results of our model (red regions) compare with those obtained in the ΛCDM case (blue regions, see Fig. 3.12).

3.3.7 Impact of IDE models on cosmological parameters

We shall present in what follows the largest impact of IDE models on the cosmological parameters, focusing on the Hubble constant and on the dark matter mass energy density parameter, which is the most affected parameter (among the six) by the presence of the introduced coupling ξ.

The effect of the coupling on H_0

Figure 3.14 illustrates the strong degeneracy between the Hubble constant H_0 and the coupling ξ. Indeed, IDE models could be able to alleviate the so-called H_0 tension [104, 105, 106, 107, 108, 109, 110, 111, 112].
We notice that Planck alone allows higher values of H_0, consistent with the measurements of SH0ES. This is related to the very strong degeneracy that appears between $\Omega_{\rm dm}h^2$ and the coupling ξ (see Fig. 3.3), that is reflected by the degeneracy between H_0 and ξ. Also including DESI measurements, we notice that there is still a huge degeneracy, which reduces the H_0 tension as for more negative couplings, higher H_0 values are allowed. As soon as we consider also Supernovae and RSD measurements, the constraints becomes tighter. In particular, considering Fig. 3.14, we notice that the RSD measurements give a very tight constraint for the coupling, which translates into a value for the Hubble parameter today in agreement with the one we have from Planck.
Therefore, focusing on Planck and Planck+DESI measurements, interacting dark energy models could fully solve the H_0 tension. We notice that actually the addition of DESI data seems to prefer a non zero coupling, even though still compatible with a zero value for ξ. When one includes also SN measurements, we obtain lower values of H_0 with respect to the previous dataset combinations considered, but higher than those obtained with the CMB measurements of Planck in the ΛCDM scenario. This alleviates the H_0 tension as well, even if not significantly.
It is only when we introduce the RSD measurements that the constraints become extremely tight, favoring values of H_0 which are in agreement with the Planck ΛCDM results, not allowing to alleviate the tension. This is a neat important result, since the RSD measurements are the most sensitive to the effect of the coupling.

The effect of the coupling on $\Omega_{\rm dm}h^2$

In Fig. 3.15, we compare how the expected degeneracy between $\Omega_{\rm dm}h^2$ and ξ gets constrained by the different measurements. Here, the behaviour is the same as before. Since ξ and $\Omega_{\rm dm}h^2$ are strongly degenerate, a tighter constraint on the coupling ξ will lead to a tighter constraint in $\Omega_{\rm dm}h^2$.
We notice that with Planck data alone the degeneracy is very strong, which is consistent with the fact that CMB measurements are not sensitive to late times physics. Including DESI measurements, we notice that the degeneracy gets mildly reduced. As soon as we

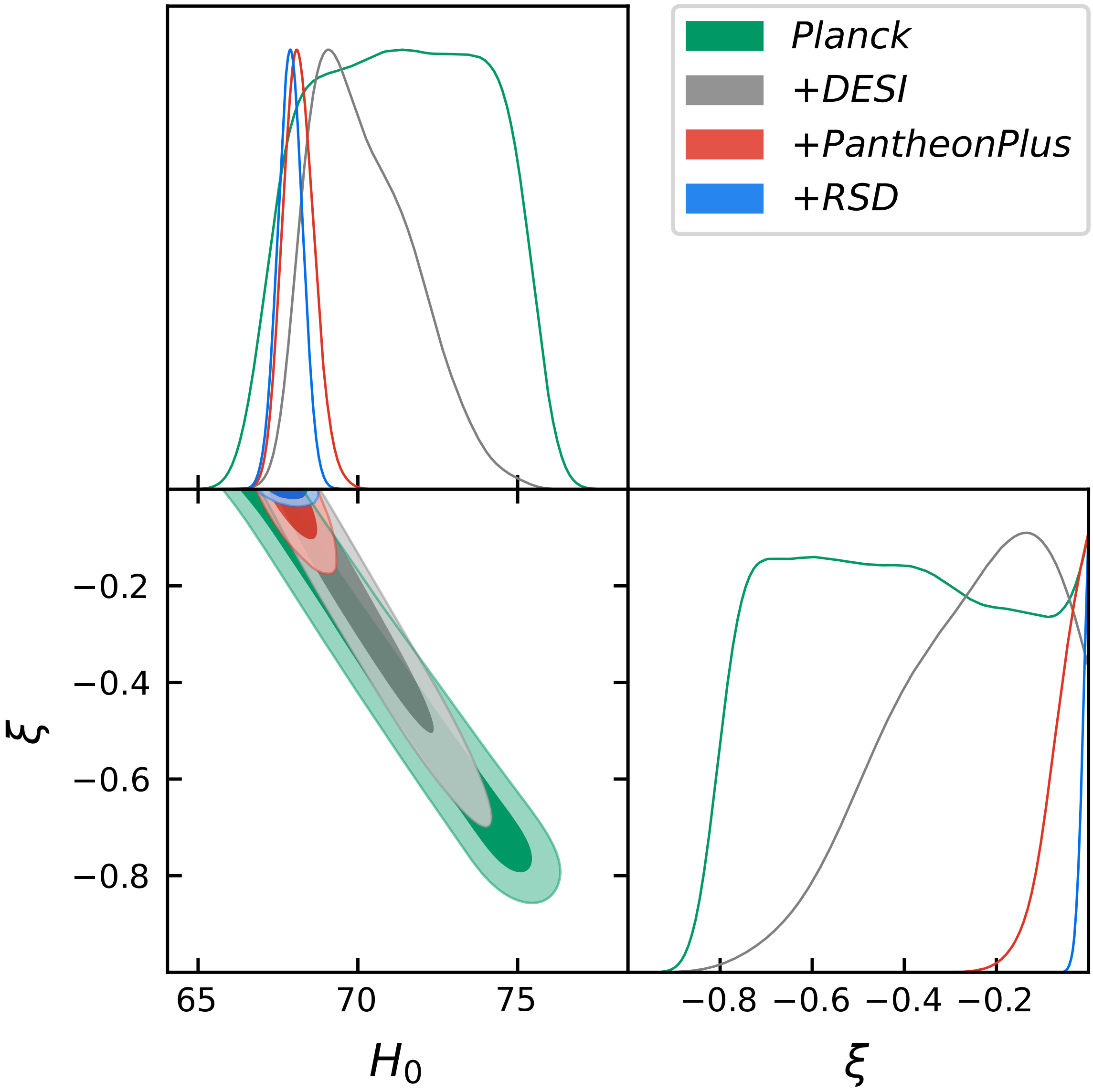

Figure 3.14: One-dimensional probability distributions and 68% and 95% CL joint constraints on ξ and H_0 for our IDE model using different combinations of measurements. The plus sign should be interpreted as an addition to all the data previously considered, meaning that each row contains all data from the above. All the results are obtained in the $\Lambda CDM + \xi$ scenario.

consider also Supernovae and RSD measurements, the constraints becomes tighter. In particular, considering Fig. 3.15, we notice that the RSD measurements give a very tight constraint for the coupling, which translates into a smaller degeneracy in the $(\Omega_{\rm dm}h^2, \xi)$ plane.

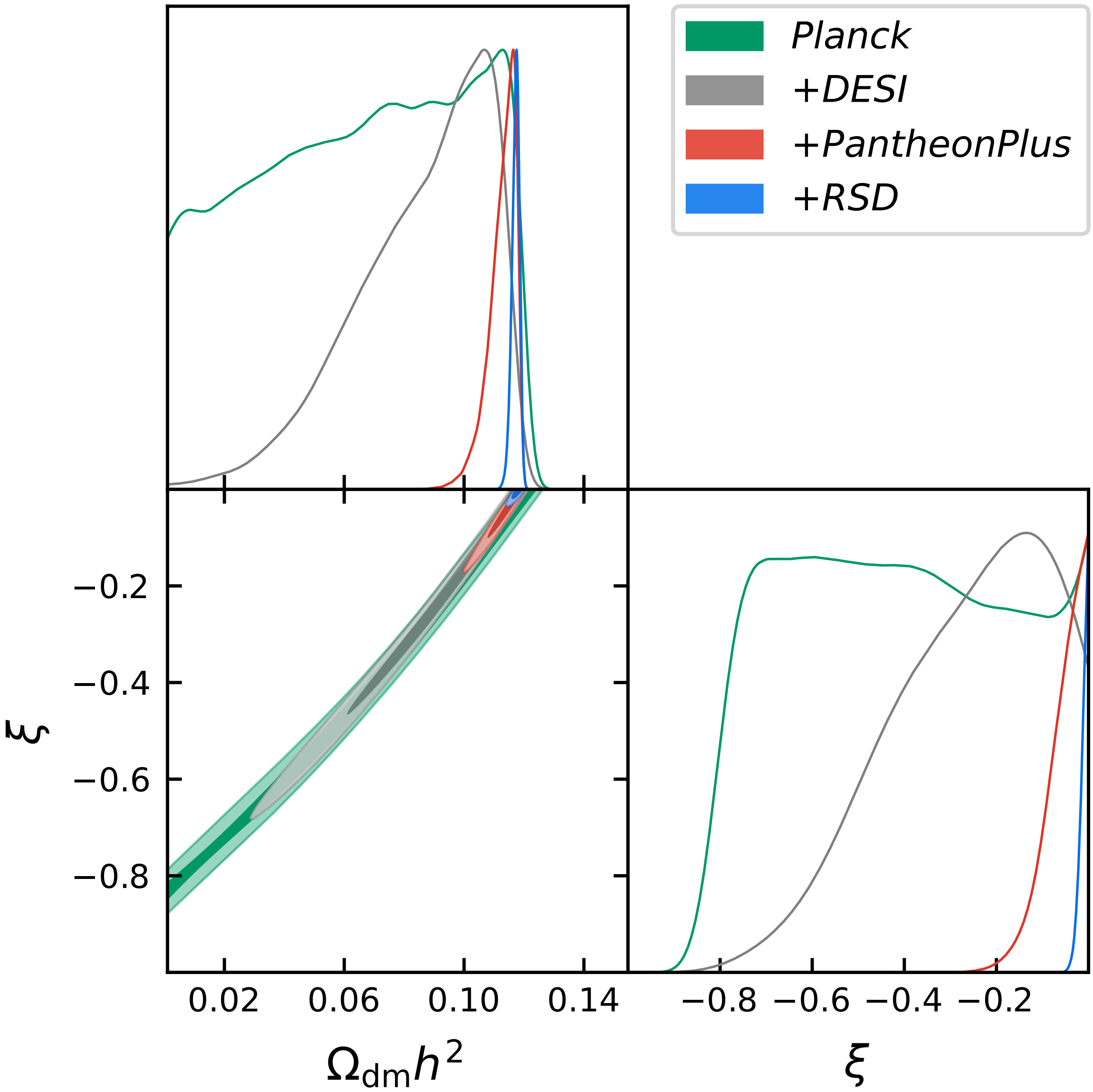

Figure 3.15: One-dimensional probability distributions and 68% and 95% CL joint constraints on ξ and $\Omega_{\mathrm{dm}}h^2$ for our IDE model using different combinations of measurements. The plus sign should be interpreted as an addition to all the data previously considered, meaning that each row contains all data from the above. All the results are obtained in the ΛCDM + ξ scenario.

Chapter 4

Conclusions

In this thesis, we have investigated the growth of structures in non-standard dark energy cosmologies, focusing on the interacting dark energy (IDE) scenario. Our first goal was to extend the standard parametrisation within the ΛCDM cosmology of the growth rate f to include the dependence on the coupling between dark matter and dark energy ξ. Additionally, we aimed to place constraints on the phenomenological parameters of these alternative cosmological models by analyzing various cosmological datasets, in different combinations, to obtain a complementary analysis.

We derived a modified parametrisation for the growth rate f, which incorporates the coupling ξ. This extended parametrisation offers a more comprehensive description of structure formation within IDE cosmologies. Such a parametrisation depends on $\Omega_{\rm dm}$. Nevertheless, we proved that the error introduced due to this additional dependence does not significantly alter the cosmological analysis, introducing only a tiny difference with respect to the numerical results.

The cosmological analyses yield constraints consistent with a zero coupling scenario ($\xi \sim 0$), considering all the datasets taken into account in this work. These findings indicate that current cosmological observations do not yet provide significant evidence for non-gravitational interactions between dark matter and dark energy. As one would expect, Planck alone is not able to set very strong constraints on the coupling, as it is not sensible to the late time physics of the Universe and there is a strong degeneracy with the dark matter mass-energy density. When adding all the other datasets, the constraints become tighter. This is because Supernovae, BAO and RSD measurements are more sensitive to the time in which the coupling becomes important, with some of them being more sensitive than others, being RSD the one providing the tighter constraints.

The most peculiar results are obtained introducing the DESI DR1 measurements, which induce a modification of the best-fit values also in the ΛCDM scenario, then present for all combinations involving these data. Moreover, in considering the IDE scenario, we also obtain a non-zero best-fit value for the coupling, even if still consistent with a zero-value for ξ at 95% CL. In order to fully comprehend the meaning behind these results, we should wait for future releases from the DESI collaboration. Therefore, this is not yet a strong evidence for a possible non-zero coupling.

We find, as we would expect, that the largest degeneracy of the coupling ξ appears with the density parameter of cold dark matter, $\Omega_{\rm dm}h^2$. The degeneracy between these two parameters is strong when considering only CMB measurements. Nevertheless, when we introduce other measurements, which are more sensitive to late time physics (when ξ becomes more important), the degeneracy is reduced.

Our study placed particular emphasis on redshift space distortions (RSD) measurements, which have not been extensively highlighted in the recent literature. RSD data are crucial: indeed, we found that it is only when we add them that the constraints become much tighter, helping enormously in breaking the degeneracies.

Our findings have implications for the H_0 tension, which suggests discrepancies in the Hubble constant values derived from different observational methods. For the same reason above, while some measurements present a huge degeneracy between H_0 and ξ, alleviating the tension, when we include the RSD data the degeneracy almost disappears and the constraints point towards the Planck18 ΛCDM values.

Even though the cosmological analyses point towards the zero coupling scenario, indicating that the IDE could not be the final answer to the H_0 tension, for example, one must keep in mind that we only focused in this work on a particular case, among all the possible ones.

For this reason, as a future line of work, one could consider other models, which are closer to modified gravity models, to place constraints in light of recent redshift space distortion measurements.

In summary, while current observations favor a zero dark energy-dark matter coupling scenario, the methodologies and insights developed in this thesis lay the groundwork for future investigations into the dynamics of the Universe. Expanding the range of models and incorporating more comprehensive datasets will be essential in uncovering the true nature of dark energy, dark matter, and their potential interactions.

Appendix A

`CLASS` modifications

A.1 input.c

We set the default values for the new parameters: b, which discriminates between DEvel and DMvel models, and the coupling ξ. In addition, we force the dark energy to be described by a fluid.

```
pba->Omega0_lambda = 0.;
pba->Omega0_fld = 1. - pba->Omega0_k - Omega_tot;
class_read_double("coupling_xi", pba->coupling_xi);
class_read_double("b", pba->b);
```

⋮

```
/** 9) Dark energy contributions */
pba->Omega0_fld = 1.-pba->Omega0_k-pba->Omega0_g-pba->Omega0_ur
                    -pba->Omega0_b-pba->Omega0_cdm-pba->Omega0_ncdm_tot
                    -pba->Omega0_dcdmdr-pba->Omega0_idr-pba->Omega0_idm;
pba->xi = 0.;
pba->b = 1.;
//pba->Omega0_scf = 0.;
//pba->Omega0_lambda = 1.-pba->Omega0_k-pba->Omega0_g-pba->Omega0_ur
//                    -pba->Omega0_b-pba->Omega0_cdm-pba->Omega0_ncdm_tot
//                    -pba->Omega0_dcdmdr-pba->Omega0_idr-pba->Omega0_idm;
```

A.2 background.h

We add two new parameters: b, which discriminates between DEvel and DMvel models, and the coupling ξ.

```
double coupling_xi;
double b;
```

A.3 background.c

We modify the equations that describe the evolution of the background densities of dark matter and dark energy. Moreover, we modify the differential equation for the matter density perturbations and for the growth factor f.

```
/* cdm */
if (pba->has_cdm == _TRUE_) {
pvecback[pba->index_bg_rho_cdm] = pba->Omega0_cdm*pow(pba->H0,2)/
                                  pow(a,3)+(pba->Omega0_fld*
                                  pow(pba->H0,2)/pow(a,3))*
                                  (pba->coupling_xi/(3.*(pba->w0_fld+
                                  pba->coupling_xi/3.)))*(1.-pow(a,-3.*
                                  (pba->w0_fld+pba->coupling_xi/3.)));
rho_tot += pvecback[pba->index_bg_rho_cdm];
p_tot += 0.;
rho_m += pvecback[pba->index_bg_rho_cdm];
}
```

⋮

```
case CLP:
*w_fld = pba->w0_fld; //+ pba->wa_fld * (1. - a);
break;
```

⋮

```
case CLP:
*dw_over_da_fld = 0.;//- pba->wa_fld;
break;
```

⋮

```
case CLP:
*integral_fld = 3.*((1.+pba->w0_fld+pba->coupling_xi/3.)*log(1./a));
break;
```

⋮

```
if (pba->has_fld == _TRUE_) {
/* - Compute fld density \f $d\rho/dloga = -3(1+w_{fld}(a)) \rho\f$ */
dy[pba->index_bi_rho_fld] = -(3.+3.*pvecback[pba->index_bg_w_fld]+
                            pba->coupling_xi)*y[pba->index_bi_rho_fld];
}

⋮

/* - solve second order growth equation \f$ [D''(\tau)=-aHD'(\tau)+
3/2 a^2 \rho_M D(\tau) \f$ written as \f$ dD/dloga = D' / (aH) \f$
and \f$ dD'/dloga = -D' + (3/2) (a/H) \rho_M D \f$ */

rho_M = pvecback[pba->index_bg_rho_b];
if (pba->has_cdm == _TRUE_) {
    rho_M += pvecback[pba->index_bg_rho_cdm];
}
if (pba->has_idm == _TRUE_){
    rho_M += pvecback[pba->index_bg_rho_idm];
}

dy[pba->index_bi_D] = y[pba->index_bi_D_prime]/(a*H);
dy[pba->index_bi_D_prime] = -y[pba->index_bi_D_prime]+1.5*a*rho_M*
                            y[pba->index_bi_D]/H-pba->coupling_xi*
                            (y[pba->index_bi_rho_fld]/rho_M)*a*H*
                            (y[pba->index_bi_D]+((1.-pba->b)/(a*H))*
                            (y[pba->index_bi_D_prime]+
                            pba->coupling_xi*a*H*
                            (y[pba->index_bi_rho_fld]/rho_M))+
                            y[pba->index_bi_D_prime]/(a*H)-
                            0.5*y[pba->index_bi_D]*(1.+3.*
                            pvecback[pba->index_bg_w_fld]*
                            y[pba->index_bi_rho_fld]/(H*H))-
                            y[pba->index_bi_D]*(pba->coupling_xi+3.*
                            pvecback[pba->index_bg_w_fld]+
                            pba->coupling_xi*
                            (y[pba->index_bi_rho_fld]/rho_M)));
```

A.4 perturbations.c

We modify the differential equations that describe the evolution of the dark matter and dark energy density perturbations, respectively $\delta_{\rm dm}$ and $\delta_{\rm fld}$. We also modify the equations for θ_{dm} and θ_{fld}.

```
/* converting synchronous variables to newtonian ones */
if (ppt->gauge == newtonian) {

⋮

/* short-cut notations for the perturbations */
double delta_g=0.,theta_g=0.,shear_g=0.;
double delta_b,theta_b;
double theta_cdm=0.;

⋮

/** - ---> cdm */

if (pba->has_cdm == _TRUE_) {

  /** - ----> newtonian gauge: cdm density and velocity */

  if (ppt->gauge == newtonian) {
    dy[pv->index_pt_delta_cdm] = -(y[pv->index_pt_theta_cdm]+
                metric_continuity)+pba->coupling_xi*a_prime_over_a*
                (ppw->pvecback[pba->index_bg_rho_fld]/
                ppw->pvecback[pba->index_bg_rho_cdm])*
                (metric_euler/k2-y[pv->index_pt_delta_cdm]+
                y[pv->index_pt_delta_fld]);/* cdm density */

    dy[pv->index_pt_theta_cdm] = -a_prime_over_a*
                y[pv->index_pt_theta_cdm]+metric_euler+
                (1.-pba->b)*pba->coupling_xi*a_prime_over_a*
                (ppw->pvecback[pba->index_bg_rho_fld]/
                ppw->pvecback[pba->index_bg_rho_cdm])*
                (y[pv->index_pt_theta_fld]-y[pv->index_pt_theta_cdm]);
                /* cdm velocity */
  }

  /** - ----> synchronous gauge: cdm density only (velocity set to zero
  by definition of the gauge) */

  if (ppt->gauge == synchronous) {
```

```
    dy[pv->index_pt_delta_cdm] = -metric_continuity+a_prime_over_a*
                (ppw->pvecback[pba->index_bg_rho_fld]/
                ppw->pvecback[pba->index_bg_rho_cdm])*
                (y[pv->index_pt_delta_fld]-y[pv->index_pt_delta_cdm])*
                pba->coupling_xi; /* cdm density */

  }
}

⋮

/** - ---> fluid (fld) */

if (pba->has_fld == _TRUE_) {

  if (pba->use_ppf == _FALSE_){

    /* - ----> factors w, w_prime, adiabatic sound speed ca2 (all
    three background-related), plus actual sound speed in the
    fluid rest frame cs2 */

    class_call(background_w_fld(pba,a,&w_fld,&dw_over_da_fld,
    &integral_fld), pba->error_message, ppt->error_message);
    w_prime_fld = dw_over_da_fld * a_prime_over_a * a;

    ca2 = w_fld; //- w_prime_fld / 3. / (1.+w_fld) / a_prime_over_a;
    cs2 = pba->cs2_fld;

    /** - ----> fluid density */

    dy[pv->index_pt_delta_fld] =
      -(1+w_fld)*(y[pv->index_pt_theta_fld]+metric_continuity)
      -3.*(cs2-w_fld)*a_prime_over_a*y[pv->index_pt_delta_fld]
      -9.*(1+w_fld)*(cs2-w_fld)*a_prime_over_a*a_prime_over_a*
      y[pv->index_pt_theta_fld]*(1+pba->coupling_xi/(3.*(1+w_fld)))/k2;

    /** - ----> fluid velocity */

    if (ppt->gauge == synchronous) {
      theta_cdm = 0.;
```

```
    }
    else {
      theta_cdm = y[ppw->pv->index_pt_theta_cdm];
    }

    dy[pv->index_pt_theta_fld] = /* fluid velocity */
      -(1.-3.*cs2-pba->coupling_xi*(cs2+pba->b)/(1.+w_fld))*
      a_prime_over_a*y[pv->index_pt_theta_fld]+cs2*k2/(1.+w_fld)*
      y[pv->index_pt_delta_fld]+metric_euler-
      pba->b*pba->coupling_xi*a_prime_over_a*theta_cdm/(1.+w_fld);
  }
  else {  /* Gamma variable of PPF formalism */
    dy[pv->index_pt_Gamma_fld] = ppw->Gamma_prime_fld;
  }
}
```

Appendix B

Priors used in the MCMC analysis

In this appendix we present a table with the parameters we sampled in the MCMC analyses (using `Cobaya` [33, 34]) together with the ranges in which we allow these parameters to change. All of the priors are flat in the ranges given.

Parameter	Priors
$\boldsymbol{\log(10^{10} A_\mathrm{s})}$	$\mathcal{U}[1.61, 3.91]$
$\boldsymbol{n_\mathrm{s}}$	$\mathcal{U}[0.8, 1.2]$
$\boldsymbol{100\theta_\mathrm{s}}$	$\mathcal{U}[0.5, 10]$
$\boldsymbol{\Omega_\mathrm{b} h^2}$	$\mathcal{U}[0.005, 0.1]$
$\boldsymbol{\Omega_\mathrm{dm} h^2}$	$\mathcal{U}[0.001, 0.99]$
$\boldsymbol{\tau_\mathrm{reio}}$	$\mathcal{U}[0.01, 0.8]$
$\boldsymbol{\xi}$	$\mathcal{U}[-1.0, 0.0]$

Table B.1: Table summarising the cosmological parameters that are sampled over in different runs and the priors that are placed on them.

Bibliography

[1] N. Aghanim et al. “Planck2018 results: VI. Cosmological parameters”. In: *Astronomy & Astrophysics* 641 (2020).

[2] Adam G. Riess et al. “A Comprehensive Measurement of the Local Value of the Hubble Constant with 1 km s^{-1} Mpc^{-1}. Uncertainty from the Hubble Space Telescope and the SH0ES Team”. In: *The Astrophysical Journal Letters* 934.1 (2022).

[3] Licia Verde, Tommaso Treu, and Adam G. Riess. “Tensions between the early and late Universe”. In: *Nature Astronomy* 3.10 (2019).

[4] Eleonora Di Valentino et al. “Snowmass2021 - Letter of interest cosmology intertwined II: The hubble constant tension”. In: *Astropart. Phys.* 131 (2021). arXiv: `2008.11284 [astro-ph.CO]`.

[5] Adam G. Riess et al. “Cluster Cepheids with High Precision Gaia Parallaxes, Low Zeropoint Uncertainties, and Hubble Space Telescope Photometry”. In: (2022). arXiv: `2208.01045 [astro-ph.CO]`.

[6] Eleonora Di Valentino et al. “In the realm of the Hubble tension—a review of solutions”. In: *Class. Quant. Grav.* 38.15 (2021). arXiv: `2103.01183 [astro-ph.CO]`.

[7] Nils Schöneberg et al. “The H0 Olympics: A fair ranking of proposed models”. In: *Phys. Rept.* 984 (2022), pp. 1–55. DOI: `10.1016/j.physrep.2022.07.001`. arXiv: `2107.10291 [astro-ph.CO]`.

[8] Marika Asgari et al. “KiDS-1000 cosmology: Cosmic shear constraints and comparison between two point statistics”. In: *Astronomy & Astrophysics* 645 (2021).

[9] Laura Lopez Honorez et al. “Coupled dark matter-dark energy in light of near universe observations”. In: *Journal of Cosmology and Astroparticle Physics* 2010.09 (2010).

[10] M.B. Gavela et al. “Dark coupling”. In: *Journal of Cosmology and Astroparticle Physics* 2009.07 (2009).

[11] Glennys R. Farrar and P. J. E. Peebles. “Interacting Dark Matter and Dark Energy”. In: *The Astrophysical Journal* 604.1 (2004).

[12] John D. Barrow and T. Clifton. "Cosmologies with energy exchange". In: *Physical Review D* 73.10 (2006).

[13] Luca Amendola, Gabriela Camargo Campos, and Rogerio Rosenfeld. "Consequences of dark matter-dark energy interaction on cosmological parameters derived from type Ia supernova data". In: *Physical Review D* 75.8 (2007).

[14] Jian-Hua He and Bin Wang. "Effects of the interaction between dark energy and dark matter on cosmological parameters". In: *Journal of Cosmology and Astroparticle Physics* 2008.06 (2008).

[15] Jussi Väliviita, Elisabetta Majerotto, and Roy Maartens. "Large-scale instability in interacting dark energy and dark matter fluids". In: *Journal of Cosmology and Astroparticle Physics* 2008.07 (2008).

[16] Gabriela Caldera-Cabral, Roy Maartens, and Bjoern Malte Schaefer. "The growth of structure in interacting dark energy models". In: *Journal of Cosmology and Astroparticle Physics* 2009.07 (2009).

[17] Elisabetta Majerotto, Jussi Väliviita, and Roy Maartens. "Adiabatic initial conditions for perturbations in interacting dark energy models". In: *Monthly Notices of the Royal Astronomical Society* 402.4 (2010).

[18] Elcio Abdalla, L. Raul Abramo, and José C. C. de Souza. "Signature of the interaction between dark energy and dark matter in observations". In: *Physical Review D* 82.2 (2010).

[19] Timothy Clemson et al. "Interacting dark energy: Constraints and degeneracies". In: *Physical Review D* 85.4 (2012).

[20] Supriya Pan, Subhra Bhattacharya, and Subenoy Chakraborty. "An analytic model for interacting dark energy and its observational constraints". In: *Monthly Notices of the Royal Astronomical Society* 452.3 (2015).

[21] Valentina Salvatelli et al. "New constraints on coupled dark energy from the Planck satellite experiment". In: *Physical Review D* 88.2 (2013).

[22] Rafael C. Nunes and Edésio M. Barboza. "Dark matter–dark energy interaction for a time-dependent EoS parameter". In: *General Relativity and Gravitation* 46.11 (2014).

[23] Valerio Faraoni, James B. Dent, and Emmanuel N. Saridakis. "Covariantizing the interaction between dark energy and dark matter". In: *Physical Review D* 90.6 (2014).

[24] Elisa G. M. Ferreira et al. "Evidence for interacting dark energy from BOSS". In: *Physical Review D* 95.4 (2017).

[25] R. Murgia, S. Gariazzo, and N. Fornengo. "Constraints on the coupling between dark energy and dark matter from CMB data". In: *Journal of Cosmology and Astroparticle Physics* 2016.04 (2016).

[26] Rafael C. Nunes, Supriya Pan, and Emmanuel N. Saridakis. "New constraints on interacting dark energy from cosmic chronometers". In: *Physical Review D* 94.2 (2016).

[27] Weiqiang Yang et al. "Cosmological constraints on coupled dark energy". In: *Journal of Cosmology and Astroparticle Physics* 2016.10 (2016).

[28] R. von Marttens et al. "Cosmological constraints on parametrized interacting dark energy". In: *Physics of the Dark Universe* 23 (2019).

[29] Eric V. Linder. "Cosmic growth history and expansion history". In: *Physical Review D* 72.4 (2005).

[30] Eric V. Linder and Robert N. Cahn. "Parameterized beyond-Einstein growth". In: *Astroparticle Physics* 28.4–5 (2007).

[31] Julien Lesgourgues. *The Cosmic Linear Anisotropy Solving System (CLASS) I: Overview.* 2011. arXiv: `1104.2932 [astro-ph.IM]`.

[32] Diego Blas, Julien Lesgourgues, and Thomas Tram. "The Cosmic Linear Anisotropy Solving System (CLASS). Part II: Approximation schemes". In: *Journal of Cosmology and Astroparticle Physics* 2011.07 (2011).

[33] Jesús Torrado and Antony Lewis. *Cobaya: Bayesian analysis in cosmology.* Astrophysics Source Code Library, record ascl:1910.019. 2019.

[34] Jesús Torrado and Antony Lewis. "Cobaya: code for Bayesian analysis of hierarchical physical models". In: *Journal of Cosmology and Astroparticle Physics* 2021.05 (2021).

[35] Scott Dodelson. *Modern Cosmology.* Academic Press, 2003.

[36] Edwin Hubble. "A Relation between Distance and Radial Velocity among Extra-Galactic Nebulae". In: *Proceedings of the National Academy of Science* 15.3 (1929).

[37] H. P. Robertson. *Kinematics and World-Structure.* 1935.

[38] V. C. Rubin, Jr. Ford W. K., and N. Thonnard. *Rotational properties of 21 SC galaxies with a large range of luminosities and radii, from NGC 4605 (R=4kpc) to UGC 2885 (R=122kpc).* 1980.

[39] Douglas Clowe et al. "A Direct Empirical Proof of the Existence of Dark Matter". In: *The Astrophysical Journal* 648.2 (2006).

[40] S. Chandrasekhar. *The Maximum Mass of Ideal White Dwarfs.* 1931.

[41] The Dark Energy Survey Collaboration. *The Dark Energy Survey.* 2005. arXiv: `astro-ph/0510346 [astro-ph]`.

[42] T. M. C. Abbott et al. "First Cosmology Results using Type Ia Supernovae from the Dark Energy Survey: Constraints on Cosmological Parameters". In: *The Astrophysical Journal Letters* 872.2 (2019).

[43] DES Collaboration et al. *The Dark Energy Survey: Cosmology Results With ∼1500 New High-redshift Type Ia Supernovae Using The Full 5-year Dataset.* 2024. arXiv: `2401.02929 [astro-ph.CO]`.

[44] D. M. Scolnic et al. "The Complete Light-curve Sample of Spectroscopically Confirmed SNe Ia from Pan-STARRS1 and Cosmological Constraints from the Combined Pantheon Sample". In: *The Astrophysical Journal* 859.2 (2018).

[45] A. A. Penzias and R. W. Wilson. *A Measurement of Excess Antenna Temperature at 4080 Mc/s.* 1965.

[46] D. Fixsen and John Mather. *The Spectral Results of the FIRAS Instrument on COBE.* 2002.

[47] Julien Lesgourgues et al. *Neutrino Cosmology.* Cambridge University Press, 2013.

[48] Daniel J. Eisenstein et al. "Detection of the Baryon Acoustic Peak in the Large-Scale Correlation Function of SDSS Luminous Red Galaxies". In: *The Astrophysical Journal* 633.2 (2005).

[49] Jiamin Hou et al. "The completed SDSS-IV extended Baryon Oscillation Spectroscopic Survey: BAO and RSD measurements from anisotropic clustering analysis of the quasar sample in configuration space between redshift 0.8 and 2.2". In: *Monthly Notices of the Royal Astronomical Society* 500.1 (2020).

[50] Shadab Alam et al. "Completed SDSS-IV extended Baryon Oscillation Spectroscopic Survey: Cosmological implications from two decades of spectroscopic surveys at the Apache Point Observatory". In: *Physical Review D* 103.8 (2021).

[51] BOSS collaboration. `https://www.sdss3.org/surveys/boss.php`. 2009.

[52] A. J. S. Hamilton. *Linear Redshift Distortions: A Review.* 1998.

[53] Felipe Avila et al. "Inferring $S_8(z)$ and $\gamma(z)$ with cosmic growth rate measurements using machine learning". In: *The European Physical Journal C* 82.7 (2022).

[54] F Avila et al. "The growth rate of cosmic structures in the local Universe with the ALFALFA survey". In: *Monthly Notices of the Royal Astronomical Society* 505.3 (2021).

[55] E. Hawkins et al. "The 2dF Galaxy Redshift Survey: correlation functions, peculiar velocities and the matter density of the Universe". In: *Monthly Notices of the Royal Astronomical Society* 346.1 (2003).

[56] L. Guzzo et al. "A test of the nature of cosmic acceleration using galaxy redshift distortions". In: *Nature* 451.7178 (2008).

[57] Chris Blake et al. “Galaxy And Mass Assembly (GAMA): improved cosmic growth measurements using multiple tracers of large-scale structure”. In: *Mon. Not. Roy. Astron. Soc.* 436 (2013). arXiv: `1309.5556 [astro-ph.CO]`.

[58] Chris Blake et al. “The WiggleZ Dark Energy Survey: the growth rate of cosmic structure since redshift z=0.9”. In: 415.3 (2011). arXiv: `1104.2948 [astro-ph.CO]`.

[59] Max Tegmark et al. “Cosmological constraints from the SDSS luminous red galaxies”. In: *Physical Review D* 74.12 (2006).

[60] Nicholas P. Ross et al. “The 2dF-SDSS LRG and QSO Survey: the LRG 2-point correlation function and redshift-space distortions”. In: *Monthly Notices of the Royal Astronomical Society* 381.2 (2007).

[61] J. DaÂngela et al. “The 2dF-SDSS LRG and QSO survey: QSO clustering and the L-z degeneracy”. In: *Monthly Notices of the Royal Astronomical Society* 383.2 (2007).

[62] Stephen J. Turnbull et al. “Cosmic flows in the nearby universe from Type Ia supernovae”. In: *Monthly Notices of the Royal Astronomical Society* 420.1 (2011).

[63] I. Achitouv et al. “Consistency of the growth rate in different environments with the 6-degree Field Galaxy Survey: Measurement of the void-galaxy and galaxy-galaxy correlation functions”. In: *Physical Review D* 95.8 (2017).

[64] Florian Beutler et al. “The 6dF Galaxy Survey: z≈0 measurements of the growth rate and σ_8”. In: *Monthly Notices of the Royal Astronomical Society* 423.4 (2012).

[65] Martin Feix, Adi Nusser, and Enzo Branchini. “Growth Rate of Cosmological Perturbations at $z \sim 0.1$ from a New Observational Test”. In: *Physical Review Letters* 115.1 (2015).

[66] Shadab Alam et al. “The clustering of galaxies in the completed SDSS-III Baryon Oscillation Spectroscopic Survey: cosmological analysis of the DR12 galaxy sample”. In: *Monthly Notices of the Royal Astronomical Society* 470.3 (2017).

[67] Ariel G. Sánchez et al. “The clustering of galaxies in the SDSS-III Baryon Oscillation Spectroscopic Survey: cosmological implications of the full shape of the clustering wedges in the data release 10 and 11 galaxy samples”. In: *Monthly Notices of the Royal Astronomical Society* 440.3 (2014).

[68] Chris Blake et al. “The WiggleZ Dark Energy Survey: joint measurements of the expansion and growth history at z¡1”. In: *Monthly Notices of the Royal Astronomical Society* 425.1 (2012).

[69] Seshadri Nadathur et al. “Beyond BAO: Improving cosmological constraints from BOSS data with measurement of the void-galaxy cross-correlation”. In: *Physical Review D* 100.2 (2019).

[70] Chia-Hsun Chuang et al. "The clustering of galaxies in the SDSS-III Baryon Oscillation Spectroscopic Survey: single-probe measurements from CMASS anisotropic galaxy clustering". In: *Monthly Notices of the Royal Astronomical Society* 461.4 (2016).

[71] Marie Aubert et al. "The completed SDSS-IV extended Baryon Oscillation Spectroscopic Survey: growth rate of structure measurement from cosmic voids". In: *Monthly Notices of the Royal Astronomical Society* 513.1 (2022).

[72] Michael J. Wilson. *Geometric and growth rate tests of General Relativity with recovered linear cosmological perturbations.* 2016. arXiv: `1610.08362 [astro-ph.CO]`.

[73] Gong-Bo Zhao et al. "The clustering of the SDSS-IV extended Baryon Oscillation Spectroscopic Survey DR14 quasar sample: a tomographic measurement of cosmic structure growth and expansion rate based on optimal redshift weights". In: *Monthly Notices of the Royal Astronomical Society* 482.3 (2018).

[74] Teppei Okumura et al. "The Subaru FMOS galaxy redshift survey (FastSound). IV. New constraint on gravity theory from redshift space distortions at z$\sim$1.4". In: *Publications of the Astronomical Society of Japan* 68.3 (2016).

[75] Chung-Pei Ma and Edmund Bertschinger. "Cosmological Perturbation Theory in the Synchronous and Conformal Newtonian Gauges". In: *The Astrophysical Journal* 455 (1995).

[76] Sean M. Carroll. "Quintessence and the Rest of the World: Suppressing Long-Range Interactions". In: *Physical Review Letters* 81.15 (1998).

[77] Christof Wetterich. "The Cosmon model for an asymptotically vanishing time dependent cosmological 'constant'". In: *Astron. Astrophys.* 301 (1995). arXiv: `hep-th/9408025`.

[78] Luca Amendola. "Perturbations in a coupled scalar field cosmology". In: *Mon. Not. Roy. Astron. Soc.* 312 (2000). arXiv: `astro-ph/9906073`.

[79] Luca Amendola. "Coupled quintessence". In: *Phys. Rev. D* 62 (2000). arXiv: `astro-ph/9908023`.

[80] G. Mangano, Gennaro Miele, and V. Pettorino. "Coupled quintessence and the coincidence problem". In: *Mod. Phys. Lett. A* 18 (2003). arXiv: `astro-ph/0212518`.

[81] Thomas Bayes Rev. "An essay toward solving a problem in the doctrine of chances". In: *Phil. Trans. Roy. Soc. Lond.* 53 (1764).

[82] Roberto Trotta. *Bayesian Methods in Cosmology.* 2017. arXiv: `1701.01467 [astro-ph.CO]`.

[83] Steve Brooks et al. *Handbook of Markov Chain Monte Carlo.* 2011.

[84] Nicholas Metropolis et al. “Equation of State Calculations by Fast Computing Machines”. In: *The Journal of Chemical Physics* 21.6 (1953).

[85] W. K. Hastings. “Monte Carlo Sampling Methods Using Markov Chains and Their Applications”. In: *Biometrika* 57.1 (1970).

[86] Andrew Gelman and Donald B. Rubin. “Inference from Iterative Simulation Using Multiple Sequences”. In: *Statistical Science* 7.4 (1992).

[87] N. Aghanim et al. “Planck2018 results: I. Overview and the cosmological legacy ofPlanck”. In: *Astronomy & Astrophysics* 641 (2020).

[88] N. Aghanim et al. “Planck 2018 results: V. CMB power spectra and likelihoods”. In: *Astronomy & Astrophysics* 641 (2020).

[89] N. Aghanim et al. “Planck 2018 results. VIII. Gravitational lensing”. In: *Astron. Astrophys.* 641 (2020). arXiv: `1807.06210 [astro-ph.CO]`.

[90] Adam G. Riess et al. “Observational Evidence from Supernovae for an Accelerating Universe and a Cosmological Constant”. In: *The Astronomical Journal* 116.3 (1998).

[91] S. Perlmutter et al. “Measurements of Ω and Λ from 42 High-Redshift Supernovae”. In: *The Astrophysical Journal* 517.2 (1999).

[92] Dan Scolnic et al. “The Pantheon+ Analysis: The Full Data Set and Light-curve Release”. In: *The Astrophysical Journal* 938.2 (2022).

[93] Dillon Brout et al. “The Pantheon+ Analysis: Cosmological Constraints”. In: *The Astrophysical Journal* 938.2 (2022).

[94] DESI Collaboration et al. *DESI 2024 VI: Cosmological Constraints from the Measurements of Baryon Acoustic Oscillations.* 2024. arXiv: `2404.03002 [astro-ph.CO]`.

[95] ChangHoon Hahn et al. “The DESI Bright Galaxy Survey: Final Target Selection, Design, and Validation”. In: *The Astronomical Journal* 165.6 (2023).

[96] Rongpu Zhou et al. “Target Selection and Validation of DESI Luminous Red Galaxies”. In: *The Astronomical Journal* 165.2 (2023).

[97] A. Raichoor et al. “Target Selection and Validation of DESI Emission Line Galaxies”. In: *The Astronomical Journal* 165.3 (2023).

[98] DESI Collaboration et al. *DESI 2024 III: Baryon Acoustic Oscillations from Galaxies and Quasars.* 2024. arXiv: `2404.03000 [astro-ph.CO]`.

[99] Edmond Chaussidon et al. “Target Selection and Validation of DESI Quasars”. In: *The Astrophysical Journal* 944.1 (2023).

[100] DESI Collaboration et al. *DESI 2024 IV: Baryon Acoustic Oscillations from the Lyman Alpha Forest.* 2024. arXiv: `2404.03001 [astro-ph.CO]`.

[101] Antony Lewis and Sarah Bridle. “Cosmological parameters from CMB and other data: A Monte Carlo approach”. In: *Physical Review D* 66.10 (2002).

[102] Antony Lewis. “Efficient sampling of fast and slow cosmological parameters”. In: *Physical Review D* 87.10 (2013).

[103] Antony Lewis. *GetDist: a Python package for analysing Monte Carlo samples.* 2019. arXiv: `1910.13970 [astro-ph.IM]`.

[104] Eleonora Di Valentino, Alessandro Melchiorri, and Olga Mena. “Can interacting dark energy solve the H_0 tension?” In: *Phys. Rev. D* 96.4 (2017), p. 043503. DOI: `10.1103/PhysRevD.96.043503`. arXiv: `1704.08342 [astro-ph.CO]`.

[105] Eleonora Di Valentino et al. “Interacting dark energy in the early 2020s: A promising solution to the H_0 and cosmic shear tensions”. In: *Phys. Dark Univ.* 30 (2020), p. 100666. DOI: `10.1016/j.dark.2020.100666`. arXiv: `1908.04281 [astro-ph.CO]`.

[106] Eleonora Di Valentino et al. “Nonminimal dark sector physics and cosmological tensions”. In: *Phys. Rev. D* 101.6 (2020), p. 063502. DOI: `10.1103/PhysRevD.101.063502`. arXiv: `1910.09853 [astro-ph.CO]`.

[107] Weiqiang Yang et al. “2021-H0 odyssey: closed, phantom and interacting dark energy cosmologies”. In: *JCAP* 10 (2021), p. 008. DOI: `10.1088/1475-7516/2021/10/008`. arXiv: `2101.03129 [astro-ph.CO]`.

[108] Weiqiang Yang et al. “Dynamical dark energy after Planck CMB final release and H_0 tension”. In: *Mon. Not. Roy. Astron. Soc.* 501.4 (2021), pp. 5845–5858. DOI: `10.1093/mnras/staa3914`. arXiv: `2101.02168 [astro-ph.CO]`.

[109] Supriya Pan et al. “Interacting scenarios with dynamical dark energy: Observational constraints and alleviation of the H_0 tension”. In: *Phys. Rev. D* 100.10 (2019), p. 103520. DOI: `10.1103/PhysRevD.100.103520`. arXiv: `1907.07540 [astro-ph.CO]`.

[110] Weiqiang Yang et al. “Observational constraints on one-parameter dynamical dark-energy parametrizations and the H_0 tension”. In: *Phys. Rev. D* 99.4 (2019), p. 043543. DOI: `10.1103/PhysRevD.99.043543`. arXiv: `1810.05141 [astro-ph.CO]`.

[111] Weiqiang Yang et al. “Interacting dark energy with time varying equation of state and the H_0 tension”. In: *Phys. Rev. D* 98.12 (2018), p. 123527. DOI: `10.1103/PhysRevD.98.123527`. arXiv: `1809.06883 [astro-ph.CO]`.

[112] Weiqiang Yang et al. “Tale of stable interacting dark energy, observational signatures, and the H_0 tension”. In: *JCAP* 09 (2018), p. 019. DOI: `10.1088/1475-7516/2018/09/019`. arXiv: `1805.08252 [astro-ph.CO]`.